UNIVERSITY OF CALIFORNIA

Santa Barbara

Exploration of transient landscapes within the Western Transverse Range, CA

A dissertation submitted in partial satisfaction of the

requirements for the degree Doctor of Philosophy

in Geography

by

Nina L. Bingham

Committee in charge:

Professor Oliver Chadwick, Chair

Professor Bodo Bookhagen

Professor Tom Dunne

June 2019

The dissertation of Nina L. Bingham is approved.

_____

Tom Dunne

_____

Bodo Bookhagen

_____

Oliver Chadwick, Committee Chair

June 2019

ACKNOWLEDGEMENTS

I am very thankful to my committee for providing me endless support throughout the dissertation. I am very appreciative of Tom's participation in the finalizing and polishing process. I am also very thankful for Bodo's enthusiasm in collaborating with me and his willingness to host me in Berlin. Lastly, I am eternally grateful to Oliver for always being there for me and encouraging my soil explorations.

I would like to thank Adam Davis for his advice in spatial data processing specifically for Chapter 4 and his R advice for the entire dissertation. More importantly, Adam has been an unending source of love, support, walks, and productive conversations during the entire dissertation and for this I am entirely grateful.

I owe a lot of my success to my co-authors (and also friends) Eric Slessarev, Kerri Johnson, and Pete Homyak for their enthusiasm for my science and patience with my writing.

I have been fortunate to find myself with a set of loving and empowering friends who have made the last 6 years truly enjoyable. Thank you Kate Voss, Kelsey Bisson, Sasha Kramer, and Steph Moore.

None of my work would be possible without the guidance from the reserve managers at Sedgwick Reserve and Santa Cruz Island. I would also like to thank the UC Reserve system and the Nature Conservancy for permitting the excavation of many soil pits on their property.

A whole army of people have come to my aid over the years – helping me dig holes, grind samples, label bags, and keep me company. They understood the work was dirty but dedicated their time anyways and for this I am very thankful. This includes, Claire Kouba, Gad Girling, Andrea Whyte, Andrew Saunders, Denise Villanueva, Chuck Sweeney, Tess Irving-Ruffing, Lauren Illes, and Vivi Von Welczeck and many more.

Lastly, I would like to thank several sets of parents who have been there for me when I needed a family. This includes some West Coast families, Nancy & Jerry and Matt & Paula, who have adopted me for many holidays. Finally, thank you to my family, who have always encouraged me to pursue my curiosity for science.

VITA OF NINA L. BINGHAM
May 2019

PhD Candidate, ABD
Department of Geography
University of California Santa Barbara
Santa Barbara, California 93106-4060
nbingham@ucsb.edu

EDUCATION

Ph.D. in Geography, University of California Santa Barbara
Dissertation: *Exploration of transient landscapes within the Western Transverse Range, CA*
Advisors: Oliver Chadwick & Bodo Bookhagen
Expected Completion: May, 2019

M.A. in Geography, University of California Santa Barbara
Thesis: *Strontium isotopes provide clues for base cation sources in young Kona soils*
Advisor: Oliver Chadwick
December, 2015

B.S. in Geosciences (Honors), The Pennsylvania State University
Thesis: *Carbon, nitrogen, and manganese in shale soil profiles along a climate gradient*
Advisor: Susan Brantley
May, 2013

RESEARCH EXPERIENCE

Research Assistant for the Chadwick and Bookhagen Research Groups | Sept. 2013 - current
Dept. of Geography, University of California Santa Barbara

Clean lab chemistry including: soil, rock dissolutions and strontium (Sr) separation by column chemistry for $^{87}Sr/^{86}Sr$ analyses, and channel sand leaching and beryllium (Be) isolation via column chemistry for cosmogenic radionuclide target preparation. Instrument use including: MC-ICP-MS, ICP-MS and ICP-OES operation. *Computational work including*: topographic analysis of landscapes using digital elevation models in R, Matlab, Python, and ArcGIS.

Undergraduate Lab Technician for the Brantley Research Group | May 2011 - Sept. 2013
Dept. of Geosciences, The Pennsylvania State University

Field work in environmental geochemistry, including: soil pit digging/augering, lysimeter water collection and sample prep, tree coring and gas/water well monitoring. Rock, soil and water sample preparation, including: rock and soil crushing/sieving, dilutions, and extractions for analysis by CHNS analyzer, ion chromatography, ICP-AES, XRD, and loss on ignition.

PUBLICATIONS

N.L. Bingham, B. Bookhagen, K. Johnson, and O.A. Chadwick (in review – JGR: Earth Surface) *Use of lidar point-cloud data to assess human-induced erosion and loss of vegetation cover on contrasting lithologies.*

N.L. Bingham and O.A. Chadwick (in prep) *Strontium isotopes provide clues for hydrologic influence on chemical weathering in young volcanic soils.*

Y. Lin, S.E. Prentice III, T. Tran, **N.L. Bingham**, J.Y. King, O.A. Chadwick (2016) *Topographically determined patterns of soil carbon and nitrogen in Southern California grasslands.* Geoderma Regional: 7, 67-75. doi:10.1016/j.geodrs.2016.01.005

E.W. Slessarev, Y. Lin, **N.L. Bingham**, J.E. Johnson, Y. Dai, J.P. Schimel, O.A. Chadwick (2016) *Water Balance Defines a Threshold in Soil pH at the Global Scale.* Nature. doi:10.1038/nature20139

CONFERENCE PRESENTATIONS

N.L. Bingham, E. Slessarev, P. Homyak, M. Zhu, O. A. Chadwick (2019) *Evidence for rock-derived nitrogen contributions at the pedon-scale in a Mediterranean grassland*, International Soils Meeting: Soils Across Latitudes, San Diego, CA. (invited talk)

N.L. Bingham, B. Bookhagen, O.A Chadwick (2017) *Spatial and temporal patterns of anthropogenic-driven erosion controlled by rock type*, Geological Society of America Annual Meeting, Seattle, WA (talk)

N.L. Bingham, B. Bookhagen, O.A Chadwick (2017) *Rock-Derived N Influx and Distribution on Mediterranean Climate Hillslopes*, 2017 Goldschmidt, Paris, France. (talk)

N.L. Bingham, K. Johnson, B. Bookhagen, O.A Chadwick (2016) *Propagation of varied timescale perturbations in landscapes*, 2016 American Geophysical Union Annual Meeting, San Francisco, CA. (poster)

N.L. Bingham, B. Bookhagen, O.A Chadwick (2016) *Stable vs. Evolving hillslopes: Setting the geomorphic stage for interpreting soils*, Geological Society of America Annual Meeting, Denver, CO (talk)

N.L. Bingham, M.G. Jackson, B. Bookhagen, K. Maher, O.A Chadwick (2015) *Strontium isotopes provide clues for a process shift in base cation dynamics in young volcanic soils*, 2015 American Geophysical Union Annual Meeting, San Francisco, CA. (poster)

N.L. Bingham and O.A. Chadwick (2015) *Strontium isotopes provide clues for base cation sources in young Kona soils*, Hawaii Ecosystems Project Annual Meeting, Hilo, HI. (talk)

N.L. Bingham, A. Dere, S.L. Brantley (2012) *Modeling Soil Addition Profiles of Carbon, Nitrogen, Lead and Manganese Across a Climate Gradient*, Soil Science Society of America Annual Meeting, Cincinnati, OH (poster)

TEACHING EXPERIENCE

Course Instructor, Soil Genesis and Classification | Spring 2017
Dept. of Geography, University of California Santa Barbara

Teaching Assistant, Quantitative Geomorphology | Spring 2019
Dept. of Geography, University of California Santa Barbara

Teaching Assistant, Soil Genesis and Classification | Winter 2019
Dept. of Geography, University of California Santa Barbara

Teaching Assistant, Soil Science | Fall 2013-2018
Dept. of Geography, University of California Santa Barbara

Teaching Assistant, Groundwater Hydrology | Winter 2014
Dept. of Geography, University of California Santa Barbara

Teaching Assistant, Environmental Water Quality | Spring 2014
Dept. of Geography, University of California Santa Barbara

Teaching Assistant, Calculus with Earth and Mineral Sciences Applications II | Spring 2013
College of Earth and Mineral Sciences, The Pennsylvania State University

Teaching Assistant, Calculus with Earth and Mineral Sciences Applications I | Fall 2012
College of Earth and Mineral Sciences, The Pennsylvania State University

AWARDS AND HONORS

GSA Graduate Student Research Grant | 2016
Geological Society of America

Jack and Laura Dangermond Travel Award | 2015, 2016, 2017, 2019
Dept. of Geography, University of California Santa Barbara

Leal Anne Kerry Mertes Scholarship | 2014
Dept. of Geography, University of California Santa Barbara

Marathon Oil Scholarship | 2009 – 2013
College of Earth and Mineral Sciences, The Pennsylvania State University

James and Nancy Hedberg Scholarship in Geosciences | 2011
Dept. of Geosciences, The Pennsylvania State University

Teas Scholarship for Excellence | 2010
College of Earth and Mineral Sciences, The Pennsylvania State University

WISER Undergraduate Research Award | 2009
NASA Pennsylvania Space Grant Consortium, The Pennsylvania State University

ABSTRACT

Exploration of transient landscapes within the Western Transverse Range, CA

by

Nina L. Bingham

Determining where sediment goes and why is a problem that defines the field of geomorphology and has direct implications on the fields of soil science and ecology. The morphology of landscapes changes when they are perturbed from a balance between uplift and erosion – this leads to a state of transience where soil and sediment is shed or accumulated in order to reestablish steady-state. This dissertation looks at what happens to the landscape when the balance between uplift and erosion is upset by different timescales of perturbations: 1) tectonic uplift and sea-level rise induced base level change over tens of thousands of years and 2) human land-use induced decreases in soil cohesion over the last 200 years. I use the westernmost portion of the Transverse Range, CA for this research. Active tectonics and a spatial variation in lithology within a similar climate makes this region a natural laboratory for this work. This dissertation encompasses three, individual studies which contribute towards understanding landscape change over different timescales in the Western Transverse Range, CA. Collectively, these studies show that the interplay between climate and lithology influences the way this landscapes adjust to both long- and short-timescale perturbations to the balance between uplift and erosion. Specifically, the current semi-arid climate limits how soil is produced and where it can go in a landscape, and the erodibility of the underlying lithology sets how much soil can be produced and how erosion can be translated across catchments.

TABLE OF CONTENTS

Chapter 1. Introduction

Soil is the life sustaining membrane of Earth, providing substrate for shelter and sustenance for terrestrial organisms. Ultimately, the presence of soil on a landscape and its nutrient status is set by the rates and relative balance of uplift and erosion. If these rates are unequal, the landscape is in a state of transience, accumulating or eroding soil until a steady-state is achieved (Montgomery, 2001). Landscape response to transience is often not spatially uniform; internal and external factors such as underlying lithology, vegetation, climate, and human activity can all effect where and how much soil is removed or accumulated (Jenny, 1941). Measuring the heterogeneity in landscape response and assessing the factors which drive these differences is imperative for understanding the controls on chemical and physical properties of soil and consequently ecosystem health. The necessity of soil for life makes this an ongoing pursuit of many fields researching Earth surface processes.

The westernmost portion of the Transverse Range can be utilized as a natural laboratory to study the factors controlling landscape adjustment; the region has well constrained uplift rates (c.f. Rockwell et al., 1992; Metcalf, 1994; Gurrola et al., 2014; Farris 2017; Morel and Keller, 2017), spatially uniform but temporally varied climate (Kennet and Ingram, 1995), and heterogeneous lithologic assemblage (Jennings et al., 2010). Furthermore, the region is subject to multiple timescales of perturbation to the balance between uplift and erosion. Tectonic uplift, and glacial-cycle related climate and sea-level fluctuations change the balance between uplift and erosion by adjusting the base level and stream power for the region over timescales of $10^{4\text{-}6}$ years (Metcalf, 1994; DeVecchio et al., 2012; Reynolds and Simms, 2015). Additionally, the region has undergone widespread population growth and land use change over the last 200 years. This anthropogenic influence entails vegetation

change and removal, and soil disturbance which decreases the cohesiveness of the soil and effectively increases the erosivity of the system (Perroy et al., 2012; Gabet and Dunne, 2003). These natural and anthropogenic perturbations produce a timescale gradient in landscape response over which to examine what and how different factors influence the adjustment of a landscape and soil.

This dissertation seeks to understand how and why landscapes within the Western Transverse Range respond to disturbances over multiple timescales. I first provide a brief background (Chapter 2) of climate, tectonics, geology, and human land use in the region for context. I then describe three stand-alone studies which provide 1) an assessment of possible controls on long-term transience across the whole westernmost Transverse Range, 2) the factors controlling the landscape response to recent, and rapid anthropogenic-driven erosion, and 3) a deep dive into the factors controlling chemical weathering and rock-derived nutrient fluxes from a lower anthropogenically disturbed soil. Together these chapters elucidate how different factors interact over multiple timescales of perturbation to influence the landscape and soils of the western Transverse Range. I summarize the three studies below.

In Chapter 3, I produce the first set of long-term erosion rates for the Western Transverse Range and look for controls on these erosion rates and the resulting landscape morphology. There is a dearth of long-term erosion rate data for the region and understanding average rates for sediment movement across the landscape is necessary for assessing geologic hazards. I compare erosion rates with known uplift rates for the last 100 kyr and explain discrepancies using both a catchment average and spatially explicit topographic metric, the normalized stream steepness index. This work shows that much of the westernmost Transverse Range is out of steady-state during the Holocene, with uplift rates an order of

magnitude faster than erosion rates. Sampling location, paleoclimate fluctuations, and variation in the erodibility of bedrock help explain the low erosion rates for some of the catchments. Holocene-age climate drying has decreased stream power and increased valley aggradation which slows erosion rates for some catchments. Additionally, the topographic metric, normalized channel steepness, is used to assess spatial patterns of erosion for other catchments. Resistant lithologies at the channel outlets keeps erosion rates low in some catchments despite higher normalized channel steepness in streams headed in erodible rock types. Lastly, small catchments positioned above large channel knickpoints are protected from increases in incision and have the lowest erosion rates for the whole region. This chapter sets the long-term erosional regime, outlining the regions of relative transience with respect to uplift and erosion within the westernmost Transverse Range.

Turning up the intensity of anthropogenic disturbance, I move offshore to Santa Cruz Island to probe patterns of soil coverage produced by short-timescale perturbations. In Chapter 4, I ask how landscape factors such as current vegetation coverage and underlying lithology affect hillslope response to anthropogenic perturbations over the last 140 years. Quantifying anthropogenic erosion is difficult without repeated measures of a landscape topography or spatially averaging measurement techniques (Wheaton et al., 2010; Williams, 2012; Rengers and Tucker, 2015; Purinton and Bookhagen, 2018). Additionally, vegetation presence slows anthropogenic erosion (Bastola et al., 2018), but how vegetation presence is influenced by lithology is less well understood. This work develops a novel, spatially explicit method for quantifying erosion from single-timepoint topography post-disturbance and tests this method on a catchment in the southwestern corner of Santa Cruz Island. The results are compared against vegetation and lithology maps to assess patterns of erosion. I show that the

patterning of recent erosion is strongly controlled by lithology. Furthermore, the underlying lithology corresponds to changes in vegetation presence and type on the landscape, which has feedbacks for the amount of on-going erosion. This work emphasizes the importance of lithology in determining the presence of soil and its thickness.

Finally, I target Sedgwick Reserve, an inland location experiencing a lower intensity anthropogenic disturbance, to probe the relative intensity of chemical weathering in the soil and measure flux of rock-derived nutrients to the soil. Chemical weathering is a fraction of the total denudation and therefore directly related to the balance between uplift and erosion. Chapter 5 focuses on a ridgecrest soil, a landscape position that is likely to be most closely tuned to the erosion rates I measure in the overall catchment. Although chemical weathering and the flux of rock-derived nutrients as a function of uplift, erosion, climate and lithology is well studied for putative rock-derived nutrients such as P (Vitousek et al,. 2003; Porder et al., 2007), this work probes how nitrogen (N) derived from the bedrock is incorporated into the ecosystem. Global models and catchment and pedon-scale research in wetter climates indicate that rock-derived N could provide a substantial portion of the total N budget (Morford et al., 2016a; Morford et al., 2016b; Houlton et al., 2018), but its importance in drier climates where weathering is limited is still unknown. In this chapter, I show that the flux of rock-derived nitrogen is small compared to surficial inputs. The low rock-derived N flux rate is likely due to low weathering rates in the semi-arid climate. This work provides context to the factors controlling the relative magnitude of chemical weathering in the Western Transverse Range.

Each individual chapter provides specific outcomes that contribute to the fields of geomorphology and soil science. In all I emphasize two major factors as controls on the way

landscapes adjust to both long- and short-timescale perturbations: 1) The current semi-arid climate dictates how soil is produced and where it moves along hillslopes and within watersheds, and 2) The erodibility of the underlying lithology sets how much soil can be produced and how erosion can be translated across catchments. This dissertation reinforces existing knowledge within the field of earth surface processes pertaining the to the production, transport, and storage of sediment on a transient landscape.

References

Bastola, S., Dialynas, Y.G., Bras, R.L., Noto, L.V., & Istanbulluoglu, E. (2018). The role of vegetation on gully erosion stabilization at a severely degraded landscape: A case study from Calhoun Experimental Critical Zone Observatory. Geomorphology, 308, 25-39.

DeVecchio, D. E., Heermance, R. V., Fuchs, M., & Owen, L. A. (2012). Climate-controlled landscape evolution in the Western Transverse Ranges, California: Insights from Quaternary geochronology of the Saugus Formation and strath terrace flights. Lithosphere, 4(2), 110-130.

Farris, A. (2017). Quantifying late Quaternary deformation in the Santa Ynez Valley, Santa Barbara County, California (Master's Thesis). Retrieved from PQDT Open from MAI 56/03M(E), Masters Abstracts International. (ISBN:9781369698480)

Gurrola, L. D., Keller, E. A., Chen, J. H., Owen, L. A., & Spencer, J. Q. (2014). Tectonic geomorphology of marine terraces: Santa Barbara fold belt, California. GSA Bulletin, 126(1-2), 219-233.

Houlton, B. Z., Morford, S. L., & Dahlgren, R. A. (2018). Convergent evidence for widespread rock nitrogen sources in Earth's surface environment. Science, 360(6384), 58-62.

Jennings, C.W., Gutierrez, C., Bryant, W., Saucedo, G., and Wills, C. (2010). Geologic Map of California, 2nd Edition. Department of Conservtion, California Geologic Survey, Sacremento, CA.

Jenny, H. (1941). Factors of soil formation. 281 pp. New York.

Kennett, J. P., & Ingram, B. L. (1995). A 20,000-year record of ocean circulation and climate change from the Santa Barbara basin. Nature, 377(6549), 510.

Metcalf, J. G. (1994), Morphology, chronology, and deformation of Pleistocene marine terraces, southwestern Santa Barbara County, California, M.S. thesis, Univ. of Calif., Santa Barbara.

Montgomery, D. R. (2001). Slope distributions, threshold hillslopes, and steady-state topography. American Journal of science, 301(4-5), 432-454.

Morford, S. L., Houlton, B. Z., & Dahlgren, R. A. (2016a). Geochemical and tectonic uplift controls on rock nitrogen inputs across terrestrial ecosystems. Global Biogeochemical Cycles, 30(2), 333-349.

Morford, S. L., Houlton, B. Z., & Dahlgren, R. A. (2016b). Direct quantification of long-term rock nitrogen inputs to temperate forest ecosystems. Ecology, 97(1), 54-64.

Morel, D., & Keller, E. (2017, October). Quaternary chronology and uplift of Gaviota Coast marine terraces, Southern California. Talk presented at the Geological Society of America Annual Meeting, Seattle, WA.

Porder, S., Vitousek, P. M., Chadwick, O. A., Chamberlain, C. P., & Hilley, G. E. (2007). Uplift, erosion, and phosphorus limitation in terrestrial ecosystems. Ecosystems, 10(1), 159-171.

Purinton, B., & Bookhagen, B. (2018). Measuring decadal vertical land-level changes from SRTM-C (2000) and TanDEM-X (~ 2015) in the south-central Andes. Earth Surface Dynamics, 6(4).

Rengers, F. K., & Tucker, G. E. (2015). The evolution of gully headcut morphology: a case study using terrestrial laser scanning and hydrological monitoring. Earth Surface Processes and Landforms, 40(10), 1304-1317.

Rockwell, T. K., Keller, E. A., Clark, M. N., & Johnson, D. L. (1984). Chronology and rates of faulting of Ventura River terraces, California. GSA Bulletin, 95(12), 1466-1474.

Vitousek, P., Chadwick, O., Matson, P., Allison, S., Derry, L., Kettley, L., Luers, A., Mecking, E., Monastra, V. & Porder, S. (2003). Erosion and the rejuvenation of

weathering-derived nutrient supply in an old tropical landscape. Ecosystems, 6(8), 762-772.

Wheaton, J. M., Brasington, J., Darby, S. E., & Sear, D. A. (2010). Accounting for uncertainty in DEMs from repeat topographic surveys: improved sediment budgets. Earth surface processes and landforms: the journal of the British Geomorphological Research Group, 35(2), 136-156.

Williams, R. (2012). DEMs of difference. Geomorphological Techniques, 2(3.2).

Chapter 2. Brief summary of the geographic, geomorphic, and human history of the western Transverse Range

1. Preface

This chapter covers a brief natural and human history of the region to set the stage for more targeted looks into landscape evolution and the factors which influence how change happens. This chapter is designed to give the reader a general understanding of the tectonic and erosional aspects of the westernmost part of the Transverse Range.

2. Geology and Tectonics

The coastal-positioning of the region over geologic-timescales creates a diverse set of lithologies in a region of active uplift over the last 5Ma. The westernmost extent of the Transverse Range in southern California runs between Santa Barbara and Gaviota along a tectonically active continental margin. Inland of the region, the Pacific plate meets the North American plate along the San Andreas Fault (right-lateral, strike-slip). The great bend in the San Andreas fault means that the Western Transverse Range is not only moving north but also experiencing compression. This compression is responsible for the mountain ranges and also extensive fault and fold system throughout the region (Fig. 1).

Much of the sedimentary lithologies within the Western Transverse Range resulting from several long periods of sedimentation in the region. Over much of the Cenozoic era the region was part of a large fore-arc basin associated with the oblique subduction of the Farallon plate underneath the North American plate. The forearc basin gradually filled with sediment that record the transition of the basin from marine to terrestrial as the basin shallowed (Minor et al., 2009). The spreading center associated with the Farallon plate intersected the North American Plate during the Oligocene and due to oblique contact,

formed a trans-tensional boundary. During this period, the Transverse Range began to rotate around an eastern axis (Kamerling and Luyendyk, 1979). The trans-tension associated with the proto-Pacific and North American plate boundary and also the rotation of the Transverse Range away from the North American plate produced basins, which were filled by extension related volcanism or basement-rock uplift (similar to "unroofing" processes in the Basin and Range today – Wemicke, 1992). This volcanism is associated with the Miocene volcanic suite on Santa Cruz Island and the subsequent "unroofing" explains the presence of Jurassic Age basement rocks such as the Santa Cruz Island Schist and Willows Diorite (Atwater, 1998). Additionally, early rotation is associated with uplift inland of the Transverse Range to form proto-San Rafael Mountains and expose accretionary arc metamorphosed rocks of the Franciscan Formation (Wahl et al., 1998).

The current landscape is a product of active compression and continued rotation of the Transverse Range over the last 5 Ma as the Pacific plate captured Baja California and forced the plate boundary to move inland of the Transverse Range. This collision and shift in plate boundary produced a bend in the San Andreas Fault and changed the region from extensional to compressional (Atwater, 1998; Minor et al., 2009). This compression is responsible for the uplift of the current Santa Ynez and San Rafael Mountains. Sedimentary units younger than 5.3 Ma are derived from uplifting, predominantly sedimentary terrain. Grain size variations indicate variation in the balance between uplift and erosion through the Pleistocene (Minor et al., 2009). Over the past 100 ka+, marine terraces along the coast are graded during interglacial highstands in sea level and then uplifted and exposed by sea-level fall during glaciation and the continued tectonic uplift in the region (Rockwell et al., 1992;

Minor et al., 2009; Muhs et al. 2014).

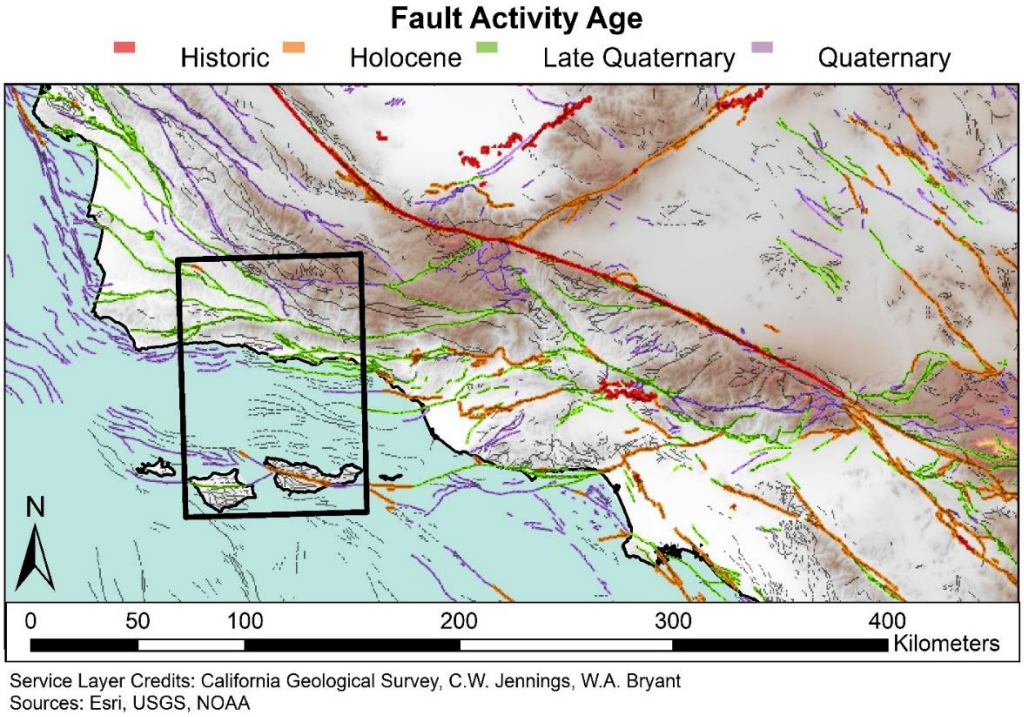

Figure 1. Fault activity age map for Southern California. The study region is outlined in black. The San Andreas Fault is red fault trending NW-SE across the study region. Mountainous topography is represented with dark brown shading.

3. Glacial and interglacial control on climate during late Pleistocene

Glacial and interglacial cycles over the last 100 ka set fluctuations in climate for the region. The arctic high moved southward with the expanse of glaciers, pushing low pressure systems into southern and central California (Thompson et al., 1993). These low pressure systems brought significantly more rain and drove transitions in the vegetation from Oak/Chaparral to Conifer forests. Evidence for wetter and cooler climates during glacial cycles can be inferred from pollen and paleolimnology data. Work from cores in the Santa Barbara and further south in San Bernardino County show fluctuations between Conifer forest (wetter climate) and Oak/Chaparral (drier - typical of current climate) that correspond to glacial and interglacial cycles (summarized by DeVecchio et al., 2014 from the works of

Huesser, 1995; 1998; Kirby et al 2006; 2007; Bird and Kirby, 2006). Wetter periods over the last 100 ka include 100-90 ka, 69-48 ka, 35-25 ka, and 18-11 ka. The 18 ka to 11 ka wet period was the most recent wet period and lasted from the last glacial maximum to the onset of the Holocene epoch. Fossilized Douglas Fir (*Pseudotsuga menziesii)* have been found on Santa Cruz Island in sedimentary deposits which date to 13-17 ka (Rick et al., 2014). Today, this tree species is only found in wetter ecoregions like Northern California, supporting a much wetter climate for the Western Transverse Range during the last glacial period.

4. Human land use

4.1 Overview

The region has been inhabited by indigenous peoples since 11 ka, but the arrival of European settlers in the late 1700's brought widespread land use change and triggered significant soil erosion in some areas. People made their way down the coast following the kelp highway and settled in the Western Transverse Range around 11 ka (Erlandson et al., 2007; Johnson et al., 2002) – descendants of these early settlers are the Chumash People. The Chumash thrived in the region for thousands of years; coastal populations lived off the abundant shallow marine life such as abalone, while inland populations incorporated native land-animals and acorns from the prevalent Oak communities into their diets (Arnold, 1992). The mainland Chumash performed prescribed burns to control native vegetation but the effects on the landscape and vegetation are generally assumed smaller in magnitude than the historic disturbances produced by European settlers (Timbrook et al., 1982).

The arrival of European settlers to the region in the late 1700's produced a rapid shift in land-use. The Chumash People were enslaved and removed from their land (Dart-Newton and Erlandson, 2006) and that land was converted into pasture for grazing sheep and cattle

(Barbour et al., 2007). This process included widespread removal of Oak, Chaparral, and Coastal Sage vegetation communities by burning and the introduction of shallow rooted, annual, invasive grasses like *Bromus spp.* and *Avena spp.* (Jackson et al., 2007). These land-conversion practices decreased soil cohesiveness and produced hillslope instabilities (Terwilliger and Waldron, 1991; Gabet and Dunne, 2003).

4.2 Study site specific land-use differences

The intensity of European land-use effects varies spatially within the region. Here I discuss the difference in intensity of European land-use between two locations that will be utilized in this dissertation: an offshore site discussed in Chapter 3 (Santa Cruz Island), and an inland site discussed in Chapter 5 (Sedgwick). On Santa Cruz Island, the stocking rates of ungulates was many times the typical rate on the adjacent mainland (Perroy et al., 2012). This severe overgrazing totally denuded the land of vegetation, pushing the landscape into a state of complete instability. Intense rain events in the late 1800's triggered widespread soil loss that continued until the complete removal of livestock in the early 2000's (Brumbaugh et al., 1982; Pinter and Vestal, 2005; Perroy et al., 2012). Today soil coverage is very patchy and varies significantly depending on vegetation and rock type, making it an ideal location to assess the interaction of a recent, high magnitude disturbance and varying soil forming factors. In contrast, it is likely that Sedgwick Reserve did not experience the same duration or severity of overgrazing as Santa Cruz Island because the landscape is still largely soil mantled. The reserve has been used for ranching since the early 1800's (UC-NRS, 2019), and consequently much of the reserve converted to annual grasslands from native Chaparral and Sage Scrub communities by the 1930's (Gabet and Dunne, 2002). However, the transition in vegetation did not push the landscape into total instability. Vegetation conversion is marked

by only an increase in landslides and not total evacuation of sediment from the hillslopes (Gabet and Dunne, 2003).

4. References

Arnold, J. E. (1992). Complex hunter-gatherer-fishers of prehistoric California: Chiefs, specialists, and maritime adaptations of the Channel Islands. *American Antiquity*, 57(1), 60-84.

Atwater, T. M. (1998). Plate tectonic history of southern California with emphasis on the western Transverse Ranges and northern Channel Islands. *Contributions to the Geology of the Northern Channel Islands, So. California*, Pacific Section of AAPG, p. 1-8.

Barbour, M., Keeler-Wolf, T., & Schoenherr, A. A. (Eds.). (2007). *Terrestrial vegetation of California*. Univ of California Press.

Brumbaugh, R. W., Renwick, W. H., & Loeher, L. L. (1982). *Effects of vegetation change on shallow landsliding: Santa Cruz Island, California*. General Technical Report PSW, 58.

Dartt-Newton, D., & Erlandson, J. (2006). Little choice for the Chumash: colonialism, cattle, and coercion in Mission Period California. *The American Indian Quarterly*, 30(3), 416-430.

Erlandson, J. M., Graham, M. H., Bourque, B. J., Corbett, D., Estes, J. A., & Steneck, R. S. (2007). The kelp highway hypothesis: marine ecology, the coastal migration theory, and the peopling of the Americas. *The Journal of Island and Coastal Archaeology*, 2(2), 161-174.

Gabet, E. J., & Dunne, T. (2002). Landslides on coastal sage-scrub and grassland hillslopes in a severe El Nino winter: The effects of vegetation conversion on sediment delivery. *GSA Bulletin*, 114(8), 983-990.

Gabet, E. J., & Dunne, T. (2003). A stochastic sediment delivery model for a steep Mediterranean landscape. *Water Resources Research*, 39(9).

Jackson, R. D., & Bartolome, J. W. (2007). *Grazing ecology of California grasslands*. California grasslands: ecology and management, 197-206.

Johnson, J. R., Stafford Jr, T. W., Ajie, H. O., & Morris, D. P. (2002, March). Arlington springs revisited. *Proceedings of the fifth California Islands Symposium* (pp. 541-545). Santa Barbara: Santa Barbara Museum of Natural History.

Kamerling, M. J., & Luyendyk, B. P. (1979). Tectonic rotations of the Santa Monica Mountains region, western Transverse Ranges, California, suggested by paleomagnetic vectors. *GSA Bulletin*, 90(4), 331-337.

Lambeck, K., & Chappell, J. (2001). Sea level change through the last glacial cycle. *Science*, 292(5517), 679-686.

Minor, S.A., Kellogg, K.S., Stanley, R.G., Gurrola, L.D., Keller, E.A., and Brandt, T.R., 2009, *Geologic Map of the Santa Barbara Coastal Plain Area, Santa Barbara County, California*: U.S. Geological Survey Scientific Investigations Map 3001, scale 1:25,000, 1 sheet, pamphlet, 38 p.

Muhs, D. R., Simmons, K. R., Schumann, R. R., Groves, L. T., DeVogel, S. B., Minor, S. A., & Laurel, D. (2014). Coastal tectonics on the eastern margin of the Pacific Rim: Late Quaternary sea-level history and uplift rates, Channel Islands National Park, California, USA. *Quaternary Science Reviews*, 105, 209-238.

Perroy, R. L., Bookhagen, B., Chadwick, O. A., & Howarth, J. T. (2012). Holocene and Anthropocene landscape change: arroyo formation on Santa Cruz Island, California. *Annals of the Association of American Geographers*, 102(6), 1229-1250.

Pinter, N., & Vestal, W. D. (2005). El Niño–driven landsliding and postgrazing vegetative recovery, Santa Cruz Island, California. *Journal of Geophysical Research: Earth Surface*, 110(F2).

Rick, T. C., Sillett, T. S., Ghalambor, C. K., Hofman, C. A., Ralls, K., Anderson, R. S., ... & Collins, P. W. (2014). Ecological change on California's Channel Islands from the Pleistocene to the Anthropocene. *BioScience*, 64(8), 680-692

Rockwell, T. K., Nolan, J., Johnson, D. L., & Patterson, R. H. (1992). Ages and Deformation of Marine Terraces Between Point Conception and Gaviota: Western Transverse Ranges, California. *Society for Sedimentary Geology*, Special Issue, No. 48.

Terwilliger, V. J., & Waldron, L. J. (1991). Effects of root reinforcement on soil-slip patterns in the Transverse Ranges of southern California. *GSA Bulletin*, 103(6), 775-785.

Thompson, R.S., Whitlock, C., Bartlein, P.J., Harrison, S.P., and Spaulding, W.G., 1993, *Climatic changes in the western United States since 18,000 yr B.P*. in Wright, H.E., Jr., Kutzbach, J.E., Webb, T. III, Ruddiman, W.F., Street-Perrott, F.A., and Bartlein, P.J. (Editors), Global climates since the last glacial maximum: University of Minnesota Press, pp. 468-513.

Timbrook, J., Johnson, J. R., & Earle, D. D. (1982). Vegetation burning by the Chumash. *Journal of California and Great Basin Anthropology*, 4(2).

Wahl, A. D., Naeser, N. D., Isaacs, C. M., & Keller, M. A. (1998). *Cenozoic deformation of the Franciscan Complex, eastern Santa Maria Basin, California*. Regional thermal maturity of surface rocks, onshore Santa Maria Basin and Santa Barbara-Ventura Basin area, California (No. 1995-W, X).

Wemicke, B. (1992). *Cenozoic extensional tectonics of the US Cordillera*. The Geology of North America, 3, 553-582.

UC-Natural Reserve System. (2019) *History of Sedgwick Reserve*. https://sedgwick.nrs.ucsb.edu/about/history

Chapter 3. Constraining long-term transience in the Western Transverse Range, CA

Key Points

- Cosmogenic nuclide derived erosion rates are low and relatively uniform across the Western Transverse Range (0.01-0.35 mm yr^{-1}).
- Uplift rates for inland and coastal regions of the westernmost portion of the Transverse Range, CA are an order of magnitude higher than the measured erosion rates.
- Lithologic erodibility variations coupled with a loss of erosive power during the Holocene help explain the low erosion rates.

Abstract

The balance between uplift and erosion sets current topography and the trajectory of topography over time. Imbalances between uplift and erosion can mean increased landslides, debris flows, or earthquakes. Additionally, the building or eroding of topography is intimately linked with the absence or presence of soil and its nutrient status. Therefore constraining rates of uplift and erosion are important for hazard and ecosystem health assessments. This study compares uplift rates to a new dataset of cosmogenic nuclide-derived erosion rates for the Transverse Range, CA and seeks to understand controls on the erosion rates. There is a mismatch between erosion rates and uplift rates for the inland and coastal regions of our study site – indicating a transience where uplift is outpacing erosion by an order of magnitude. Offshore at our study site, islands are uplifting slower and large catchments are eroding at approximately the same rate as uplift. Holocene-age climate drying has decreased stream power and increased valley aggradation which slows erosion rates for some catchments. Additionally, the topographic metric, normalized channel steepness, is used to assess spatial patterns of erosion for other catchments. Resistant lithologies at the channel outlets keeps erosion rates low in some catchments despite higher normalized channel steepness in streams headed in erodible rock types. Lastly, small catchments positioned above large channel knickpoints are protected from increases in incision and have the lowest erosion rates for the whole region.

1. Introduction

The Transverse Range physiographic province, in coastal southern California is a tectonically active region where localized uplift rates can exceed 5 mm yr^{-1} (Rockwell et al., 1992). It is also one of the most populous parts of California, with 11.4 million people in Santa Barbara, Ventura, and Los Angeles Counties (U.S. Census Bureau - Population Estimates Program, 2018). Understanding how tectonics and erosion create relief is necessary to estimate local natural hazards, particularly those related to flooding, debris flows and landslides. The rate of erosion also sets soil thickness (Heimsath et al. 1997) and determines soil nutrient availability (Vitousek et al., 2003) and hence fire fuel productivity. Since Transverse Range topography creates an important boundary condition to human habitation, it is important to understand the ongoing patterns of uplift and erosion in the region.

Tectonic activity in the region is related to transpression associated with movement on the San Andreas Fault. The Transverse Range block has been rotating clockwise around an eastern axis since 16 Ma (Kamerling and Luyendyk, 1979). Starting 5 Ma the Pacific-North American Plate boundary moved inland enhancing compression and creating stronger northward movement of the Transverse Range block. Ongoing transpression created a series of faults and folds through the area, locally uplifting the Santa Ynez Mountains (Atwater, 1998). Although mountain building and uplift in the Transverse Range has been well studied over 10^{4-6} year timescales (c.f. Rockwell et al., 1992; Blythe et al., 2000; Lindvall and Rubin, 2008; Gurrola et al., 2014; Farris 2017; Morel and Keller, 2017), there have been fewer studies of erosion rates at comparable spatial and temporal scales. The best examples come from the San Gabriel Mountains (DiBiase et al., 2010) and San Bernardino Mountains

(Binnie et al., 2007). This thesis provides a compilation of erosion rates for offshore, coastal, and inland regions at the western extremity of the Transverse Range (Fig. 1).

We utilize the erosion rate dataset for the westernmost Transverse Range to probe patterns of landscape evolution in the region. Relief of a landscape is set by the balance of uplift (U) rates and erosion (E) rates over geologic timescales (Hack, 1960). An imbalance between these two forces could mean building topography (U>E) or a wearing down of the landscape (U<E). At the watershed scale, the balance between U and E can vary, reflecting in changes in the local landscape morphology. Yoo et al. (2009) demonstrated spatial differences in U vs E on the hillslope scale, where actively eroding ridgecrests transition into depositional lower slopes in Tennessee Valley, CA. They argue that hillslopes are actively adjusting to a decreased erosion rate. In contrast, Marshal and Roering (2014) showed static differences in erosion rate set by alternating facies of resistant and less resistant rock. In this case, the average erosion rate for catchments with varying rock erodibility matched catchments in the area with less variability in rock strength. To assess net balance or imbalance, catchment average erosion rates are compared to long-term uplift rates.

Topographic metrics such as catchment slope, the normalized channel steepness index can be used to connect patterns in landscape morphology to the erosional regime (Wobus et al., 2006). At high uplift rates, hillslopes tend to reach a critical slope angle at which rather than further steepening, they change mode of erosion for instance by increasing frequency of landsliding (Montgomery and Brandon, 2002; DiBiase et al., 2010). Channels will continue to incise even after hillslopes reach their critical slopes (Burbank et al., 1996; Ouimet et al., 2009) - therefore quantifying channel steepness can provide insights into the

spatial patterns of erosion and uplift rates of a landscape (Whipple and Tucker, 1999; Wobus et al., 2006).

In this contribution, I assemble the first set of cosmogenic nuclide derived erosion rates for the western Transverse Range, compare them to existing uplift data, and provide a preliminary assessment of landscape evolution over geologic timescales based on the normalized channel steepness index and temporal shifts in regional climate. Finally, I discuss the potential implications of the long-term landscape evolution on soil production and rock-derived nutrient fluxes for the inland region in this study.

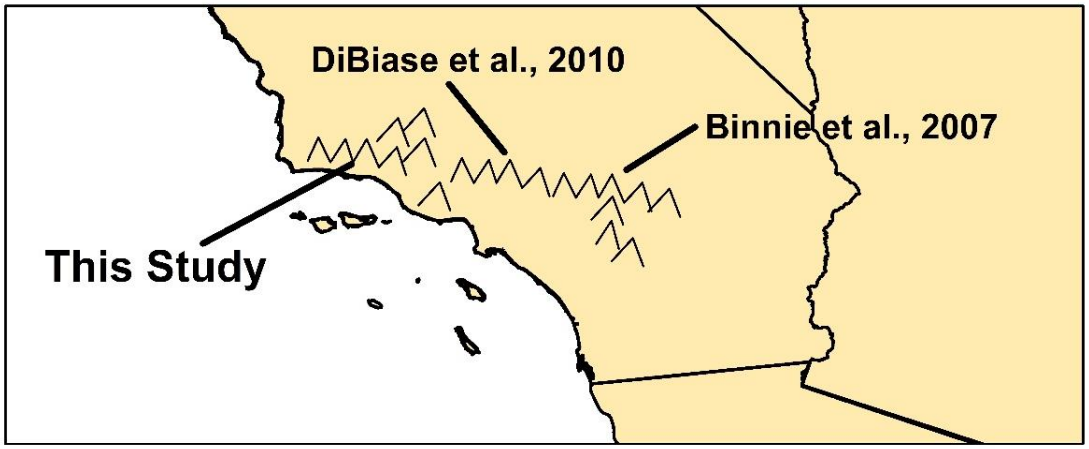

Figure 1. Cosmogenic nuclide derived erosion rate studies in the Transverse Range, CA.

2 Methods

2.1 Beryllium-10 derived catchment average erosion rates

2.1.1 Catchment location and underlying lithology

Samples for cosmogenic nuclide analysis were taken between 2014 – 2016 from channels in the greater Santa Barbara Region (Fig. 2), with a focus on inland (Catchments in and encompassing of Sedgwick UC Natural Reserve, in the Santa Ynez Valley; here called Sedgwick), coastal (Santa Barbara Coast from Gaviota to the mountains above downtown

Santa Barbara, here called SB Coast), and offshore (Santa Cruz Island, the largest of the western Channel Islands, here called SCI).

The lithologies within the region are largely sedimentary, with faulting bringing older metamorphic and volcanic rocks to the surface. Many of the catchments selected for erosion rate sampling do have some fine grain, non-quartz bearing facies, but either average large enough areas that the distribution of quartz bearing facies predominates or are small and entirely within a quartz bearing facies. These sampling locations were chosen for their proximity to on-going soil research projects in the region under the premise of providing a constraint on the geologic-timescale erosion rate.

Catchments at Sedgwick are located within the Santa Maria Basin, a wedge-shaped basin set by the Little Pine Fault to the NE and the Santa Ynez River Fault to the SW (Sylvester and Darrow, 1979). Their underlying lithology is dominantly the Paso Robles formation, a Pleistocene-age fanglomerate derived from the San Rafael Mountains. However the catchments initiate in the resistant Franciscan Formation, a Jurassic-age complex terrain consisting of serpentinite, greywacke, and greenstone (Dibblee, 1966). Samples were taken from. Most hillslopes grade to in-filled valleys and the current channels that were sampled cut into these in-filled valleys. We presumed most of the sediment supplied to the channel was derived from the valley fill.

The Santa Barbara catchments have head waters at the crest of the Santa Ynez Mountains in resistant, Eocene sedimentary units and flow southward through less resistant, Oligocene to Pliocene sedimentary units in the foothills and finally drain through more recent and less folded/faulted, Pleistocene and Holocene sedimentary deposits in the coastal plain (Minor et al., 2009). Rattlesnake, Upper Mission, and La Honda channel samples were taken

in the higher relief portion of the Santa Ynez Mountains. The channels at these sampling locations were bedrock-floored with patchy sediment coverage. San Pedro and Gaviota were sampled at channel mouths closer to the coast. These sampling locations targeted channels that cut into valley fill and these channels had more uniform sediment coverage.

The catchments on Santa Cruz Island are predominantly derived in fairly resistant, metamorphic and volcanic rocks. The headwaters of the catchments are derived from the Jurassic-aged SCI Schist, a chlorite greenschist that becomes red during weathering. The catchments then drain through the similarly aged, Willows Diorite, and Miocene-aged volcaniclastic sandstone/conglomerate known as the Blanca Formation, and finally the San Onofre Breccia at the outlets. Pozo and Sauces Catchments are built by north-south trending bands of the Blanca Formation in the headwaters and then more friable San Onofre Breccia, friable Canada Shale, and other minor shale and mudstone units downstream. These larger south- and west-draining catchments have significant valley fill in the main stem where cosmogenic nuclide samples were taken. The current channels cut into these valley fill deposits. The central valley sub-catchments on SCI are all derived from the SCI Schist (Dibblee, 1982). Samples were preferentially targeted to source small drainage areas above major catchment knickpoints. These samples were taken from 1st order streams with little to no valley in-filling.

2.1.2 Erosion rate calculations

Beryllium-10 accumulates over time in quartz exposed to cosmic rays. The flux of cosmic rays through surface regolith decreases rapidly with depth, such that the accumulation of 10Be within quartz is dependent on the cosmic ray flux and time spent by the mineral within the penetration zone – averaging over hundreds to thousands years depending on the

erosion rate (von Blanckenburg, 2005). Faster exhumation corresponds to lower concentrations of 10Be and slower exhumations rates lead to higher concentrations of 10Be in the mineral grains (Lal, 1991). Sampling sediment in the channel utilizes the natural routing of sediment through a landscape to spatially average the erosion within the watershed. Catchment average erosion rates can be inferred from sampling channel sediment as long as transport time is short relative to the amount of 10Be accumulated during transport (Granger et al., 1996). If there is an imbalance between long-term uplift and erosion such that sediment is eroded faster or slower than it is produced, the 10Be derived erosion rates from channel sands will reflect the time it takes to erode the 10Be enriched soil layer and some dilution via eroding deeper than the enriched soil thickness or enrichment via additional sediment storage time within the catchment.

Samples were cleaned and isolated following standard procedures adapted from Kohl and Nishiizumi (1992), von Blanckenburg et al. (2004), and Bookhagen and Strecker (2012). Samples from Sedgwick were measured at the PRIMELab (Purdue University) and Santa Cruz Island samples were measured at HZDR (Dresden, Germany). Calculating catchment average erosion rates from concentrations of 10Be in channel sands requires the cosmic ray production rate specific to the sample watershed (von Blanckenburg, 2005). The online Chronus-calculator (Balco et al., 2008) was used to convert 10Be concentrations into erosion rates. Although the Chronus calculator is designed for surface erosion rates at a point location, the range in elevation within our catchments is relatively low and the relative error on the rates by using an average elevation for an entire catchment is lower than the variation between rate estimates for the Western Transverse Range. I included an average shielding value for our erosion rate calculations. Shielding-weighting (ratio of production rate with

obstruction to production rate without obstruction) matrices are calculated to account for potential blocking of cosmogenic rays within the watershed by dense or high vegetation, ice or snow, and steep topography (Balco et al., 2008). The shielding matrices for the rates produced in this study was calculated using TopoToolbox (Schwanghart and Kuhn, 2010; Schwanghart and Scherler, 2014); because snow and ice are extremely rare in the study area, only a topographic shielding component was calculated. The erosion rates produced in association with this work (Results - Table 1) were estimated using the Lm-scaling scheme (Lal, 1991; Stone, 2000; Nishiizumi et al., 1989). Pre-existing rates for Santa Cruz Island and Coastal Santa Barbara region were produced utilizing spatially explicit altitude driven production rates (Results - Table 2).

2.2 Long-term uplift rates

Long-term uplift rates for the Western Transverse Range were derived from marine terraces on SCI and neighboring Channel Islands (Pinter et al., 1998; Muhs et al., 2014) and along the SB Coast from Gaviota to the Santa Barbara Cemetery (Gurrola et al., 2014; Morel and Keller, 2017). Inland, uplift rates were taken from a study on the fluvial terraces along Zaca Creek in the Santa Maria Basin/Santa Ynez Valley (Farris, 2017). These uplift rates were estimated by assuming the elevation of the terrace above sea level (marine) or active channel (fluvial) is equivalent to the amount of uplift the landscape underwent over the age of the terrace and therefore represent average uplift rates over the age of the terrace surface.

Dating of the marine terraces within the western Transverse Range was done by measuring carbon-14 concentration or the ratio between radioactive isotopes of Uranium and Thorium to derive dates on corals found within basal sediments of wave cut platforms (Pinter et al., 1998; Muhs et al., 2014). Optically stimulated luminescence (OSL) has also been used

to date terraces as it is sensitive to ~200kyr (Aitken, 1998; Botter-Jensen and Murray, 2001) and is useful for dating channel and coastal sands. When OSL is used, ages corresponds to the last exposure of basal sediments to sunlight and is therefore set by the burial time of sediment and subsequent uplift out of the active deposition-erosion area of the channel (Aitken, 1998; Botter-Jensen and Murray, 2001). Gurrola et al. (2014) and Morel and Keller (2017) both used OSL for dating coastal terraces and Farris (2017) used OSL for dating fluvial terraces in the Santa Maria Basin.

Constraining the elevation of a terrace involves several considerations. For the fluvial terraces in Santa Maria Basin, the authors assumed uplift matched incision on a hundred-thousand year timescale, such that the elevation above the active channel in Zaca Creek was produced by uplift rates (Farris, 2017; Pazzaglia et al., 1998). If channel incision is less than uplift rates over the age of the terrace, then the uplift rates estimated from terrace elevation are minimums. For coastal terraces, accounting for local sea level change over the time of the terrace age is key for accurately determining the uplift produced elevation of the terrace (Muhs et al., 2003). Morel and Keller (2017) utilized a localized eustatic sea level curve produced by Reynolds and Simms (2015) to model the elevation for the marine terraces. The authors of the uplift studies for the region did consider explicitly the folding and faulting activity within their study sites making it unlikely their localized uplift rates are faulty. However, the variable faulting and folding combine with few uplift data to make it difficult to confidently extrapolate locally measured values.

2.3 Landscape metrics to assess spatial patterns of erosion

2.3.1 Topographic Data and Topographic Data Software

Digital elevation models (DEMs) with resolutions of 10m and 30m were used to calculate topographic metrics for each of the catchments with a measured 10Be erosion rate. Digital elevation data was derived from the National Elevation Dataset (2002) in association with the United States Geological Survey. Topographic metrics were calculated using the Topographic Analysis Toolkit (Forte and Whipple, 2019) which runs in Matlab and utilizes an existing digital topography description toolkit, TopoToolbox (Schwanghart and Kuhn, 2010; Schwanghart and Scherler, 2014). Catchments were created using a D8 flow-routing scheme to determine a flow direction and flow accumulation raster from a sink-filled DEM, and outlets were assigned using the BasinPicker tool, which allows for a user selection of the basin outlet. Streams were delineated by an automated Chi-profile analysis using the FindThreshold function and channel heads initiated between $10^{4\text{-}6}$ m^2 of upstream area.

2.3.2 Normalized Stream Steepness Index

I used the topographic metric, normalized stream steepness index (K_{sn}), to help understand potential controls on erosion and uplift rates. Stream power erosion models set erosion rate, E, equal to upstream drainage area, A, channel steepness, S, and a coefficient that encompasses rock strength, channel composition, and flow rate distributions, K, (Eqn. 1; Sklar and Dietrich, 1998). In Equation 1, m and n are positive constants that encompass style of channel erosion, and hydraulic parameters (Whipple and Tucker, 1999).

Equation 1. $E = KA^m S^n$

Change in channel elevation over time can be approximated by the balance between channel bedrock uplift, U, and channel incision (Eqn. 2; Whipple and Tucker, 1999). If the rates of uplift and erosion are approximately equal, the change in elevation over time is zero and

uplift is equivalent to those factors effecting erosion (drainage area, channel steepness, erodibility of bedrock, climate, etc.).

Equation 2. $\frac{dz}{dt} = U - E;\ 0 = U - KA^m S^n;\ \mathrm{U} = KA^m S^n$

Equation 2 can be rearranged so that slope is a function of upstream drainage area, A, and equilibrium channel steepness, K_s, and concavity, Θ (Eqn. 3a; Wobus et al., 2006). Wobus et al. (2006) set the concavity as a constant in order to produce a normalized channel steepness, K_{sn}, metric which allows for comparison of channel steepness between catchments (Eqn. 3b). In this form of the equation $K_{sn} = (U/K)^{1/n}$ and increases in U lead to higher K_{sn} values whereas increases in K lead to lower K_{sn} values. If U=E and K is uniform across the catchment, K_{sn} is directly related to the uplift rate (c.f. DiBiase et al., 2010), however if U≠E and there is variability in K across the catchment, K_{sn} is a function of the factors which make up K (bedrock erodibility, climate, etc.) and can be used to interpret controls on erosion rate.

Equation 3a. $S = K_s A^{-\theta}$

Equation 3b. $S = K_{sn} A^{-\theta_{ref}}$

K_{sn} was calculated on stream networks using a reference concavity, Θ_{ref}, of 0.50 and the KsnChiBatch and ProcessRiverBasins functions in the Topographic Analysis Toolkit. The CompileBasinStats function was used to produce a catchment average K_{sn} value with standard error for each catchment of interest. I compared the catchment average Ksn values with our catchment average erosion rates.

3 Results

3.1 Comparison of measured catchment average erosion rates and uplift rates

I compare our measured erosion rates to existing uplift data to assess relative balance between uplift and erosion rates across the Western Transverse Range (Fig. 2). Existing

uplift rates were determined by dividing the elevation of marine and fluvial terraces by their surface ages. Uplift rates inland of the Santa Ynez Mountains are limited. Uplift rates from river terraces associated with Zaca Creek (two drainages to the NW from Sedgwick - c.f orange star on Fig. 2) were on the order of 0.9 to 1.1 mm yr^{-1} over the last 78 kyr (Farris, 2017). The uplift rates measured on marine terraces along the SB Coast between Point Concepcion and the Isla Vista (c.f. purple stars on Fig. 2) are 1.7-1.9 ±0.5 mm yr^{-1} over 37 kyr (Morel and Keller, 2017). Uplift rates for the SB Coast between Ellwood and the Santa Barbara Mesa are 1.1 – 2.0 mm yr^{-1} over the last 39-53 kyr and at the far end of our study site 0.40 mm yr^{-1} over 79 kyr at the Santa Barbara Cemetery (c.f. pink stars on Fig. 2 - Gurrola et al., 2014). The current uplift rates for Santa Cruz Island are between 0.1 and 0.2 mm yr^{-1} over the last ~120 kyr (SCI rates, c.f green stars on Fig. 2 - Pinter et al., 1998).

The cosmogenic nuclide derived erosion rate dataset shows relatively similar rates throughout the Western Transverse Range; averaging over a timescale of ~8.5 kyr. The catchment average erosion rates from Sedgwick (Table 1) are 0.12-0.15 mm yr^{-1}, an order of magnitude slower than the uplift rates determined for the region. Similar to Sedgwick catchments, the erosion rates for the Santa Barbara Coast (Table 2) are an order of magnitude slower than uplift rates along the SB Coast: 0.15 – 0.35 mm yr^{-1} erosion vs 1-2 mm yr^{-1} uplift. In contrast, erosion rates for the south-draining catchments of Santa Cruz Island (Table 2) are roughly equivalent to the uplift rates for the island: 0.1 mm yr^{-1} erosion vs 0.1-0.2 mm yr^{-1} uplift. Sauces catchment and the north-draining sub-catchments of the central valley of Santa Cruz Island (Table 1) are an order of magnitude slower than the uplift rates for the island and some of the slowest measured for the Transverse Range at 0.006 to 0.016 mm yr^{-1}.

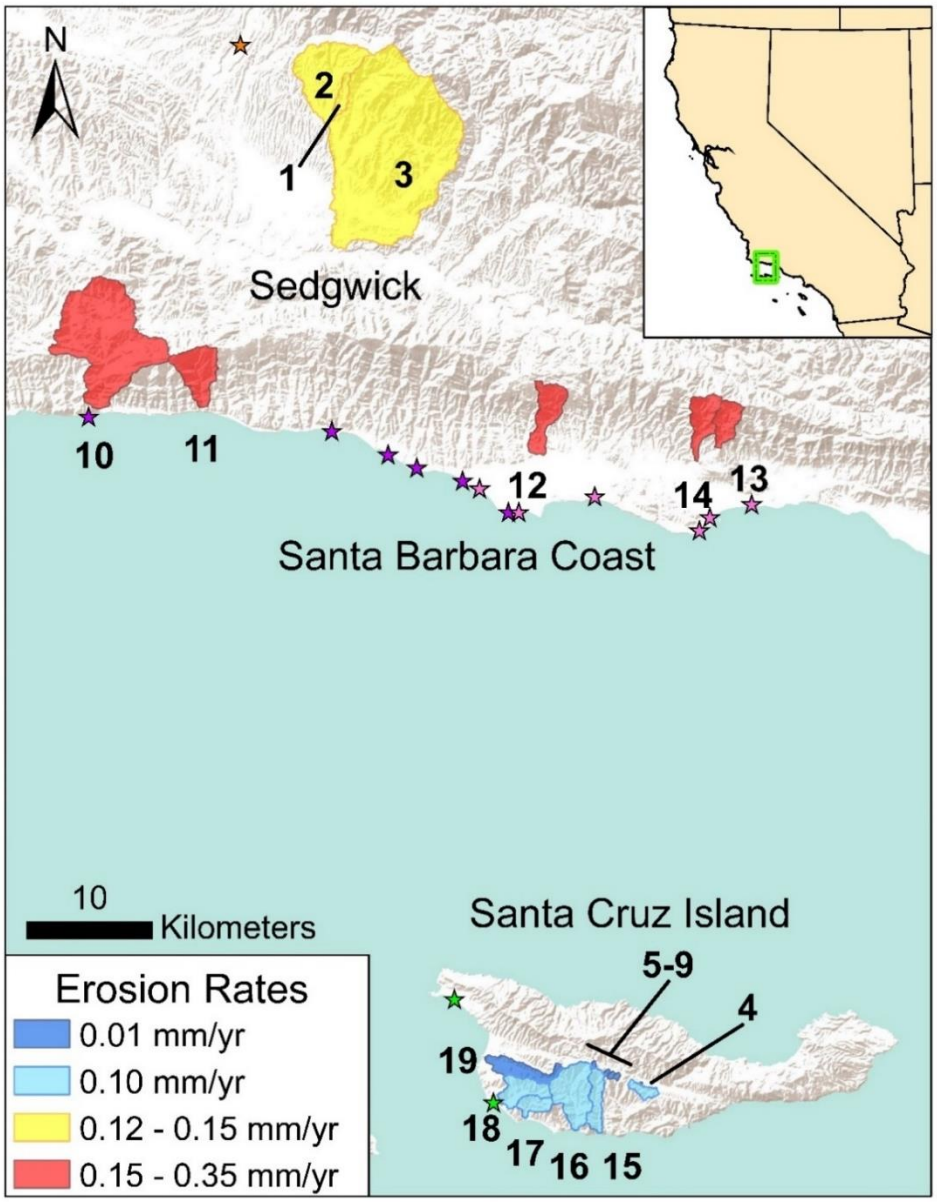

Figure 2. Watersheds in the Western Transverse Range with cosmogenic nuclide derived catchment average erosion rates and sampling locations for uplift rate studies in the region. Erosion rates are produced in associated with this dissertation are for Sedgwick (WC, FC, SA in Table 1) and the north-draining watersheds in Santa Cruz Island (SCI_ in Table 1). Pre-existing cosmogenic nuclide data is for the south-draining watersheds of Santa Cruz Island and for the Santa Barbara coastal region (Table 2). Colored stars indicate locations with dated terraces used for determining uplift rates. Colors indicate study: Green – Pinter et al., 1998; Pink – Gurrola et al., 2014; Purple – Morel and Keller, 2017; Orange – Farris, 2017.

Table 1. Watershed characteristics, measured 10Be concentrations, estimated erosion rates for watersheds within the Santa Maria Basin and the central valley of Santa Cruz Island. Shielding was estimated for SA catchment due to the size of the watershed and computer memory.

Watershed	Area (km^2)	Max Z (m asl)	Mean Z (m asl)	Mean Shielding	Be-10 (atoms g^{-1})	Uncertainty (atoms g^{-1})	Lm Erosion Rate (mm yr^{-1})
WC -1	2.30	694	454.3	0.9918	25431	1002	0.155±0.019
FC - 2	23.65	1037	502.7	0.9902	27138	1243	0.143±0.019
SA - 3	144.93	1404	491.9	~0.99	32451	1862	0.122±0.019
SCI3_4 - 4	1.87	426	257.5	0.938	28577	1307	0.100±0.013
SCI8_6 - 5	0.21	422	341.8	0.939	474008	11317	0.006±0.001
SCI7_1 - 6	0.04	273	217.9	0.930	439911	13489	0.006±0.001
SCI2_11 - 7	0.27	443	351.2	0.938	199967	6236	0.015±0.002
SCI2_12 - 8	0.18	441	358.9	0.940	301094	877	0.010±0.001
SCI2_13 - 9	0.19	448	386.6.	0.957	282831	9412	0.011±0.001

*Table 2. Existing cosmogenic nuclide derived catchment average erosion rates***.**

Watershed	Area (km^2)	Max Z (m asl)	Mean Z (m asl)	Mean Shielding	Be-10 (atoms g^{-1})	Uncertainty (atoms g^{-1})	Erosion Rate (mm yr^{-1})
Gaviota - 10	19.90	703.66	191.26	-	-	-	0.342±0.22
La Honda - 11	11.24	870.65	437.69	0.997	33000	750	0.158±0.010
San Pedro - 12	10.45	880.06	300.22	0.998	29000	1100	0.169±0.0.012
Rattlesnake Canyon - 13	8.13	1161.06	627.40	0.995	29000	800	0.214±0.015
Upper Mission - 14	7.40	1212.58	696.79	0.995	30000	950	0.193±0.013
Laguna – SCI - 15	12.46	459.16	195.91	-	-	-	~0.10*
LS – SCI - 16	5.03	454.27	205.44	-	-	-	~0.10*
Johnson – SCI - 17	3.29	459.16	159.60	-	-	-	~0.10*
Pozo – SCI - 18	6.45	405.42	151.89	0.992	43000	1160	0.101±0.007
Sauces – SCI - 19	6.07	397.99	181.14	0.989	84000	1200	0.051±0.003
*Laguna, Ls, and Johnson are estimated rates awaiting final results							

3.2 Landscape morphology

This section explores the relationship between K_{sn}, erosion rate, and environmental parameters (underlying lithology). Catchment average comparisons are useful for assessing differences between larger spatial areas – e.g. elucidating how K_{sn} and catchment average erosion rates change between Sedgwick and the SB Coast. Spatially explicit K_{sn} provides an in-depth look for each catchment on how environmental parameters affect the balance

between uplift and erosion. In our case, because climate is relatively constant through the region, I will compare breaks in K_{sn} with changes in underlying lithology.

Catchment average values of normalized stream steepness compared with the average slope of the catchment show three distinct groupings: 1) high K_{sn} and medium erosion rates, 2) low K_{sn} and medium erosion rates, and 3) low K_{sn} and low erosion rates (Fig. 6). The first grouping has catchments from the SB Coast. This grouping also has the largest standard error. The second grouping contains catchments from SB Coast, Sedgwick, and the south-draining catchments from SCI. The group of low K_{sn} values with medium erosion rates has varied standard error; SB Coast catchment has more (similar to grouping 1), while SCI and Sedgwick have less. The third group encompasses the central valley sub-catchments from SCI. These catchments are very small (~0.1 km^2) and therefore contain only one stream segment as part of the K_{sn} calculation and these catchments do not have standard error. Lastly, the Gaviota catchment on the SB Coast plots away from other catchments with respect to average erosion rate and K_{sn}, with the highest erosion rate (0.35 mm yr^{-1}) and a low K_{sn}.

A spatial map of K_{sn} values underlain by general rock type for each region helps elucidate the relationship between erosion rate and stream steepness (Fig. 7). Wider ranges of K_{sn} (<50 to >250) and the highest K_{sn} values (>250) are found in catchments on the SB Coast and in Sedgwick. This is in contrast to catchments on SCI which have a more narrow range in K_{sn} (<50 to 150) and generally lower K_{sn} values (<150). Major shifts in normalized channel steepness changes occur at contacts between lithologic units (shifts in grey – Fig. 7) in Sedgwick, Santa Barbara Coast, and the farthest west of the south-draining catchments on Santa Cruz Island (Pozo and Sauces). The rest of the south-draining catchments on SCI show

minimal differences in K_{sn} across the different lithologies. The Gaviota catchment on the SB Coast shows a break in channel steepness towards the headwaters of this catchment which is notable because it is not related to a change in lithology.

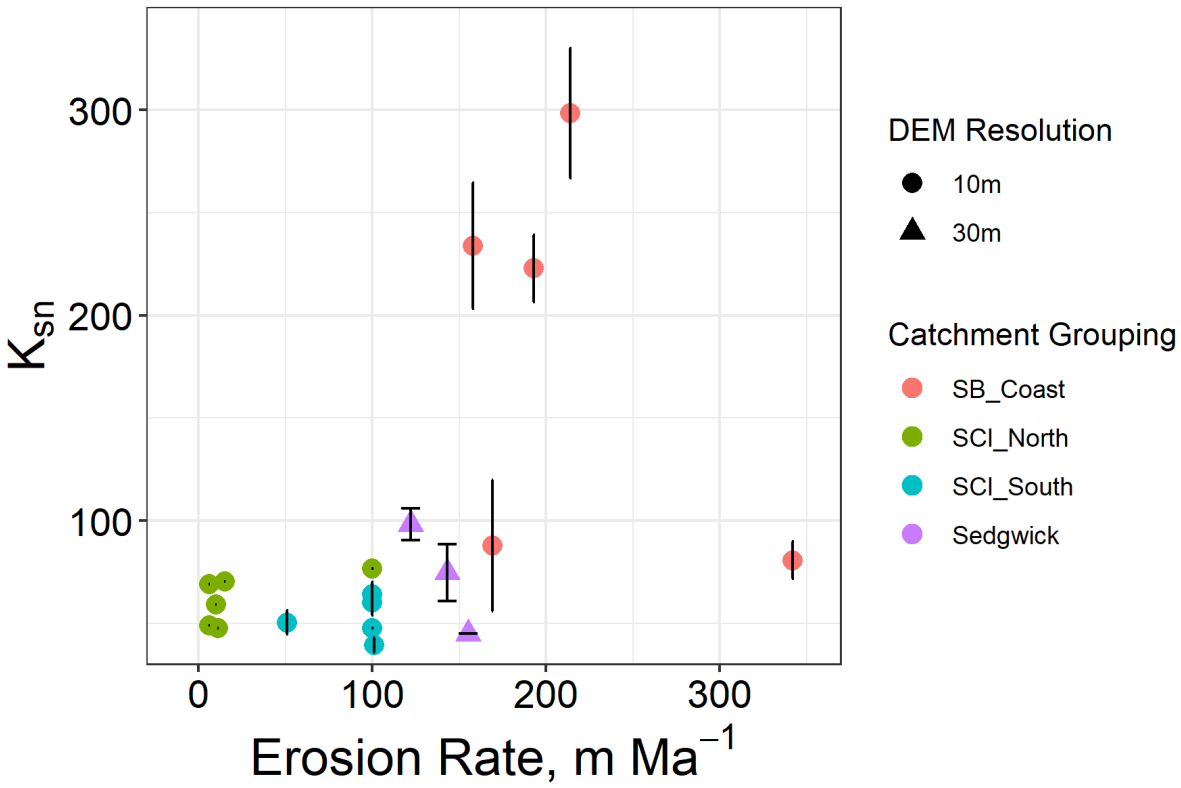

Figure 6. Catchment average erosion rates compared to the normalized stream steepness index. Standard error on K_{sn} is represented by the vertical black bars.

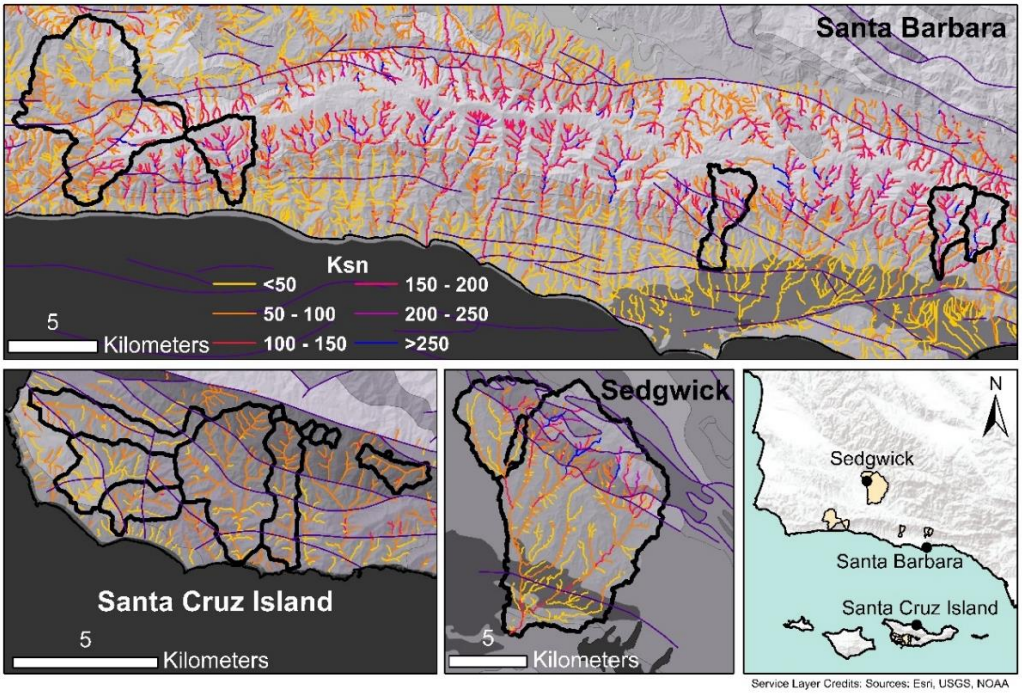

Figure 7. Normalized stream steepness index, K_{sn}, compared with fault and geologic contacts for the Western Transverse Range. K_{sn} is not computed for the small, north-draining sub-catchments on SCI because these catchments are too small for the raster resolution (30m) and upstream area to compute meaningful steepness indices.

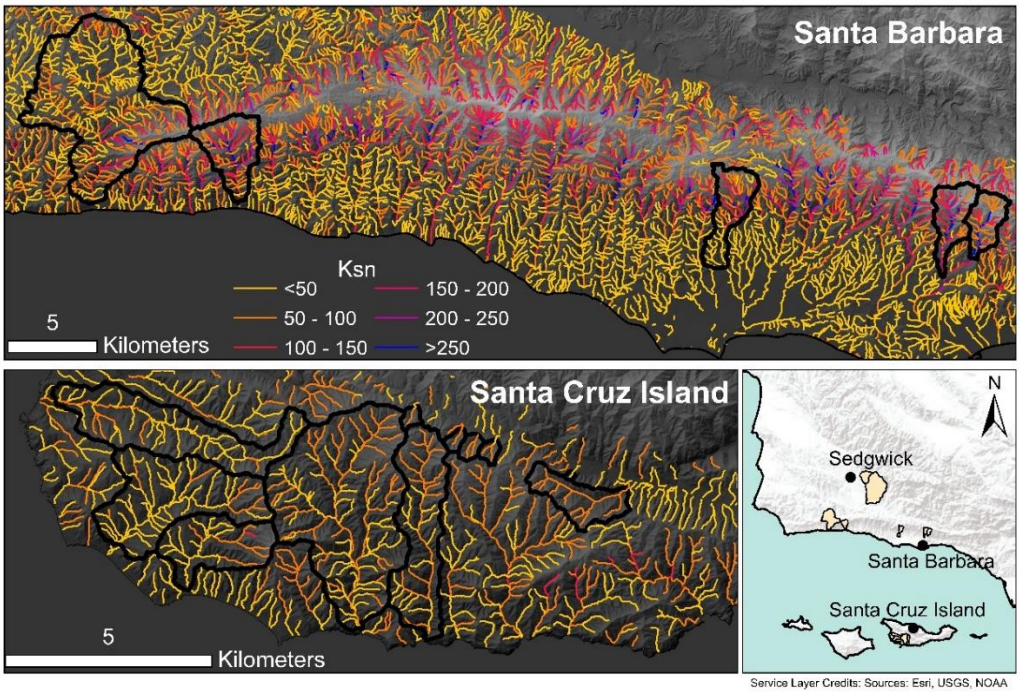

Figure 8. Normalized stream steepness index, K_{sn}, for SCI and SB Coast calculated with a 10m DEM. This map is included to show K_{sn} values for the central valley sub-catchments of SCI.

4 Discussion

In this section I explore how the measured erosion rates may reflect several controls on landscape morphology and evolution unique to the Western Transverse Range. Additionally, I consider the potential implications of low catchment average erosion rates on soils research in the Western Transverse Range. The imbalance between uplift and erosion rates in the Western Transverse Range is in contrast to other regions in the Transverse Range, such as the San Gabriel Mountains to the east. In the San Gabriel Mountains 10Be-derived erosion rates ranged from 0.035 to 1.10 mm yr^{-1} and generally matched long-term exhumation rates, indicating a landscape steady-state over geologic timescales (DiBiase et al., 2010). In our study site, our erosion rates are at the lower end of the range of rates for San Gabriel Mountains (0.1-0.3 mm yr^{-1}) despite more uniformly high uplift rates (1-2 mm yr^{-1}, SCI excluded) over at least the last ~100 kyr. While climate is more consistent across the Western Transverse Range than the Eastern Transverse Range (the San Gabriel Mtns.), temporal shifts in climate over the timescale of uplift (last 100 kyr) may affect the current erosion rates. Furthermore, the variation in lithology within catchments and across the region is significant, especially compared to the more uniform ranges to the east (San Gabriel and San Bernardino Mtns are largely granitic). If weatherability of the underlying bedrock varies, then the lithology could also control erosion rates and landscape evolution. We explore these two ideas in further detail in the following section.

4.1 Climate and lithologic influence on erosion rates

4.1.1 Climate driven increase in valley sediment storage

Slower erosion rates in some catchments could be caused by an increase in the amount of sediment stored on hillslopes and in valleys over the averaging timescale of 10Be accumulation. The accumulation of 10Be averages over a timescale set by the cosmic ray

penetration depth (600 – 900 mm depending on rock or soil) divided by the estimated erosion rate. Therefore, using a penetration depth of 850 mm (typical soil – von Blanckenburg, 2005) and an erosion rate of 0.1 mm yr^{-1} means averaging erosion over 8,500 years. The climate shifted to warmer and drier conditions at the onset of the Holocene (11,200 years ago, Kennet and Ingram, 1995). Climate-drying induced loss of stream power lead to valley aggradation in the area, especially from 11.2 to 4 kyr (DeVecchio et al., 2012). Valley aggradation increases the storage time between soil production and transport out of the catchment via stream. More 10Be will accumulate in sediment stored in the valley before making its way to the channel. This would produce a catchment average erosion rate that encompasses both the hillslope transport and valley storage time instead of just the assumed hillslope transport time.

The influence of climate-drying driven valley storage on erosion rates would be most dominate valley fill deposits defined the banks of the channel and bank slumps and failures contribute valley fill sediment to the stream. The catchments within our study where excessive valley fill may be enriching the catchment average 10Be concentration are the Sedgwick catchments and the south- and west-draining catchments on SCI. These samples were all taken within channels that cut through in-filled valleys and hillslopes generally graded to these filled-valleys and not the cut channel. In contrast, catchments in the San Gabriel Mountains were chosen specifically with minimal valley aggradation, therefore the rates produced were not likely sensitive to storage time effects (DiBiase et al., 2010).

It is possible to estimate hillslope erosion rates from measured catchment average erosion rates. This would require determining the accumulation of 10Be in the valley sediment over the period of accumulation for the region (≤11.2kyr – onset of Holocene). This

simplest form of the calculation requires the assumption that the current active channel receives all of its sediment from valley fill and specifically surficial valley fill (sediment within the cosmic ray penetration depth). These calculations are beyond the current scope of this dissertation but would be important for more spatially explicit erosion rate studies.

4.1.2 Bedrock erodibility controls landscape morphology

In our study-site, topographic metrics are largely related to changes in bedrock erodibility instead of erosion rate. The normalized stream steepness index is directly related to the uplift rate for a region only if 1) uplift rates are equal to erosion rates and 2) rock type and climate are uniform throughout the landscape. For our study region, uplift rates are much faster than erosion rates and there is considerable variability in the lithology, which means the connection between K_{sn} and uplift is complicated. The order of magnitude difference in uplift rate between the mainland and the Channel Islands is reflected in the range and maximum K_{sn}; rapidly uplifting areas (Sedgwick and SB Coast) have wider ranges of K_{sn} and higher max K_{sn} compared to areas of slower uplift (SCI). However, the most noticeable spatial pattern with K_{sn} is the in-catchment shifts from high K_{sn} to low K_{sn} at rock type boundaries. In the Santa Ynez Mountains in the SB Coast, much of the lower and middle reaches of the steeper terrain areas are underlain by resistant Eocene units and have higher K_{sn}. K_{sn} declines when the channels cut into less resistant Oligocene-Pliocene formations in the foothills and coastal plains (Duvall et al., 2004). This pattern also holds for the Sedgwick catchments; resistant rocks in the upper reaches and less resistant rocks downstream. The Sedgwick region catchments headwaters are underlain by the more resistant Franciscan Formation, built mostly of metamorphic rocks formed during the subduction of the Farallon Plate underneath the North American Plate 150 to 15 Myr. K_{sn} is high in areas underlain but

Franciscan units but drops dramatically in the downstream Paso Robles Formation, a poorly consolidated fanglomerate produced by streams draining the San Rafael Mountains.

The spatial correlation of K_{sn} with rock type helps explain the dynamics between some groupings of average K_{sn} and erosion rate (c.f. Fig 6). The cluster of catchments with high K_{sn} and medium erosion rates (La Honda, Upper Mission, and Rattlesnake for SB Coast) are situated primarily within the high relief portion of the Santa Ynez Mountains and have downstream stretches that run through resistant units. Interestingly, the head waters of some of these catchments are within more erodible mudstones and shales. The K_{sn} declines slightly where the headwaters are in more erodible lithologies, but is still steeper than in areas underlain by erodible lithologies closer to the coast (headwaters of Rattlesnake vs lower reaches of San Pedro). The higher standard error for catchment average K_{sn} may reflect the variation in the erodibility of the rock type even through the K_{sn} is relatively steep. Catchments with high average K_{sn} and large standard error, and similar erosion rates to catchments with lower average K_{sn} may be a product of resistant lithologic units holding up the less resistant lithologic units upstream during uplift and slowing the translation of increases in incision from the channel mouths over time.

4.1.3 Sampling locations target relic landscapes - Sub-catchments of SCI Central Valley

The sub-catchments underlain solely by Mesozoic age chlorite schist (SCI Schist) in the central valley of Santa Cruz Island are small (<0.3 km^2 excluding SCI3-4). These small sub-catchments have similar Ksn as may other catchments in the region but have erosion rates an order of magnitude lower than the inferred uplift rates for the island and the erosion rates for the larger watersheds that share a ridgeline (c.f. Fig. 2 and 6). These rates are some

of the slowest in the western Transverse Range (c.f. Table 1; 2). The largest sub-catchment, SCI3-4, has an erosion rate which matches those of the south-draining SCI catchments.

The orientation of the sub-catchments and the sampling location for each sub-catchment influences the measured erosion rates. The sampling locations for the sub-catchments (blue dots, Fig. 7a) are all either upstream of a major main channel knickpoint (green star, Fig. 7a) or right below a minor knickpoint for a tributary. The exception to this is SCI3-4 which is sampling the largest sub-catchment for the central valley (position-wise, this catchment is also the most connected to the ocean). The positioning of the small sub-catchment samples preferentially targets relic landscapes; these are regions isolated from base level shifts such as sea-level change or fault activity which may increase erosion rates.

Comparing the small, north-facing sub-catchments and the adjacent south-facing catchments that share the ridgeline shows that local climate may also influence the erosion rates. Aerial imagery shows higher vegetation density on the slowly eroding, central valley sub-catchments than the faster eroding, larger catchments, implying a potential moisture difference between the two groups of catchments (Fig. 7a). Solar insolation differences set by aspect does influence soil moisture content which can corresponds to vegetation differences (Carson and Kirkby, 1972; Geroy et al., 2011). In turn, this is been shown to influence hillslope morphology (Istanbulluoglu et al., 2008; Johnstone et al., 2017) and consequently differences in sediment transport rates. Polar-facing slopes tend to be steeper, have deeper soils, and erode more slowly (West et al., 2014). Distributions of slope derived from a 5m DEM show north-draining slopes have a more narrow spread and higher mean slope than south-draining slopes for areas underlain by the SCI Schist (Fig. 7b). It is entirely plausible that relic landscapes of the small, central valley sub-catchments have erosion rates further

impeded by higher soil moisture leading to more consistent vegetation coverage which slows sediment transport. It would be enticing to probe differences in relic soil depth and the depth of anthropogenic incision between the headwaters of the south-draining catchments and the north-draining central valley sub-catchments.

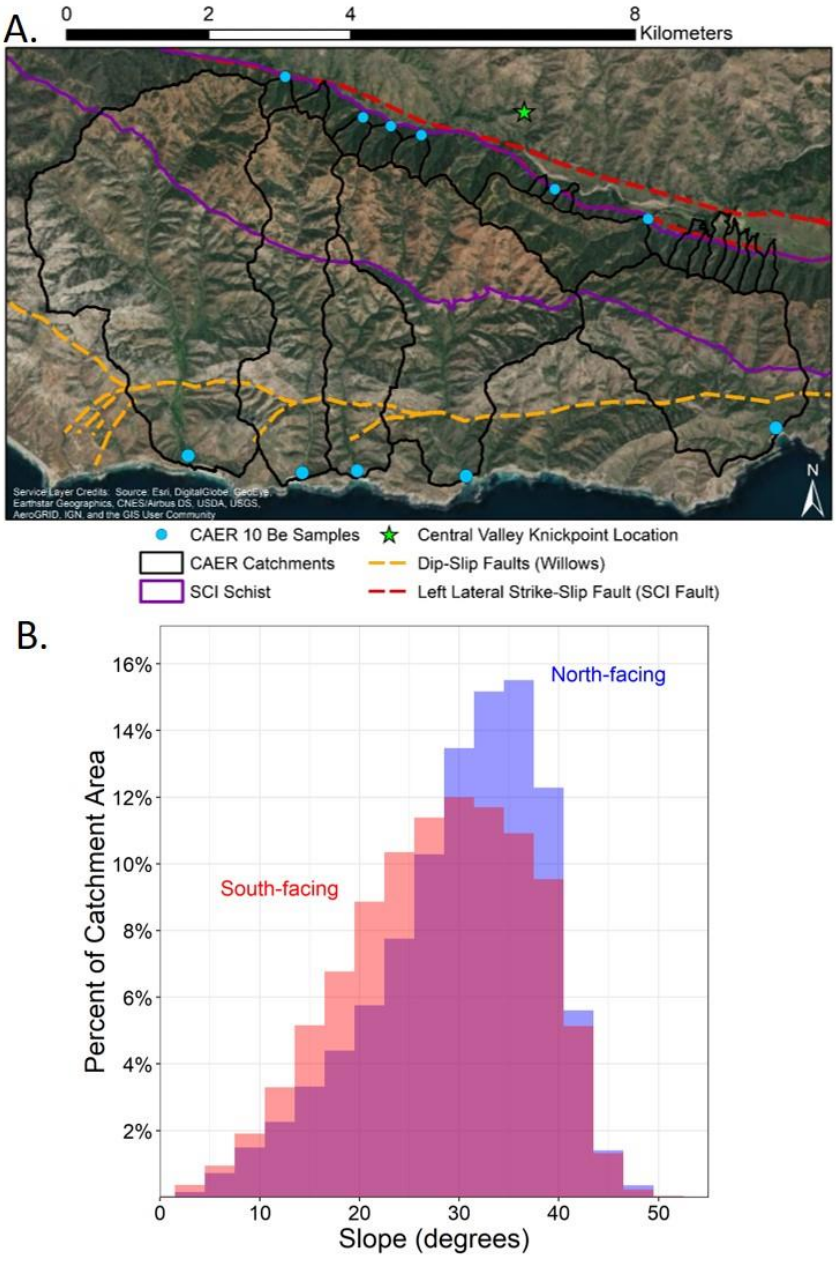

Figure 7. A. Aerial imagery of SCI catchments with fault system, SCI Schist, and CRN sampling points outlined. B. The distribution of slopes in areas underlain but SCI Schist and partitioned by dominant aspect.

4.2 Implications for soils geochemical research at Sedgwick

Parts of this dissertation pertain to bedrock weathering and estimating fluxes of rock derived nutrients from the bedrock to the landscape at a ridgecrest position (See Chapter 5). Previous literature that estimates bedrock weathering and the fluxes of rock derived nutrients from the bedrock to the landscape use total denudation rates as a proxy for soil production rates. These denudation rates in conjunction with a metric for chemical weathering losses, are used to calculate a chemical weathering flux (Reibe et al., 2003; Yoo et al., 2009; Morford et al., 2016). Typically, the total denudation rate is measured by 10Be derived catchment average erosion rate and the landscape is assumed to be in steady-state (uplift matches erosion), such that catchment average erosion rates are equivalent to soil production rates. At Sedgwick, climate drying at the onset of the Holocene is assumed responsible for an increased in valley fill which in turn increases the storage time of sediment between hillslopes and the channel. This increase in storage time allows for extra 10Be to accumulate in the aforementioned infilled concave and downslope areas of hillslopes. These infilled valleys are a typical feature of much of California' grasslands, last excavated at the onset of the Holocene between 9,000 - 14,000 years (Reneau et al., 1990). Given the magnitude difference between our measured catchment average erosion rates and the uplift rates determined for the Santa Maria Basin, a blanket assumption of steady-state and application of catchment average rates as soil production rates at Sedgwick would be erroneous.

It is likely that the actual soil production rate is between the measured uplift rates (high endmember, 1 mm yr^{-1}) and the measured 10Be catchment average erosion rate (low endmember, 0.12 mm yr^{-1}). Soil production rates of 1 mm yr^{-1} would be notoriously high for an entirely soil mantled landscape (Heimsath et al., 2012), and especially a soil that shows enough pedogenic development to classify as an Mollisol. Additionally, the previously

discussed influence of valley fill may be driving down the catchment average erosion rate. Therefore, hillslopes are likely eroding faster than the measured catchment average rate. Future work on this project will include calculations of the valley fill 10Be enrichment to the catchment average rate in order to back out a hillslope soil erosion rate/soil production rate.

5 Conclusions

The balance between erosion and uplift sets the topography of a landscape and the trajectory of landscape evolution (Hack, 1960). This work seeks to understand landscape evolution for the westernmost Transverse Range, CA. Our study provides a new dataset of cosmogenic nuclide derived erosion rates and compares these rates with uplift rates for the region. The westernmost Transverse Range is in a state of transience with respect to the balance between uplift and erosion over long timescales, with uplift rates an order of magnitude higher than erosion rates in most locations.

We sought to explain low erosion rates through inferences about sampling location, paleoclimate and paleo-stream power, and also spatial patterns of landscape morphology metrics. Climate-drying driven valley in-filling increases sediment storage time which in turn would decrease the rate of catchment average erosion. This effect is only significant in catchments where hillslopes supply sediment to an in-filled valley and the valley feeds sediment to the incised channel. We found that magnitude differences in uplift between the mainland and SCI were reflected in the normalized channel steepness index, K_{sn}. Also K_{sn} tracked changes in lithology erodibility for some catchments. Catchments had higher average K_{sn} values if resistant rock types underlain the downstream portions. We interpret this as resistant rock types protecting less resistant rock types from increases in erosion, creating steep streams during higher rates of uplift. Lastly, smaller isolated catchments in our study

area may preserve very low erosion rates if samples are taken in locations targeted for relic landscapes.

The valley infill and variability in rock erodibility do not explain erosion rates and landscape morphology for all catchments. The west- and south-draining SCI catchments show relatively small changes in K_{sn} despite shifts in lithology. This is reflected in the small standard error for the average K_{sn} values. Gaviota catchment along the SB Coast has the highest erosion rates measured for the region but a low average K_{sn} with a small standard error despite varying lithology throughout the catchment. Gaviota also has some portions of the catchment with in-filled valleys that contribute sediment to the channel. These exceptions point towards interactions between the aforementioned controls or other, different controls on erosion rate which require further study.

References

Atwater, T. M. (1998). Plate tectonic history of southern California with emphasis on the western Transverse Ranges and northern Channel Islands. Contributions to the Geology of the Northern Channel Islands, So.California, Pacific Section of AAPG, p. 1-8.

Aitken, M.J., 1998, An Introduction to Optical Dating: The dating of Quaternary sediments by the use of photon-stimulated luminescence. Oxford, United Kingdom, Oxford University Press, 267 p.

Balco, G., Stone, J. O., Lifton, N. A., & Dunai, T. J. (2008). A complete and easily accessible means of calculating surface exposure ages or erosion rates from 10Be and 26Al measurements. Quaternary geochronology, 3(3), 174-195.

Binnie, S. A., Phillips, W. M., Summerfield, M. A., & Fifield, L. K. (2007). Tectonic uplift, threshold hillslopes, and denudation rates in a developing mountain range. Geology, 35(8), 743-746.

Blythe, A. E., Burbank, D. W., Farley, K. A., & Fielding, E. J. (2000). Structural and topographic evolution of the central Transverse Ranges, California, from apatite fission track,(U–Th)/He and digital elevation model analyses. Basin Research, 12(2), 97-114.

Bookhagen, B., and Strecker, M.R. (2012): Spatiotemporal trends in erosion rates across a pronounced rainfall gradient: examples from the southern Central Andes. Earth and Planetary Science Letters, 327-8, 97-110.

Botter-Jensen, L., and Murray, A.S., 2001, Optically stimulated luminescence techniques in retrospective dosimetry. Radiation Physics and Chemistry, 61(3-6), 181-190.

Burbank, D. W., Leland, J., Fielding, E., Anderson, R. S., Brozovic, N., Reid, M. R., & Duncan, C. (1996). Bedrock incision, rock uplift and threshold hillslopes in the northwestern Himalayas. Nature, 379(6565), 505.

Carson, M. A., & Kirkby, M. J. (1972). Hillslope form and process. New York, Cambridge University Press, 476 p.

DiBiase, R. A., Whipple, K. X., Heimsath, A. M., & Ouimet, W. B. (2010). Landscape form and millennial erosion rates in the San Gabriel Mountains, CA. Earth and Planetary Science Letters, 289(1-2), 134-144.

Dibblee, T. W. (1966). Geology of the central Santa Ynez Mountains, Santa Barbara County, California (Vol. 186). California Division of Mines and Geology.

Dibblee Jr, T. W. (1982). Geology of the Channel Islands, southern California. Geology and Mineral Wealth of the California Transverse Ranges, Mason Hill Volume, South Coast Geological Society, Santa Ana, California, 27-39.

Duvall, A., Kirby, E., & Burbank, D. (2004). Tectonic and lithologic controls on bedrock channel profiles and processes in coastal California. Journal of Geophysical Research: Earth Surface, 109(F3).

Farris, A. (2017). Quantifying late Quaternary deformation in the Santa Ynez Valley, Santa Barbara County, California (Master's Thesis). Retrieved from PQDT Open from MAI 56/03M(E), Masters Abstracts International. (ISBN:9781369698480)

Forte, A. M., & Whipple, K. X. (2019). The Topographic Analysis Kit (TAK) for TopoToolbox. Earth Surface Dynamics, 7(1), 87-95.

Geroy, I. J., Gribb, M. M., Marshall, H. P., Chandler, D. G., Benner, S. G., & McNamara, J. P. (2011). Aspect influences on soil water retention and storage. Hydrological Processes, 25(25), 3836-3842.

Granger, D. E., Kirchner, J. W., & Finkel, R. (1996). Spatially averaged long-term erosion rates measured from in situ-produced cosmogenic nuclides in alluvial sediment. Geology, 104(3), 249-257.

Gurrola, L. D., Keller, E. A., Chen, J. H., Owen, L. A., & Spencer, J. Q. (2014). Tectonic geomorphology of marine terraces: Santa Barbara fold belt, California. GSA Bulletin, 126(1-2), 219-233.

Hack, J. T. (1960). Interpretation of erosional topography in humid temperate regions. Bobbs-Merrill.

Heimsath, A. M., DiBiase, R. A., & Whipple, K. X. (2012). Soil production limits and the transition to bedrock-dominated landscapes. Nature Geoscience, 5(3), 210.

Istanbulluoglu, E., Yetemen, O., Vivoni, E. R., Gutiérrez-Jurado, H. A., & Bras, R. L. (2008). Eco-geomorphic implications of hillslope aspect: Inferences from analysis of landscape morphology in central New Mexico. Geophysical Research Letters, 35(14).

Johnstone, S. A., Chadwick, K. D., Frias, M., Tagliaro, G., & Hilley, G. E. (2017). Soil development over mud-rich rocks produces landscape-scale erosional instabilities in the northern Gabilan Mesa, California. GSA Bulletin, 129(9-10), 1266-1279.

Kamerling, M. J., & Luyendyk, B. P. (1979). Tectonic rotations of the Santa Monica Mountains region, western Transverse Ranges, California, suggested by paleomagnetic vectors. GSA Bulletin, 90(4), 331-337.

Kohl, C.P., and Nishiizumi, K., (1992): Chemical isolation of quartz for measurement of in situproduced cosmogenic nuclides. Geochimica et Cosmochimica Acta, 56, 3583–3587.

Lal, D. (1991). Cosmic ray labeling of erosion surfaces: in situ nuclide production rates and erosion models. Earth and Planetary Science Letters, 104(2-4), 424-439.

Lindvall, S. C., & Rubin, C. M. (2008). Slip Rate Studies along the Sierra Madre–Cucamonga Fault System Using Geomorphic and Cosmogenic Surface Exposure Age Constraints: Collaborative Research with Central Washington University and William Lettis & Associates, Inc. US Geological Survey final report 03HQGR0084, 13.

Minor, S.A., Kellogg, K.S., Stanley, R.G., Gurrola, L.D., Keller, E.A., and Brandt, T.R., 2009, Geologic Map of the Santa Barbara Coastal Plain Area, Santa Barbara County, California: U.S. Geological Survey Scientific Investigations Map 3001, scale 1:25,000, 1 sheet, pamphlet, 38 p.

Montgomery, D. R., & Brandon, M. T. (2002). Topographic controls on erosion rates in tectonically active mountain ranges. Earth and Planetary Science Letters, 201(3-4), 481-489.

Morel, D., & Keller, E. (2017, October). Quaternary chronology and uplift of Gaviota Coast marine terraces, Southern California. Talk presented at the Geological Society of America Annual Meeting, Seattle, WA.

Morford, S. L., Houlton, B. Z., & Dahlgren, R. A. (2016). Geochemical and tectonic uplift controls on rock nitrogen inputs across terrestrial ecosystems. Global Biogeochemical Cycles, 30(2), 333-349.

Muhs, D. R., Wehmiller, J. F., Simmons, K. R., & York, L. L. (2003). Quaternary sea-level history of the United States. Developments in Quaternary Sciences, 1, 147-183.

Muhs, D. R., Simmons, K. R., Schumann, R. R., Groves, L. T., DeVogel, S. B., Minor, S. A., & Laurel, D. (2014). Coastal tectonics on the eastern margin of the Pacific Rim: Late Quaternary sea-level history and uplift rates, Channel Islands National Park, California, USA. Quaternary Science Reviews, 105, 209-238.

National Elevation Dataset; 2002; Web site; U.S Geological Survey

Nishiizumi, K., Kubik, P. W., Elmore, D., Reedy, R. C., & Arnold, J. R. (1989). Cosmogenic Cl-36 production rates in meteorites and the lunar surface. In Lunar and Planetary Science Conference Proceedings, 19, 305-312.

Ouimet, W. B., Whipple, K. X., & Granger, D. E. (2009). Beyond threshold hillslopes: Channel adjustment to base-level fall in tectonically active mountain ranges. Geology, 37(7), 579-582.

Pazzaglia, F. J., Gardner, T. W., & Merritts, D. J. (1998). Bedrock fluvial incision and longitudinal profile development over geologic time scales determined by fluvial terraces. Geophysical Monograph-American Geophysical Union, 107, 207-236.

Pinter, N., Lueddecke, S. B., Keller, E. A., & Simmons, K. R. (1998). Late quaternary slip on the Santa Cruz Island fault, California. GSA Bulletin, 110(6), 711-722.

Reneau, S. L., Dietrich, W. E., Donahue, D. J., Jull, A. T., & Rubin, M. (1990). Late Quaternary history of colluvial deposition and erosion in hollows, central California Coast Ranges. GSA Bulletin, 102(7), 969-982.

Reynolds, L. C., & Simms, A. R. (2015). Late Quaternary relative sea level in southern California and Monterey Bay. Quaternary Science Reviews, 126, 57-66.

Rockwell, T. K., Keller, E. A., Clark, M. N., & Johnson, D. L. (1984). Chronology and rates of faulting of Ventura River terraces, California. GSA Bulletin, 95(12), 1466-1474.

Rockwell, T. K., Nolan, J., Johnson, D. L., & Patterson, R. H. (1992). Ages and Deformation of Marine Terraces Between Point Conception and Gaviota: Western Transverse Ranges, California. Society for Sedimentary Geology, Special Issue, No. 48.

Schwanghart, W., & Kuhn, N. J. (2010). TopoToolbox: A set of Matlab functions for topographic analysis. Environmental Modelling & Software, 25(6), 770-781.

Schwanghart, W., & Scherler, D. (2014). TopoToolbox 2–MATLAB-based software for topographic analysis and modeling in Earth surface sciences. Earth Surface Dynamics, 2(1), 1-7.

Sklar, L., & Dietrich, W. E. (1998). River longitudinal profiles and bedrock incision models: Stream power and the influence of sediment supply. American Geophysical Union (AGU), 237-260.

Stone, J. O. (2000). Air pressure and cosmogenic isotope production. Journal of Geophysical Research: Solid Earth, 105(B10), 23753-23759.

Sylvester, A. G., & Darrow, A. C. (1979). Structure and neotectonics of the western Santa Ynez fault system in southern California. In Developments in Geotectonics, 13, 389-403.

U.S. Census Bureau, Population Estimates Program (PEP). V2018. Accessed April 2019. https://www.census.gov/quickfacts/fact/table/losangelescountycalifornia,venturacountycalifornia,santabarbaracountycalifornia/PST045218

Vitousek, P., Chadwick, O., Matson, P., Allison, S., Derry, L., Kettley, L., Luers, A., Mecking, E., Monastra, V. & Porder, S. (2003). Erosion and the rejuvenation of weathering-derived nutrient supply in an old tropical landscape. Ecosystems, 6(8), 762-772.

von Blanckenburg F., Hewawasam T., and Kubik P. (2004): Cosmogenic nuclide evidence for low weathering and denudation in the wet tropical Highlands of Sri Lanka. Journal of Geophysical Research, 109(F03008).

von Blanckenburg, F. (2006). The control mechanisms of erosion and weathering at basin scale from cosmogenic nuclides in river sediment. Earth and Planetary Science Letters, 242(3-4), 224-239.

West, N., Kirby, E., Bierman, P., & Clarke, B. A. (2014). Aspect-dependent variations in regolith creep revealed by meteoric 10Be. Geology, 42(6), 507-510.

Whipple, K. X., & Tucker, G. E. (1999). Dynamics of the stream-power river incision model: Implications for height limits of mountain ranges, landscape response timescales, and

research needs. Journal of Geophysical Research: Solid Earth, 104(B8), 17661-17674.

Wobus, C., Whipple, K. X., Kirby, E., Snyder, N., Johnson, J., Spyropolou, K., Crosby, B. & Sheehan, D. (2006). Tectonics from topography: Procedures, promise, and pitfalls. Special papers - Geological Society of America, 398(55).

Yoo, K., Mudd, S. M., Sanderman, J., Amundson, R., & Blum, A. (2009). Spatial patterns and controls of soil chemical weathering rates along a transient hillslope. Earth and Planetary Science Letters, 288(1-2), 184-193

Chapter 4. Use of lidar point-cloud data to assess human-induced erosion and loss of vegetation cover on contrasting lithologies

Key Points:

- Lidar point-cloud data provide high resolution measurement of soil and bedrock erosion linked to anthropogenic perturbations

- We developed innovative ways to measure 1) erosion without time-series data, and 2) vegetation cover across an eroded landscape.

- We found distinct erosion patterns that correlate with underlying lithology and show lithology dependent patterns of vegetation cover.

Abstract

Santa Cruz Island, California has experienced human-induced erosion over the last 140 years. In order to measure this erosion, we process irregular point-cloud data into 1-m resolution regular grids and measure incision depth using a moving-window algorithm. We also rely on rasterized return intensity data to map vegetation cover at the sub-meter spatial scale. Changes in incision and vegetation cover are mapped against total drainage area to assess spatial patterns of erosion. The size of the moving window can be tuned to detect relatively small erosion features while ignoring broad watershed-scale fluvially carved topography. Patterns of incision and vegetation cover depend primarily on the underlying lithology. Non-vegetated areas underlain by a mechanically weak shale exhibit deeply incised, active erosion features with less plant cover, whereas areas underlain by physically resistant volcaniclastics have shallower incision features with vegetation present in incised areas, indicative of a stabilized landscape. Lidar-derived, area-averaged erosion rates or the last 140 years are 1.93, 1.79, and 1.70 mm yr^{-1} for shale, breccia, and volcaniclastic lithologies, respectively. These rates are an order of magnitude larger than millennial time scale erosion rates and support previous, local centennial timescale erosion-rate measurements. This work demonstrates a method for capturing high-resolution patterns of erosion in catchments that lack pre-erosion topographic data and are currently responding to changing erosive pressure.

1 Introduction

Human-induced direct and indirect perturbations to ecosystems can trigger damaging soil erosion (Verstraeten et al., 2017). Land development for agriculture, industry, and housing are all linked to destabilization of soil (Hooke, 2000; Montgomery, 2007), which has increased global river sediment load by as much as 2.3 billion metric tons each year since the 1950's (Syvitski et al., 2005). A notable regional example of soil erosion is the gullying of valley floors and hillslopes in the mid-continent and southwestern United States in the late 1800's (Cooke & Reeves, 1976). Settlers across Colorado, Arizona, and New Mexico noted the expansion of gullies, with incision likely starting earlier in Colorado (1860-70) than in much of Arizona (1880) (Bryan, 1925). While gullying is typical across the western United States, as evidenced by Holocene cut-and-fill-sequences (Bettis & Thompson, 1985; Waters & Haynes, 2001), the most recent cycle of incision has been associated with landscape destabilization from human land use with erosion triggered by extreme rain storms (Bull & Kirkby, 1997; Hereford, 1993; Perroy et al., 2012). In 2018, severe storms produced deadly mudslides and gullying in central California after the area burned the month before in a late-season forest fire (Donnellan et al., 2018)). Forest fires and associated erosion are expected to increase in the future due to anthropogenic global warming (Sankey et al., 2017). These examples demonstrate the need to quantify human-induced erosion and understand factors controlling landscape response to it.

Erosion is typically quantified by differencing repeated topographic models of a region (Wheaton et al., 2010; Williams, 2012; Rengers and Tucker, 2015; Purinton and Bookhagen, 2018). For instance, Anderson et al. (2015) quantified landslide and mudflow

driven erosion in the Colorado Front Range after intensive rains in the Fall of 2013 by differencing lidar-produced gridded elevation surfaces. Wheaton et al. (2010) followed the erosional evolution of the river Feshie in Scotland over multiple years by differencing ground-surveyed topographic data, while also demonstrating the variability in spatial uncertainty during differencing techniques. Topographic model differencing can be an effective means to quantify erosion, however if an initial datum is not available, then it is necessary to reconstruct a pre-incised surface using other means (Small and Anderson, 1998).

The resolution of available topographic data sets the level of detail that can be captured in a reconstructed surface. This paper utilizes lidar point-cloud data for reconstructing pre-incised surfaces. Lidar point-clouds are irregular spatial data with commonly 1-30 return points within a square meter (Reutebuch et al., 2005). These data are often converted to gridded digital elevation models (DEMs) with a regular point-spacing that often range between 1 and 5 m depending on data density and application needs (Fernandez et al., 2007; Passalaqua et al., 2015; Roering et al., 2007). Lidar point-cloud data provide dozens of detailed topographic measurements per unit area where a gridded DEM would provide only one average elevation measurement (Brasington et al., 2012). Therefore, calculation of topometrics such as surface roughness using lidar point-clouds can resolve differences in topography at the sub-meter scale. For instance, Rychkov et al. (2012) used point-cloud produced surface roughness estimates of channel bottoms to determine grain size

distributions. The use of lidar point-cloud data for topographic analyses provides an opportunity to quantify erosion.

Lidar data not only provide topographic information, but also single-wavelength intensity information of surface objects. Depending on laser wavelength, they can be used to identify surface characteristics such as vegetation, buildings, and roads (Reutebuch et al., 2005; Wang and Glenn, 2009). Identifying vegetation presence within an eroding landscape is important given the role vegetation often plays in controlling the frequency and style of erosion (Istanbullouglu and Bras, 2005). Revegetation of eroding areas can reverse soil loss (Bastola et al., 2018; Vanacker et al., 2007), but feedbacks among precipitation, erosion, and vegetation complicate this seemingly simple relationship. Vegetation presence and density can be evaluated using lidar intensity data and, when coupled with lidar elevation-derived erosion measurements, can provide insight into the spatial relationships between vegetation and erosion.

Here we develop a method to use high-resolution lidar point-cloud data to separate long-term landscape-shaping erosion patterns from those imposed by recent human-influenced erosion. To do this, we calculate a surface elevation difference, or surface roughness, to estimate incision depths [m], integrate these incision-depth estimates spatially to estimate total incision [m^3], and divide these total volumes of incision by area and time to produce erosion rates [mm yr^{-1}]. Given the important connections between vegetation and erosion remediation (Istanbullouglu & Bras, 2005), we also identify vegetation via return intensity from the lidar beam at a wavelength 1064 nm. We then apply the method to quantify erosion losses from a recently disturbed landscape on Santa Cruz Island, California.

We first evaluate the algorithm results on a sub-catchment where anthropogenic erosion was previously quantified using hand-delineation techniques (Perroy et al., 2010; 2012), and then quantify erosion across a larger watershed, comparing erosion at different total drainage areas, vegetation cover, and across a variety of lithologies. Combining the algorithm-produced incision maps with field observations and valley deposit dates makes it possible to estimate lost sediment volumes and erosion rates. We determine spatially resolved estimates of recent erosion without timeseries topographic data, validate these estimates given constraints set by field observations on the dimensions of recent erosional features, and explore spatial patterns of erosion with respect to lithology and vegetation.

2 Geographic, Geomorphologic, and Geologic Setting

We test our methods on an eroded watershed underlain by three distinctly different lithologies; the Cañada Shale, the San Onofre Breccia, and the Blanca Volcaniclastics. Pozo Catchment is located on the southwestern coast of Santa Cruz Island (SCI), California (Fig. 1a). The island is the largest (249 km^2) of the Northern Channel Islands, which sit off the coast of Santa Barbara (Fig. 1a-inset) (Dibblee, 2001a, 2001b). The current uplift rates for the northern Channel Islands are between 0.1 and 0.2 mm yr^{-1}. The uplift values are derived from calculated uplift rates using marine terraces on Santa Cruz Island (Pinter et al., 1998) and on neighboring Channel Islands (Muhs et al., 2012, 2014). These long-term uplift rates are corroborated by catchment average erosion rates taken from Holocene and present-day sediments (Perroy et al., 2012). Previous studies of tectonic geomorphology on the island indicate distinctive knickpoints and knickpoint migration associated with marine-wave cut platforms, lithologic changes, and drainage capture (Neely et al., 2017). Prior to the late

1800's, US Coast Survey maps and rancher accounts verify little erosion (especially gullying) within our study catchment, however, since then soil loss has been pervasive (Perroy et al., 2012).

In Pozo Catchment, hillslopes were destabilized by overgrazing and erosion was triggered by particularly heavy rainfall events (Perroy et al., 2012). Sheep were introduced to the island in the 1830's and populations rapidly increased to a maximum in the late 1800's with populations estimated at 40-50 thousand sheep roaming the island, largely unrestricted. While sheep were the largest population of ungulates, the island simultaneously hosted smaller populations of feral pig and managed cattle (Perroy et al., 2012). During this period of high-intensity grazing, vegetation was decimated, creating exposed soil surfaces (Van Vuren & Coblentz, 1987). In 1878 a series of storms enhanced erosion rates by an order of magnitude over long-term Holocene rates (Perroy et al., 2010; 2012). Ungulate eradication started in the early 1900's, however grazing (and soil loss - Pinter and Vestal, 2005) continued to some degree until 2006 (Parkes et al., 2010). Today, the remaining vegetation, and that which has recovered since the end of grazing on the island varies in type and presence dramatically depending on the underlying lithology (Baguskas et al., 2014; Cohen et al., 2009; Jones et al., 1993).

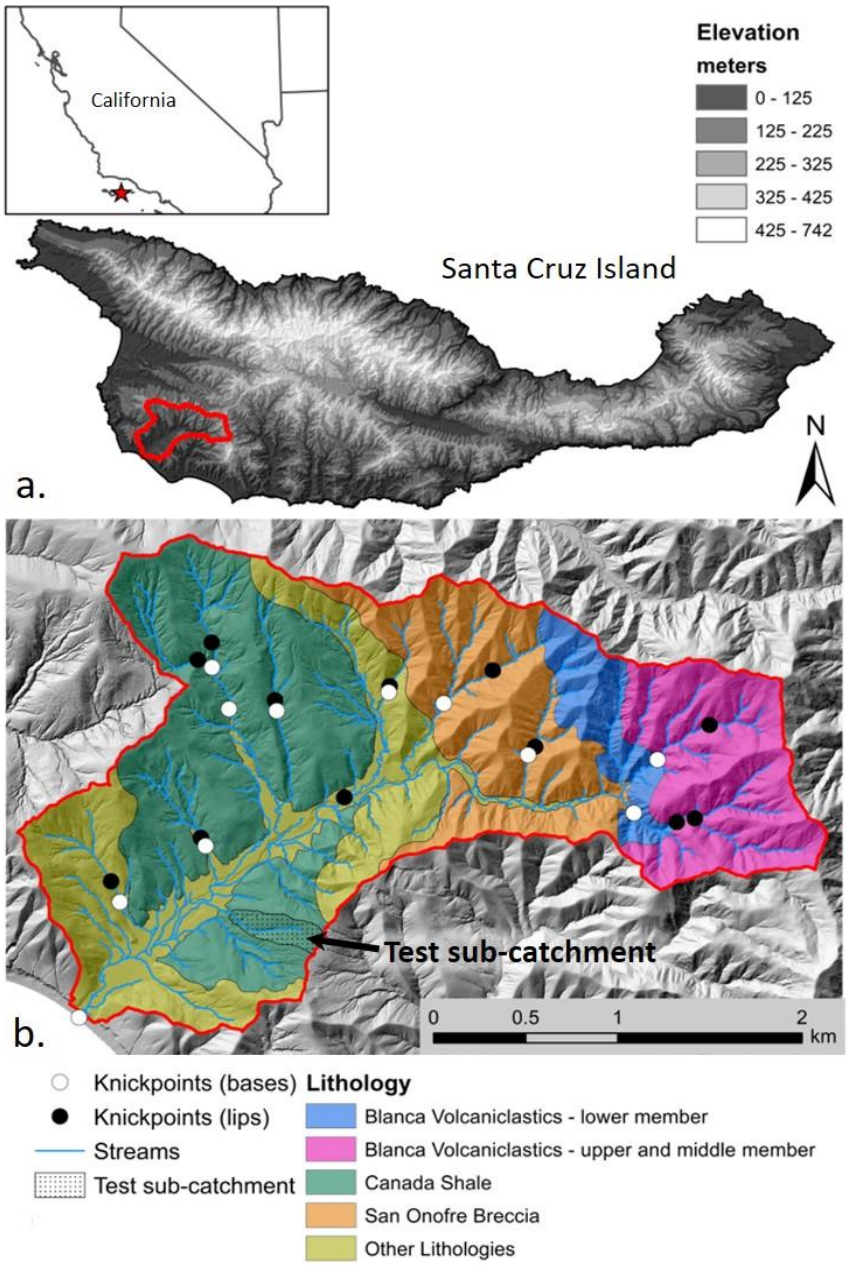

Figure 1. a. Elevation data for Santa Cruz Island with the Pozo watershed highlighted in red. a-inset, Santa Cruz Island (star) with respect to the California coast. b. Hillshade of Pozo Catchment, colored by major lithologies (modified after Dibble, 2001a) and the approximate stream network (drainage area > 10^4 m^2). Knickpoint/zone lips and bases are shown as identified by the KZ-Picker (Neely et al., 2017). Our test sub-catchment for algorithm exploration is colored with stippling.

3 Methods

3.1 Topographic data

Airborne lidar was flown in March and April 2010 by Terrapoint for the Channel Islands Lidar Collection, funded by the US Geological Survey in cooperation with The Nature Conservancy and the US National Park Service (US Geological Survey, 2010). The laser scanner was a helicopter mounted, full waveform Riegl LMS Q560 with a 1064 nm laser wavelength. The point-cloud elevation data was measured at vertical accuracy of 0.067 m with 95% confidence against stationary GPS locations. Across all the Channel Islands the average point density is 8.3 points m^{-2} but this number varies with location. Average point-density of Pozo Catchment is: 8.5 points m^{-2} for all points and 7.8 points m^{-2} for classified ground points. The return intensity among flight lines is similar with minimal visual striping. Topographic metrics for this study were calculated on the ground-classified point-cloud or a gridded product of the point-cloud (Fig. S1).

3.2 Defining geomorphic regimes

We use slope – area plots to quantify the spatial distribution of erosional regimes within Pozo (Tarboton, 1992). We used a change-point algorithm to identify the transition in Total Drainage Area (TDA) between hillslope and valley to be 12,475 m^2. The algorithm fits linear lines to the data, setting change points where the residual error associated with the fit of the linear lines is minimized. Total residual error is the sum of squared residuals for each linear fit. The algorithm can be dialed to a minimum threshold of residual error decrease required to identify a change point by increasing numbers of change points. Error bounds

created by the intersection of the interquartile range (25^{th} to 75^{th} percentile) on linear fits for each regime (Fig. S2, S3), set the transition from hillslope to valley between 5,353 m^2 and 24,492 m^2. For the remainder of this paper, we will refer to these TDA ranges as three separate geomorphic regimes: hillslope (0 – 5,353 m^2), transition (5,353 – 24,492 m^2), and valley (>24,492 m^2).

The defined breaks between geomorphic regimes are relative breaks useful for interpreting landscape metrics, but not absolute. We interpret the extensive gullying up to the ridgetop in some locations within Pozo as an example of the fluidity in the breaks determined from slope-area space. The erosion triggered by the 1878 rain events is typified by wide and shallow denuded regions at the hilltops, indicative of sheetwash processes. With increasing drainage area, erosion follows established routes of incision, or gullies (Dunne & Aubrey, 1986; Horton, 1945; Kirkby & Bracken, 2009). We argue that the pervasive presence of gullies within Pozo creates a broader transition zone between hillslope and valley segments; slope begins to decrease more rapidly at 10^3 m^2 TDA.

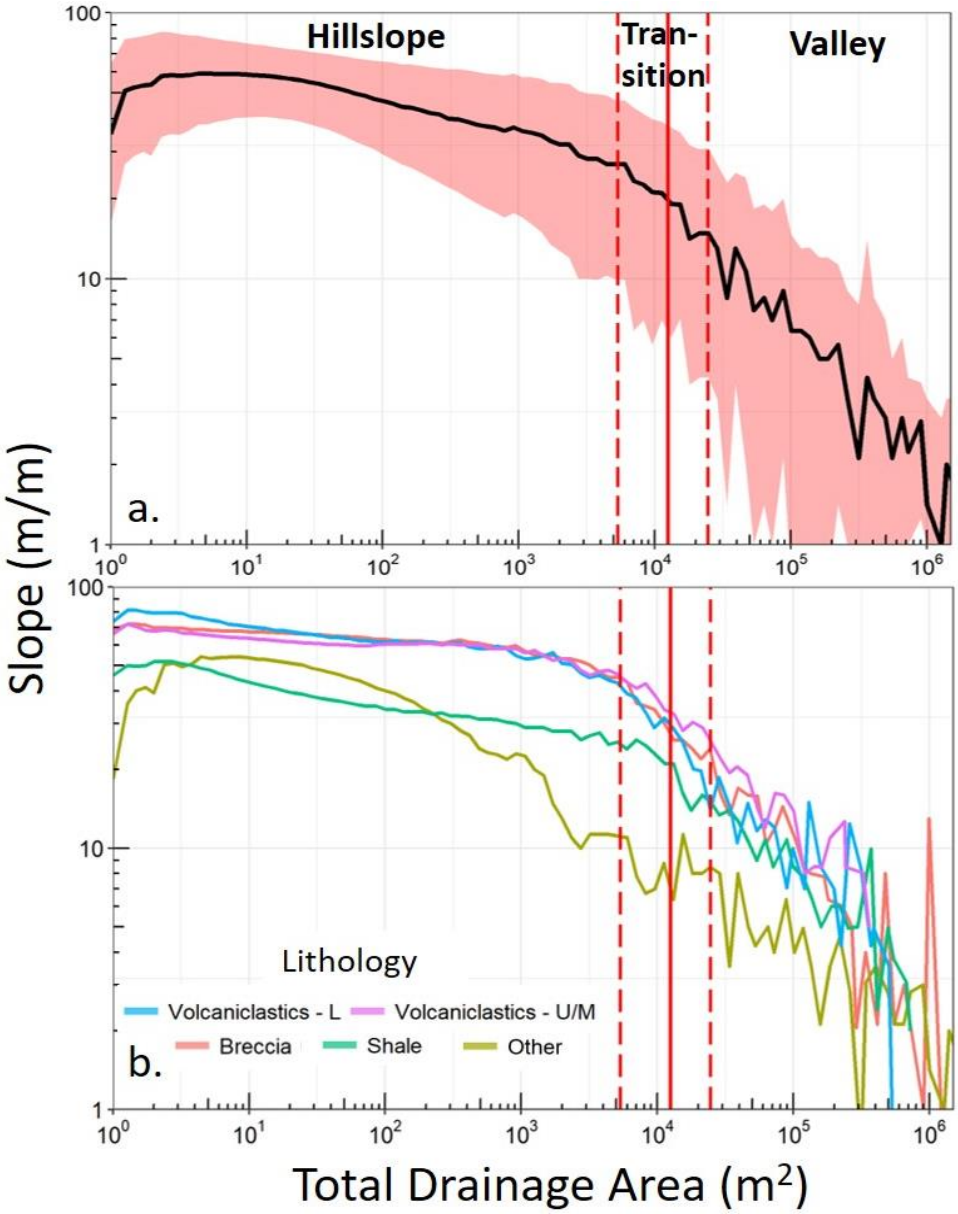

Figure 2. Total drainage area (TDA) and slope plots for the Pozo Catchment derived from a 1-m DEM (cf. Figure 1). a. median slopes for log binned total drainage area (n = 100 bins) and the interquartile range of the slopes for log binned total drainage area. The red dashed lines represent the error bounds produced by the intersection of prediction lines determined by the interquartile range around best-fit lines (cf. Fig. S3). We consider these error bounds to represent a transition zone of total drainage area between hillslope and valley geomorphic regimes. b. median slopes for log binned total drainage area (TDA) (n = 100 bins) for each lithology. "Other" lithologies include all the Quaternary fill sediments from the Pozo Catchment valley (which are associated with the highest total drainage area values and lowest slopes) and thin bands of other marine clastic lithologies including Rincon Shale, Cozy Dell Shale, Vaqueros Sandstone, and sandstones and conglomerates in the Jolla Viejo Formation.

3.3 Incision Algorithm

This work evaluates recent (<140 years) erosion by using a point cloud derived metric for surface roughness to calculate the difference between a "reconstructed surface" and the present surface by determining the inter-quartile range (IQR) of elevation within a specified search radius and assigning this range to a resolution-specified grid. We refer to the surface roughness raster as incision (-depth) [m], which can be converted to a volumetric erosion estimate by integrating the incision depths over the grid or map area [m^3]. Adding the incision-depth raster to the original DEM for the landscape creates a "reconstructed, pre-incised surface", which we refer to as reconstructed surface in the remainder of the manuscript.

3.3.1 Assumptions for reconstructing a pre-incised surface

Patchy remnants of relict soil in the field indicate that the land surface was once soil mantled and erosion over the last 140 years has removed substantial portions of it. This is supported by extensive field observations and previously published work (Perroy et al., 2010; 2012). Therefore, we use these low-roughness patches that contain few sharp slope breaks to represent non-eroded, patches of soil. Sharp slope breaks correspond to drastic changes in local elevation produced by incision. The density of the point-cloud makes these slope breaks readily detectable. We are confident that elevation differences detected by the algorithm are caused by changes in slope related to incision because the study region contains few rocks outcropping above the remnant soil patches. Due to the history of erosion in the study area

and the style of current erosion, the resultant incision-depth raster provides an estimate of soil loss similar to that achieved by use of topographic data time series.

3.3.2 Point-cloud incision algorithm mechanics

The surface roughness algorithm uses the ground-classified point-cloud to estimate erosion by calculating elevation statistics within a user-defined window size; it is publicly available and is based on an open-source python environment. Ground points were extracted from the unclassified point-cloud using LAStools (Isenburg, 2012). The algorithm uses kd-trees (Bentley, 1975) to spatially sort the point-cloud and then assign seed-point locations based on a user-defined fixed seed-point spacing (e.g. 1 m). The seed-point selection includes one lidar point m^{-2} that is closest to the cell center. For a dense point-cloud this will result in an almost equally spaced seed-point file whereas for steep, vegetated terrain, seed point spacing will likely vary due to lower point density. The algorithm also allows homogenization of the point-cloud to generate similar point densities for each seed point by randomly selecting points based on point-density neighborhoods, similar to Poisson sampling (i.e., for an area with a low number of points, most of these points are selected, an area with a high number of points result in a reduced number of points). Based on the seed-point spacing and a user-defined search radius (Fig. 3a), we fit linear or second-order polynomial planes (typically the same size as the search radius) through all ground-classified points; we refer to these areas as patches. The linear plane produces a patch surface that is ready for surface roughness calculation by removing potential confounding effects of the hillslope angle through slope normalization. By detrending the ground data only, the elevation difference assigned to incision is included in the range calculation, excluding potentially erroneous

effects on incision measurements from steep hillslope angles. Our algorithm calculates the statistical distribution of the points, such as minimum, maximum, 90^{th}-10^{th} percentile range, inter-quartile range (IQR), and calculate first- and second-order derivatives (slope and curvature) (Fig. S4). The coordinate for each seed point is then associated with a set of parameters that can be stored as a raster or regularized point-cloud. While the elevational range statistics may over compensate in areas with outcropping rock or directly adjacent to deeply incised regions, the code's variables can be manipulated to fine-tune results in order to minimize these effects (Fig. 3b).

Post-processing and analysis of incision rasters are easily implemented in standard GIS software. For this study, the incision-raster extent was aligned to match rasters of vegetation cover and total drainage area. Rasters of total drainage area and slope were produced with the D-infinity flow routing algorithm with TauDEM (Tarboton, 2002) using a 1-m bare-earth DEM created from the classified point-cloud data. For the Pozo Catchment, we ran the algorithm on segments less than 1.5 million points. This divided the catchment into 140 approximately equal pieces and recombined the results for analysis.

3.3.3 Error analysis on the incision algorithm

Incision estimates are constrained by dialing in the search radius according to the widths of recently incised features within the landscape. These features included incipient gullies at or close to ridgetops and also recent soil slips with clearly defined scarps. While features were chosen and measured via hillshade imagery, field observations confirm that these features are recent (i.e. dating to the high-intensity grazing period or later). The measured widths were taken perpendicular to flow route and from each of the three major

lithologies; shale, breccia, and volcaniclastics (Fig. S5). The range in feature width is large due to the variable nature of erosion between the underlying lithologies; however, the mean width is 6.55 ± 3.10 meters (N = 20) (Table S1). This produces a mean search radius of 3.28 m with a standard deviation range of 1.73 to 4.82 m. Incision error is estimated from the standard deviation around the mean using search radii of 1.7 and 4.8 m for selected catchments, which represent the major lithologies and a wide range of total drainage area (0-10^5 m^2) (Fig. S6, Table S2). For simplicity, this study uses a 3-m search radius for the entire Pozo Catchment incision calculation. Geomorphic regimes (Fig. 2) and the major lithologies are used to parse error estimates for total incision volumes and erosion rates for Pozo Catchment. We have verified the point-cloud accuracy with a 16 dGPS (0.01 m accuracy) collected during field work that support sub-10cm accuracy for unvegetated terrain.

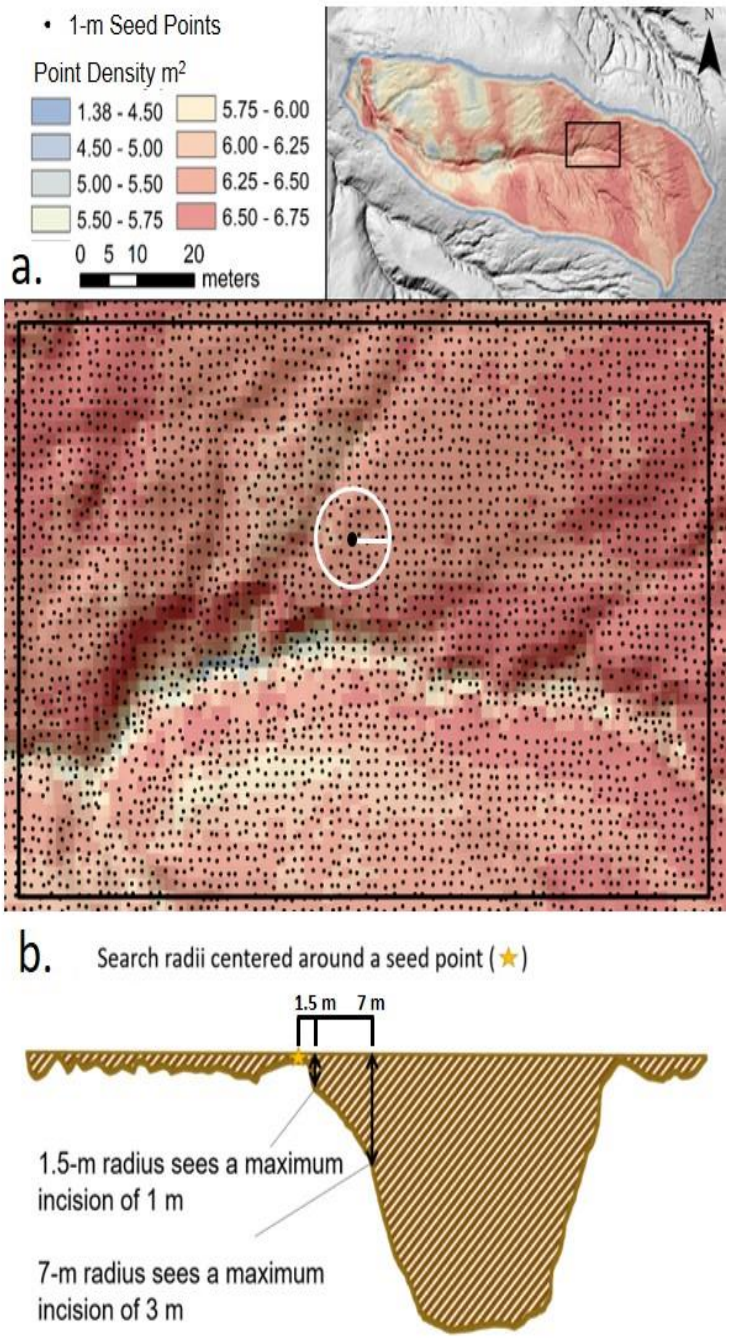

Figure 3. a. Small region of the test sub-catchment (cf. Figure 1) and outlined by black box in a-inset) showing a 1-m seed-point spacing overlaid on the number of ground-classified lidar returns (density only shows ground-classified points). Within the identified search radii (white circle, radii of 5 m), tens to hundreds of points are used in calculating statistics. Seed spacing appears irregular in a 2-D representation of the landscape, but follows true lidar points (closest point to the center has been chosen). b. Cartoon showing the maximum incision that would be assigned to a seed point depending on the search radius.

3.4 Vegetation presence detection via lidar-return intensity

3.4.1 Why use lidar return intensity to identify vegetation presence?

It is difficult to establish whether present-day spatial patterning of vegetation is a cause or effect in erosion studies. For the most part, studies show that the presence of vegetation dampens erosion (Bastola et al., 2018; Istanbullouglu & Bras, 2005; Vanacker et al., 2007; Olen et al., 2017). As noted previously, present-day vegetation patterns on SCI vary considerably depending on lithology, implying a heterogeneous effect of stabilization by vegetation. Pre-existing vegetation mapping for the Pozo Catchment is limited to depiction of species distribution and approximate density at the half-hectare scale, which is not adequate to assess the influence of vegetation (Cohen et al., 2009). Lidar processing algorithms often include a classification scheme for vegetation which would provide a higher resolution map of vegetation presence, however these algorithms tend to be based on beam return counts, 3-D structural pattern, or heights above last returns which can exclude grass-covered areas due to minimal differencing in height of grass returns and ground returns.

We used the lidar return intensity data (hereafter referred to as intensity data) to identify presence of vegetation at the 1-m^2 scale using a simplified supervised classification. Lidar return intensity is the ratio of beam return strengths to the strength of the emitted beam. The major factor affecting intensity is the reflectance of the objects the beam intercepts at the wavelength of the beam, 1064 nm (Yan et al., 2015); in this case, exposed rock and dry soil tends to reflect more than growing vegetation, making vegetated areas return lower intensities than non-vegetated. We tuned the identification of vegetation by selecting a vegetation threshold of return intensity for the region and optimized the analysis to ensure

inclusion of grass (in addition to tree and shrub) covered landscapes. More information on the raw lidar point-cloud can be found in the Supporting Information (S7).

3.4.2 Classifying non-vegetated and vegetated areas using a binary threshold on control polygons

Lidar intensity data were gridded at 1-m^2 resolution, assigning each pixel the average intensity value of all returns: this limits the intensity value range to between 16 and 1518. For the improved point-cloud classification, non-vegetated and vegetated control polygons were hand delineated in catchments underlain by the three major lithologies of Pozo to calibrate the binary threshold for the entire catchment (Fig. S8). The threshold was chosen by calculating the percentages of correctly detected vegetation and miscounted non-vegetated for intensity values between 50 and 250, at intervals of 25. The binary threshold is the whole number midpoint between the two intensity values (ie. 137 for 125 and 150) where the percent of miscounted non-vegetated pixels start to drastically increase (Fig. 4). We consider the range between 125 and 150 to be the intensity threshold zone where the percent correctly identified vegetation could be maximized while still minimizing erroneous detection (non-vegetated areas counted at vegetated regions). We used this range as error bounds for our binary threshold value. Uncalibrated return intensity data are specific to the data collection flights and therefore our calculated unitless threshold is unique to this dataset; however, the

method is applicable to any dataset. We use this vegetation cover index to evaluate the incision patterns produced directly from the point-cloud.

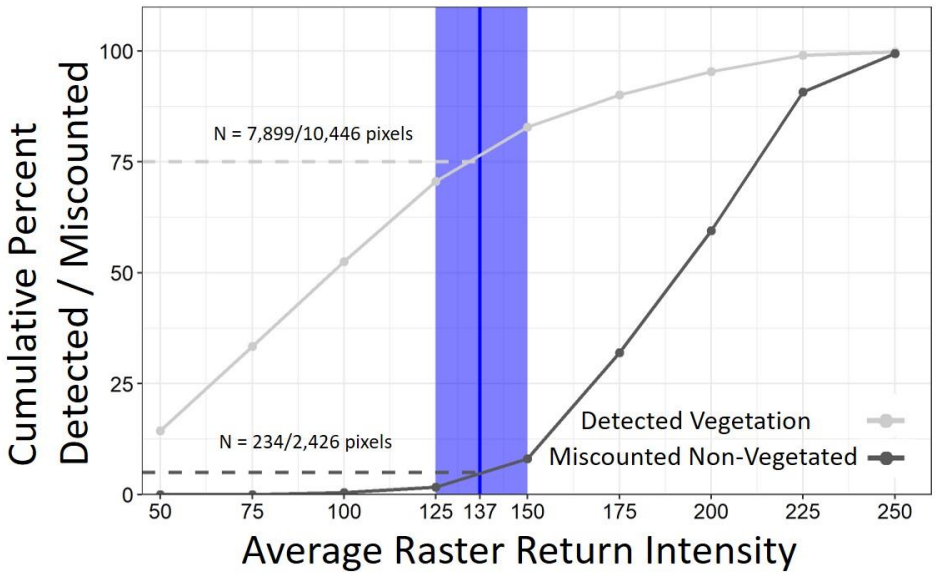

Figure 4. Binary threshold determination for vegetation vs. non-vegetated classes using average intensity of lidar returns gridded to 1 m. The blue dashed line marks the return intensity threshold of 137 – above this value pixels were considered non-vegetated, below this value pixels were considered vegetated. For the threshold of 137, 3% of non-vegetated pixels are miscounted as vegetation (N = 71 of 2462 pixels, dark grey line) and 77% of vegetated pixels (N = 8108 of 10514 pixels, light grey line) are correctly identified. The shaded blue area indicates error bounds on the return intensity threshold, which brackets the range in which miscounted non-vegetation begins to significantly increase (125 – 150).

4 Results

4.1 Incision algorithm search radius effect on erosion measurements

Figure 5 shows incision depth as a function of discharge area evaluated for different search radii. Increasing the search-radius size results in an increase in the overall magnitude of incision and in the sensitivity of incision to transitions between geomorphic regimes. Incision depths within the test sub-catchment start to increase before the slope-area determined transition zone (cf. Fig. 2, location at 12,475 m and between a range of 5,353 and

24,492 m^2 Incision begins to increase once a total drainage area (TDA) of 1,000 m^2 is reached and continues to increase through the transition zone (highlighted in red, Fig. 5). The incision changes with TDA are relatively muted for search radii of 3 m or smaller. At these smaller search radii, valley incision (SCA > 24,492 m^2) is two to three times higher (<= 1 m) than for the hillslope and transitional regimes. Expanding the search radii to >10 m produces incision estimates that are at least five times greater at the maximum drainage area range.

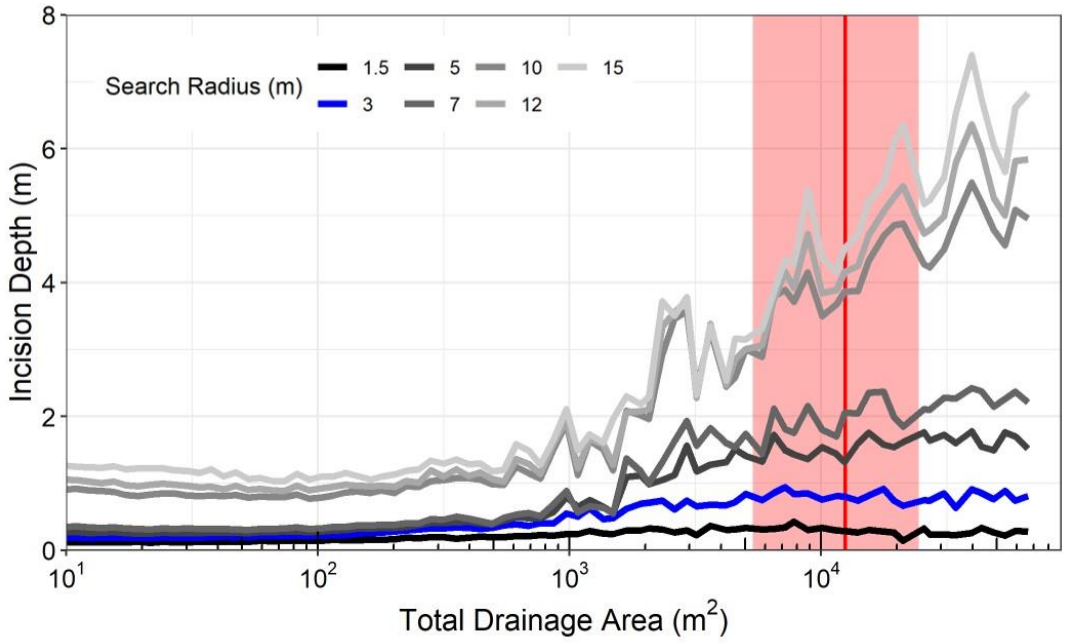

Figure 5. Search radii effects on incision-depth medians for log-binned (n = 100 bins) total drainage areas for our test sub-catchment (cf. Figure 1). Red-highlighted TDA zone is the transition zone between hillslope and valley regimes based on slope-total drainage area trends from Fig. 2. Radii used are 1.5 m, 3 m, 5 m, 7 m, 10 m, 12 m, and 15 m for a seed point spacing of 1 m. The 3-m radius is highlighted in blue as this is the search radius used for the whole Pozo catchment analysis. Interpretation of incision-depth patterns at very low drainage areas may be faulty, therefore these plots are cropped at 10^1 m^2 TDA.

4.2 Spatial patterns of incision and vegetation for Pozo

Incision depth estimated by the interquartile range of elevation within a 3-m moving window across the Pozo Catchment shows different spatial patterns (Fig. 6) and also statistical distributions for each lithology (see Supporting Information for more on the statistical testing, Fig. S9 & S10). For the Cañada Shale, interfluves have low (0-10 cm) incision that flank,areas of very deep incision (20 – 500 cm). By contrast, incision patterns in the upper and middle members of the Blanca Volcaniclastics show shallower and less wide spread incision. The breccia has more incision within the interfluves than the shale, but a less extensive incision network downslope. The lower member of the Blanca Volcanics has deeper incision than most other areas in the catchment but represents a very small portion of total catchment area. “Other” lithologies show similar incision patterns as the shale on the hillslopes. The “other” category also encompasses valley-fill sediments; the valley areas only show a small amount of incision along the active channel edge where down-cutting has occurred.

Figure 7 compares spatial incision depth data with the presence of vegetation across geomorphic regimes to test the relationship between vegetation and soil loss. Across all lithologies (Fig. 7a), incision differences in non-vegetated and vegetated areas are greatest between 500 and 25,000 m^2 TDA; this range encompasses the transition zone between hillslope and valley geomorphic regimes (cf. Fig. 2). Within this range, incision is higher in the non-vegetated areas than the vegetated areas. Vegetated areas below 500 m^2 show slightly

higher incision than non-vegetated areas, while vegetated areas above 25,000 m^2 show similar incision depths to non-vegetated regions.

Comparing incision depth to total drainage area between the two lithologies (Fig. 7b) that are most spatially prevalent and have contrasting incision distributions (Fig. S9 & S10), shows differing incision patterns between non-vegetated and vegetated areas. Incision is higher in non-vegetated and vegetated areas for both lithologies before the transition to the valley regime. Between 1 and 1,000 m^2 TDA the differences between vegetated and unvegetated and the two lithologies are small; however, the shale shows higher incision in unvegetated areas. In contrast, the vegetated areas of the volcaniclastics show the opposite pattern – higher incision in vegetated areas. For the shale, as drainage area increases towards the transition zone (1,000 to 5,353 m^2), incision increases with the deepest incision occurring in unvegetated regions. Within this same drainage area, the volcaniclastics have shallower incision than the shale (35-65 cm total for the volcaniclastics compared with 65-95 cm total for the shale) and in contrast to the shale incision is similar between vegetated and unvegetated areas. Above 24,492 m^2 total drainage area, incision in the vegetated areas of the volcaniclastics stabilize at around 65-70 cm, whereas incision in the non-vegetated regions have generally higher incision values of 75-85 cm. shale incision is fairly similar for the vegetated and non-vegetated areas in the concave valley regime, with incision decreasing from about 95 cm to 55 cm with large fluctuations between those values. The volcaniclastics

have higher median incision in vegetated areas than non-vegetated, this is in contrast with the shale.

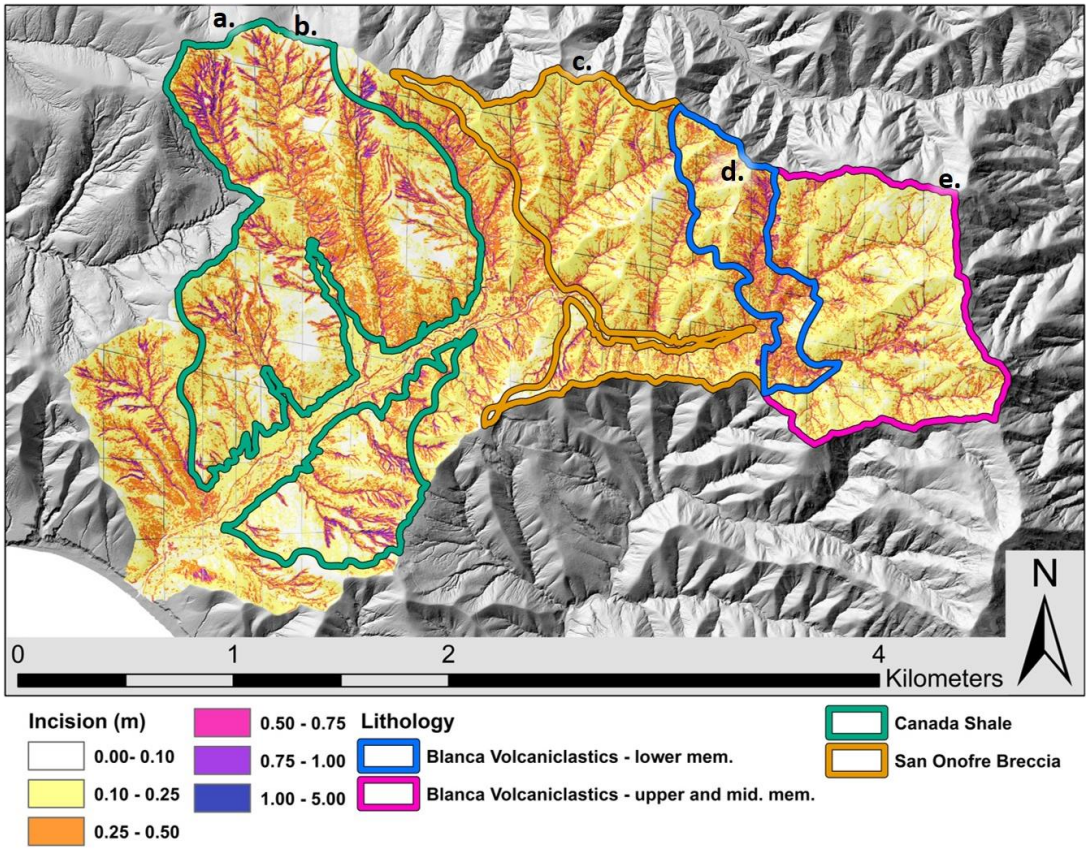

Figure 6. Incision depth for the Pozo Catchment calculated using a 3-m search radius and rasterized to a 1-m resolution. Major lithologies used for analysis are outlined. The "Other" lithology category (cf. Figure 1) is not outlined but represents the rest of the catchment not identified with an outlined lithology. The letters represent approximate locations of field pictures shown in Figure 8.

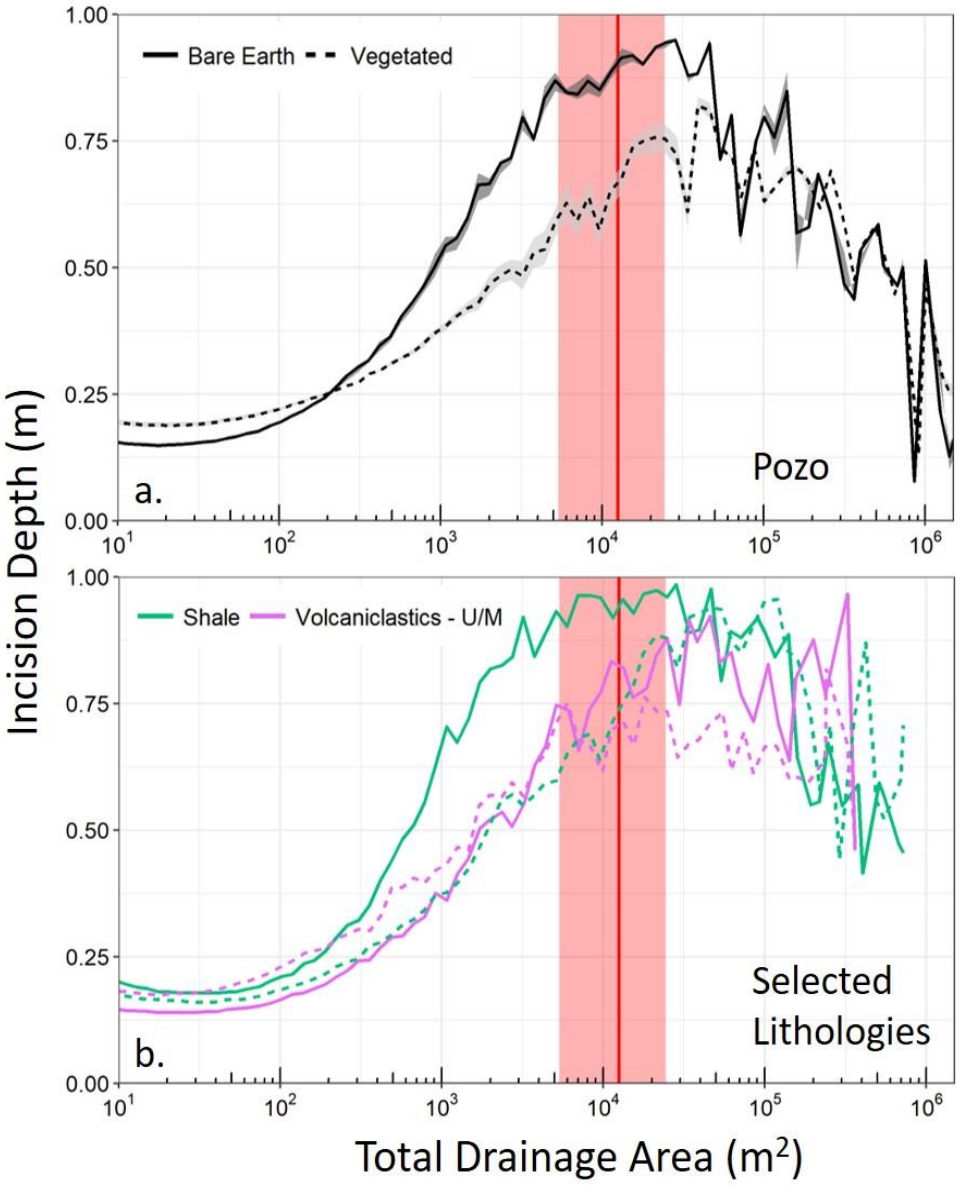

Figure 7. The influence of vegetation on incision depth across geomorphic regions a. Pozo-wide median incision depth for binned values of TDA (n= 1000 bins) and parsed by vegetated and non-vegetated areas produced by the lidar-intensity identified vegetation map (cf. Figs. 4-6). Shaded areas indicate error range in the intensity threshold between 125 and 150 for parsing vegetated and non-vegetated areas. b. Shale and volcaniclastic incision depth changes with increasing TDA parsed by vegetated and non-vegetated areas regions. Transition zone between hillslope and valley geomorphic regimes based on slope-total drainage area trends (cf. Fig. 2) is marked by the red shaded area on both plots. Interpretation of incision-depth patterns at very low drainage areas may be faulty, therefore these plots are cropped at $10^{\wedge 1}$ m^2 TDA.

Table 1. Vegetation influence on incision for two contrasting lithologies.

Lithology	Vegetation cover	Area (m^2)	Mean incision depth (m)	Median incision depth (m)	75th Perc. incision depth (m)	25th Perc. incision depth (m)	Total incision (m^3)
Shale	Non-Vegetated	653,158	0.34	0.25	0.43	0.15	218,961
Shale	Vegetated	1,508,779	0.24	0.20	0.30	0.12	365,198
Volcaniclastics - U/M	Non-Vegetated	615,028	0.19	0.15	0.22	0.11	118,164
Volcaniclastics - U/M	Vegetated	322,629	0.25	0.20	0.30	0.14	82,227

5 Discussion

5.1 Incision patterns with lithology and vegetation

Incision-depth distributions vary significantly across lithologies (Fig. 6). Furthermore, incision depth associated with vegetation cover varied depending on TDA and showed differing patterns between lithologies (Fig. 7, Table 1). All across Pozo, vegetated regions dampen the increases in incision depth with total drainage area between ~500 and 25,000 m^2, implying a negative feedback between vegetation cover and erosion. Adding to this point, the presence and type of vegetation can affect the propagation of erosion; deep-rooted trees and shrubs hold soil more strongly to hillslopes compared to shallow rooted grasses and forbs that can rapidly cover recently disturbed landscapes, but don't invest in deeper root structure (Collins et al., 2004). Incision-depth differences between the Cañada Shale and the upper/middle member of the Blanca Volcaniclastics within the hillslope - valley transition zone can be explained by the presence of deeper rooting plants in the

volcaniclastics (Bishop Pines, *Pinus muricata*, and established chaparral such as scrub oaks, *Quercus spp.* Cohen et al., 2009) and may indicate less on-going erosion in the volcaniclastics than in the shale (Collins et al., 2004). Incision within the volcaniclastics does increase downstream within the valley regime ($>10^4$ m^2), but the increase is less than in the shale. Increased vegetation presence in the downstream volcaniclastic channels is perhaps a signal of a recovering environment, where active erosion is less than in the gullies in the shale. Another possibility is that vegetation within the volcanoclastic channels plays a more active role by stabilizing the sediments around it and dampening on-going incision compared to the shale, similar to its role within transition and hillslope regions (Fig. 7b). Most likely, the presence of deep-rooted vegetation in the channels is both a signal and driver of dampened incision within the volcaniclastics.

Interestingly, the vegetated hillslope regime within the volcaniclastics has more incision than the non-vegetated areas of similar total drainage area (Fig. 7b). Greater vegetation coverage on the volcanoclastic hillslopes matches the pattern observed for most of Pozo (Fig. 7a), but differs from the pattern for shale. Field reconnaissance (Fig. 8) found minimal soil coverage on volcanoclastic hillslopes Where present, patchy soil deposits (<20 cm) backed-up behind outcropping rock or plant roots similar to the sediment storage style described in Lamb et al. (2001). Therefore, elevation differences produced by soils trapped by vegetation results in higher incision measured in the vegetated areas than in the non-vegetated regions within the volcaniclastics.

In contrast, the bulk of incision within the Cañada Shale occurs in poorly vegetated areas as rills, incipient gullies, and established gullies, which cut into convex but relatively

low slope hillslopes (Fig. 7b). The Cañada Shale, like other Miocene mudstones in California, is mechanically weak and prone to disaggregation when exposed to wetting and drying at Earth's surface (Montgomery, 2004; Johnson & Finnegan, 2015; Johnstone et al., 2017). Furthermore, the existing vegetation on the hillslopes is commonly shallow rooted annual grasses and fennel (Cohen et al., 2009), suggestive of continuing erosion within this lithology (Collins et al., 2004). Regardless of vegetation cover, much less sediment is eroded from the Blanca Volcaniclastics than the Cañada Shale (Table 1), which is likely due to the deep incision into bedrock in the Cañada Shale but minimal rock incision in the Blanca Volcaniclastics. The widespread shallow incision within the more resistant volcaniclastics represents stripping of thin surface soils while in the shale hillslopes deeper gully incision into weaker bedrock dominates the erosion signal.

Figure 8. Erosion examples and vegetation cover associated with the different lithologies. The lettering corresponds to locations on Figure 6 and indicate where the pictures were taken. a. and b. show in-tact dark organic soils and deep gullies extending into the bedrock in the Canada Shale respectively, c. shows shallow landslips near and at the ridgetop positions

within the San Onofre Breccia, d. and e. show wide swaths of shallow soil loss but minimal recent bedrock erosion in the Blanca Volcaniclastics. Vegetation type in the volcaniclastics is largely chaparral and some Bishop Pine stands in contrast to the invasive European annual grasses and fennel dominant in the shale (a. & b.).

5.2 Erosion estimate considerations

This study quantified incision over the last 140 years. Longer timescale incision, specifically within the valley regime, is difficult to separate from recent erosion because historic topographic data are limited for Pozo, as is commonly the case with historic anthropogenic erosion (Perroy et al., 2012). Our results showed incision depth increases with increasing total drainage area. The increase in incision depth is most dramatic near the top of the hillslope-valley transition (Fig. 7). We interpret deeper incision above the transition as erosion produced within the last 140 years: gullying and land slips on hillslopes ($< 5{,}353$ m^2). The sensitivity of increased incision depth within the transition is controlled by the size of the search radius (Fig. 5). Because recent erosional channel features in Pozo have an average width of 6.55 m (Table S1), increasing the radii above 3 m likely will include incision associated with pre-existing fluvially carved features. Therefore, to prevent significant over-estimation within the valley regime incision, this study uses a search radius close to half the mean of the measured widths (3 m). We have calculated error bounds on our incision estimates using search radii for the standard deviation in widths. Using our high-end estimate, underestimation of incision starts where gullies were wider than 9.65 m.

Lastly, the patterns of erosion explored here in each lithology express consistently above upper knickpoints (cf. Fig. 1b, Neely et al., 2017), where sub-catchments in each lithology are protected from any recent base level fluctuations in the mainstem below so that

we can assume lithologic control on the landscape response to anthropogenic hillslope perturbations is the primary influence on differences in erosion patterns. Furthermore, we purposely tuned our model to be less sensitive to channel incision because of the unknowns in parsing anthropogenically-influenced channel incision from longer timescale channel incision. Therefore, we feel confident that we are capturing primarily anthropogenically-influenced incision within Pozo as the geomorphic regimes with the most error (transition and valley) make up <1% of the total land area (Table 2).

5.3 Anthropogenic erosion comparisons

We estimate sediment loss since the late 1800's to be 1.60 million m^3 [range: 1.05 – 2.41 million m^3]. As an average erosion rate since 1878 (140 years) this translates to 1.84 mm yr^{-1} [range: 1.20 – 2.75 mm yr^{-1}], which is an order of magnitude larger than the background erosion rates for the island derived from cosmogenic nuclide inventories (Perroy et al., 2012) and is similar to erosion rates caused by deforestation and land conversion to agriculture in places such as the southeastern United States during the same time frame (Reusser et al., 2015). The average incision-depth estimate for Pozo is 0.26 m [range: 0.17 – 0.39 m] compares well to previous work by Perroy et al. (2010, 2012) who determined average incision depth of 0.29 ± 0.03 m. Results from Perroy et al. (2010; 2012) were determined by manually clipping gully traces within a DEM and interpolating pre-existing topography within a single sub-catchment of Pozo and scaling up the findings to the entire Pozo catchment area. Compared to previous work in the same location, the size of error bounds have increased, because we included uncertainty in the relative width of recent incision features. The strength of our approach is that it enables automation over the whole

region of interest and uses a much finer spatial resolution at the point-cloud level for estimating incision, therefore incorporating much more complexity while also providing explicit spatial resolution not yet demonstrated in incision estimates (cf. Fig. 6).

Table 2. Incision estimates with error approximations. The bulk of the incision is occurring in the hillslope geomorphic region. The shale is the lithology with the most total incision (area-average = 1.93 mm yr^{-1} compared to 1.79 and 1.70 mm yr^{-1} for the breccia and volcaniclastics), the shale is the lithology that is most subject to intense gullying. Average, high, and low bounds on incision estimates were produced from percent change between incision rasters of different search radius for selected sub-catchments in Pozo (Table S1, S2). The search radii used were the mean and mean ± standard deviation of width for erosional features know to be recent (N=20, informed by fieldwork).

Geomorphic Position and TDA	Lithology	Mean Incision Depth (m)	Mean Incision Depth - High Est. (m)	Mean Incision Depth - Low Est. (m)	Total Incision (m^3)	Total Incision - High Est. (m^3)	Total Incision - Low Est. (m^3)	Fraction of Total Catchment Area
Hillslope, 5,353 m^2	Shale	**0.27**	0.43	0.15	**571,017**	932,259	322,799	0.3439
Hillslope, 5,353 m^2	Breccia	**0.25**	0.36	0.17	**281,296**	411,166	197,607	0.1822
Hillslope, 5,353 m^2	Volcaniclastics	**0.23**	0.35	0.17	**300,069**	442,163	212,900	0.2053
Hillslope, 5,353 m^2	Other	**0.26**	0.35	0.18	**414,913**	566,649	298,584	0.2599
Transition, 5,353 – 24,492 m^2	Shale	**0.85**	1.30	0.45	**7,244**	11,075	3,787	0.0014
Transition, 5,353 – 24,492 m^2	Breccia	**0.88**	1.30	0.42	**3,259**	4,788	1,543	0.0006
Transition, 5,353 – 24,492 m^2	Volcaniclastics	**0.78**	1.16	0.40	**3,524**	5,261	1,804	0.0007
Transition, 5,353 – 24,492 m^2	Other	**0.52**	0.76	0.43	**4,646**	6,807	3,881	0.0014
Valley, 24,492 m^2	Shale	**0.85**	1.26	0.48	**5,897**	8,791	3,350	0.0011
Valley, 24,492 m^2	Breccia	**0.76**	1.18	0.35	**2,650**	4,118	1,212	0.0006

Valley, 24,492 m^2	Volcaniclastics	**0.70**	1.16	0.34	**3,238**	5,350	1,558	0.0007
Valley, 24,492 m^2	Other	**0.46**	0.65	0.29	**6,376**	9,027	4,033	0.0022
Totals	All	**0.26**	**0.39**	**0.17**	**1,604,129**	**2,407,453**	**1,053,058**	**1.0000**

6 Conclusions

This study uses lidar point-cloud data in conjunction with field observations to quantify erosion starting from a known-age (140 years ago) anthropogenic disturbance in a lithologically diverse landscape without time-series topographic data coverage. We calculated spatially resolved incision depths using a surface roughness algorithm on a lidar point-cloud. The point-cloud incision algorithm can be dialed to the scale of erosion features by changing the search radius: we use a 3-m search radius to prevent detection of long-term, watershed-scale fluvially carved topography, which can occur at higher search radii. Error bounds for the 3-m incision-depth map are based on field-informed width measurements of recent erosional features. We also calculated a high resolution vegetation cover map using a binary threshold in lidar return intensity. Error bounds for the vegetation map are set by the range where miss-identified non-vegetated areas are minimized. We compared our incision and vegetation maps across total drainage area and between different underlying lithologies.

Vegetation cover dampens incision across a range in total drainage areas for Pozo implying an overall negative feedback between incision and vegetation cover. However, the underlying lithology can set vegetation type differences that complicate this pattern, as evidenced by comparison between shale and volcaniclastics. Areas underlain by friable

Cañada Shale have less vegetation in incised areas and more in interfluve areas compared to the Blanca Volcaniclastics that have lost more soil and vegetation from interfluve areas and where vegetation is concentrated in concave positions further down slope. This pattern is likely due to the relative strength of the bedrock. Within the volcaniclastics there is minimal new mobile sediment to remove from the landscape compared to the shale bedrock, which readily erodes constantly supplying sediment. The spatially averaged erosion estimates from this study match and extend previous work indicating an order of magnitude increase over background rates. Increasing intensity and frequency of landscape perturbations from human influence drives a need for more precise soil loss estimates, which we demonstrate can be derived from single time-point lidar point-cloud data.

Acknowledgments

Topographic data used in this work was obtained from OpenTopography, DOI: 10.5069/G95D8PS7. Funding for this project was in-part by NSF-EAR Grant No. 1411309. The current Python source code and extensive manual are available at: https://github.com/BodoBookhagen/PC_geomorph_roughness.

References

Anderson, S. W., Anderson, S. P., & Anderson, R. S. (2015). Exhumation by debris flows in the 2013 Colorado Front Range storm. Geology, 43(5), 391-394. https://doi.org/10.1130/G36507.1

Baguskas, S. A., Peterson, S. H., Bookhagen, B., & Still, C. J. (2014). Evaluating spatial patterns of drought-induced tree mortality in a coastal California pine forest. Forest Ecology and Management, 315, 43-53. https://doi.org/10.1016/j.foreco.2013.12.020

Bastola, S., Dialynas, Y.G., Bras, R.L., Noto, L.V., & Istanbulluoglu, E. (2018). The role of vegetation on gully erosion stabilization at a severely degraded landscape: A case study from Calhoun Experimental Critical Zone Observatory. Geomorphology, 308, 25-39. https://doi.org/10.1016/j.geomorph.2017.12.032

Bentley, J. L. (1975). Multidimensional binary search trees used for associative searching. Communications of the ACM, 18(9), 509. https://doi:10.1145/361002.361007

Bettis III, E. A., & Thompson, D. M. (1985). Gully erosion. Rangelands, 7(2), 70–72.

Bookhagen, B. (2018). Point Cloud (PC) Geomorphologic roughness and topographic detrending (Github repository). https://github.com/BodoBookhagen/PC_geomorph_roughness

Brasington, J., Vericat, D., & Rychkov, I. (2012). Modeling river bed morphology, roughness, and surface sedimentology using high resolution terrestrial laser scanning. Water Resources Research, 48(11), 1–18. https://doi.org/10.1029/2012WR012223

Breslow, N. (1970). A generalized Kruskal-Wallis test for comparing K samples subject to unequal patterns of censorship. Biometrika, 57(3), 579-594. https://doi.org/10.1093/biomet/57.3.579

Bryan, K. (1925). Date of channel trenching (arroyo cutting) in the arid southwest. Science, 62(1607), 338-344. DOI: 10.1126/science.62.1607.338

Bull, L. J., & Kirkby, M. J. (1997). Gully Processes and Modelling. Progress in Physical Geography, 21(3), 354–374. https://doi.org/10.1177/030913339702100302

Cohen, B., Cory, C., Menke, J., & Hepburn, A. (2009). A spatial database of Santa Cruz Island vegetation. In Proceedings of the 7th California Islands Symposium. Institute for Wildlife Studies, Arcata, CA (pp. 229-244). Retrieved from https://map.dfg.ca.gov/metadata/ds0563.html

Collins, D. B. G. (2004). Modeling the effects of vegetation-erosion coupling on landscape evolution. Journal of Geophysical Research, 109(F3), F03004. https://doi.org/10.1029/2003JF000028

Cooke, R., & Reeves, R. (1977). Arroyos and Environmental Change in the American Southwest. Earth-Science Reviews, 13(2), 211–212. https://doi.org/10.1016/0012-8252(77)90042-3

Dibblee, T. W. (2001a). Geologic Map of western Santa Cruz Island, Santa Barbara County, California (Map No. DF-77). Santa Barbara, CA: Dibblee Geological Foundation.

Dibblee, T. W. (2001b). Geologic Map of eastern Santa Cruz Island, Santa Barbara County, California (Map No. DF-78). Santa Barbara, CA: Dibblee Geological Foundation.

Donnellan, A., Parker, J., Milliner, C., Farr, T. G., Glasscoe, M., Lou, Y., ... & Hawkins, B. (2018). UAVSAR and Optical Analysis of the Thomas Fire Scar and Montecito Debris Flows: Case Study of Methods for Disaster Response using Remote Sensing Products. Earth and Space Science. https://doi.org/10.1029/2018EA000398

Dunne, T. & Aubrey, B.F. (1986). Evaluation of Horton's theory of sheetwash and rill erosion on the basis of field experiments. In Abrahams, A. (Eds.), Hillslope Processes (Chap. 2, pp. 31-53). Boston, MA: Allen & Unwin.

Fernandez, J. C., Singhania, A., Caceres, J., Slatton, K. C., Starek, M., & Kumar, R. (2007). An overview of lidar point cloud processing software. GEM Center Report No. Rep_2007-12-001, University of Florida.

Hereford, R. (1993). Entrenchment and widening of the Upper San Pedro River, Arizona (Special Paper 282, pp. 1-47). https://doi.org/https://doi.org/10.1130/SPE282-p1

Hooke, R. L. (2000). On the history of human as geomorphic agent. Geology, 28(9), 843–846. https://doi.org/10.1130/0091-7613(2000)28<843

Horton, R. E. (1945). Erosional development of streams and their drainage basins; Hydrophysical approach to quantitative morphology. Geological Society Of America Bulletin, 56, 275–370. https://doi.org/10.1130/0016-7606(1945)56

Isenburg, M., (2012). Lastools: Converting, Filtering, Viewing, Gridding, and Compressing Lidar Data. http://www.cs.unc.edu/~isenburg/lastools

Johnson, K. N., & Finnegan, N. J. (2015). A lithologic control on active meandering in bedrock channels. GSA Bulletin, 127 (11-12), 1766–1776. https://doi.org/10.1130/B31184.1

Johnstone, S. A., Chadwick, K. D., Frias, M., Tagliaro, G., & Hilley, G. E. (2017). Soil development over mud-rich rocks produces landscape-scale erosional instabilities in the northern Gabilan Mesa, California. Bulletin of the Geological Society of America, 129(9–10), 1266–1279. https://doi.org/10.1130/B31546.1

Jones, J. A., & Grice, D. (1993). A computer-generated soils map of Santa Cruz Island, California. In Hochberg, F.G. (Eds.), Third California Islands Symposium (pp. 45-56). Santa Barbara, CA: Santa Barbara Museum of Natural History

Kirkby, M. J., & Bracken, L. J. (2009). Gully processes and gully dynamics. Earth Surface Processes and Landforms, 34, 1841–1851. https://doi.org/10.1002/esp.1866

Lamb, M. P., Scheingross, J. S., Amidon, W. H., Swanson, E., & Limaye, A. (2011). A model for fireinduced sediment yield by dry ravel in steep landscapes. Journal of Geophysical Research: Earth Surface, 116(F3). https://doi.org/10.1029/2010JF001878

Signal Processing Toolbox: findchangepts [Matlab R2018a]. (2018). Retrieved from https://www.mathworks.com/help/signal/ref/findchangepts.html

Montgomery, David R. "Observations on the role of lithology in strath terrace formation and bedrock channel width." American Journal of Science 304.5 (2004): 454-476.

Montgomery, D. R. (2007). Soil erosion and agricultural sustainability. Proceedings of the National Academy of Sciences of the United States of America, 104(33), 13268–13272. https://doi.org/10.1073/pnas.0611508104

Muhs, D. R., Simmons, K. R., Schumann, R. R., Groves, L. T., DeVogel, S. B., Minor, S. A., & Laurel, D. (2014). Coastal tectonics on the eastern margin of the Pacific Rim: Late Quaternary sea-level history and uplift rates, Channel Islands National Park, California, USA. Quaternary Science Reviews, 105, 209–238. https://doi.org/10.1016/j.quascirev.2014.09.017

Muhs, D. R., Simmons, K. R., Schumann, R. R., Groves, L. T., Mitrovica, J. X., & Laurel, D. (2012). Sea-level history during the Last Interglacial complex on San Nicolas Island, California: Implications for glacial isostatic adjustment processes, paleozoogeography and tectonics. Quaternary Science Reviews, 37, 1–25. https://doi.org/10.1016/j.quascirev.2012.01.010

Neely, A. B., Bookhagen, B., & Burbank, D. W. (2017). An automated knickzone selection algorithm (KZ-Picker) to analyze transient landscapes: Calibration and validation. Journal of Geophysical Research: Earth Surface, 122(6), 1236–1261. https://doi.org/10.1002/2017JF004250

Olen, S. M., Bookhagen, B., & Strecker, M. R. (2016). Role of climate and vegetation density in modulating denudation rates in the Himalaya. Earth and Planetary Science Letters, 445, 57-67. http://dx.doi.org/10.1016/j.epsl.2016.03.047

Parkes, J. P., Ramsey, D. S., Macdonald, N., Walker, K., McKnight, S., Cohen, B. S., & Morrison, S. A. (2010). Rapid eradication of feral pigs (Sus scrofa) from Santa Cruz Island, California. Biological Conservation, 143(3), 634-641. https://doi.org/10.1016/j.biocon.2009.11.028

Passalacqua, P., Belmont, P., Staley, D. M., Simley, J. D., Arrowsmith, J. R., Bode, C. A., Crosby, C., DeLong, S. B., Glenn, N. F., Kelly, A., Lague, D., Sangireddy, H., Schaffrath, K., Tarboton, D. G., Wasklewicz, T., & Wheaton, J. M. (2015). Analyzing high resolution topography for advancing the understanding of mass and energy transfer through landscapes: A review. Earth-Science Reviews, 148, 174-193. https://doi.org/10.1016/j.earscirev.2015.05.012

Perroy, R. L., Bookhagen, B., Asner, G. P., & Chadwick, O. A. (2010). Comparison of gully erosion estimates using airborne and ground-based LiDAR on Santa Cruz Island, California. Geomorphology, 118(3–4), 288–300. https://doi.org/10.1016/j.geomorph.2010.01.009

Perroy, R. L., Bookhagen, B., Chadwick, O. A., & Howarth, J. T. (2012). Holocene and Anthropocene Landscape Change: Arroyo Formation on Santa Cruz Island, California. Annals of the Association of American Geographers, 102(6), 1229–1250. https://doi.org/10.1080/00045608.2012.715054

Pinter, N., Lueddecke, S. B., Keller, E. A., & Simmons, K. R. (1998). Late Quaternary slip on the Santa Cruz Island fault, California. Bulletin of the Geological Society of America, 110(6), 711–722. https://doi.org/10.1130/0016-7606(1998)110<0711:LQSOTS>2.3.CO;2

Pinter, N., & Vestal, W. D. (2005). El Nino-driven landsliding and postgrazing vegetative recovery, Santa Cruz Island, California. Journal of Geophysical Research: Earth Surface, 110(2), 1–17. https://doi.org/10.1029/2004JF000203

Purinton, B., & Bookhagen, B. (2018). Measuring decadal vertical land-level changes from SRTM-C (2000) and TanDEM-X (~ 2015) in the south-central Andes. Earth Surface Dynamics, 6(4). https://doi.org/10.5194/esurf-6-971-2018, 2018

Roering, J. J., Perron, J. T., & Kirchner, J. W. (2007). Functional relationships between denudation and hillslope form and relief. Earth and Planetary Science Letters, 264(1-2), 245-258. https://doi.org/10.1016/j.epsl.2007.09.035

Rengers, F. K., & Tucker, G. E. (2015). The evolution of gully headcut morphology: a case study using terrestrial laser scanning and hydrological monitoring. Earth Surface Processes and Landforms, 40(10), 1304-1317. DOI: 10.1002/esp.3721

Reusser, L., Bierman, P., & Rood, D. (2015). Quantifying human impacts on rates of erosion and sediment transport at a landscape scale. Geology, 43(2), 171–174. https://doi.org/10.1130/G36272.1

Reutebuch, S. E., Andersen, H. E., & McGaughey, R. J. (2005). Light detection and ranging (LIDAR): an emerging tool for multiple resource inventory. Journal of Forestry, 103(6), 286-292. https://doi.org/10.1093/jof/103.6.286

Rychkov, I., Brasington, J., & Vericat, D. (2012). Computational and methodological aspects of terrestrial surface analysis based on point clouds. Computers and Geosciences, 42, 64–70. https://doi.org/10.1016/j.cageo.2012.02.011

Sankey, J. B., Kreitler, J., Hawbaker, T. J., McVay, J. L., Miller, M. E., Mueller, E. R., & Sankey, T. T. (2017). Climate, wildfire, and erosion ensemble foretells more sediment in western USA watersheds. Geophysical Research Letters, 44(17), 8884-8892. https://doi.org/10.1002/2017GL073979

Small, E. E., & Anderson, R. S. (1998). Pleistocene relief production in Laramide mountain ranges, western United States. Geology, 26(2), 123-126. https://doi.org/10.1130/0091-7613(1998)026<0123:PRPILM>2.3.CO;2

Syvitski, J. P. M., Vörösmarty, C. J., Kettner, A. J., & Green, P. (2005). Impact of Humans on the Flux of Terrestrial Sediment to the Global Coastal Ocean. Science, 308(5720), 376–380. https://doi.org/10.1126/science.1109454

Tarboton, D. G., Bras, R. L., & Rodriguez-Iturbe, I. (1992). A physical basis for drainage density. Geomorphology, 5, 59-76. https://doi.org/10.1016/0169-555X(92)90058-V

Tarboton, D. G. (2002), Terrain Analysis Using Digital Elevation Models (TauDEM), Utah Water Research Laboratory, Utah State University, Logan, UT; available at http://hydrology.usu.edu/taudem/.

U.S. Geological Survey. (2010). 2010 Channel Islands Lidar Collection [Data set]. https://doi.org/10.5069/G95D8PS7

Van Vuren, D., & Coblentz, B. E. (1987). Some ecological effects of feral sheep on Santa Cruz island, California, USA. Biological Conservation, 41(4), 253–268. https://doi.org/10.1016/0006-3207(87)90089-9

Vanacker, V., von Blanckenburg, F., Govers, G., Molina, A., Poesen, J., Deckers, J., & Kubik, P. (2007). Restoring dense vegetation can slow mountain erosion to near natural benchmark levels. Geology, 35(4), 303-306. https://doi.org/10.1130/G23109A.1

Verstraeten, G., Broothaerts, N., Van Loo, M., Notebaert, B., D'Haen, K., Dusar, B., & De Brue, H. (2017). Variability in fluvial geomorphic response to anthropogenic disturbance. Geomorphology, 294, 20–39. https://doi.org/10.1016/j.geomorph.2017.03.027

Wang, C., & Glenn, N. F. (2009). Integrating LiDAR intensity and elevation data for terrain characterization in a forested area. IEEE Geoscience and Remote Sensing Letters, 6(3), 463-466. DOI: 10.1109/LGRS.2009.2016986

Waters, M. R., & Haynes, V. (2001). Late Quaternary arroyo formation and climate change in the American Southwest. Geology, 29(5), 399–402. https://doi.org/10.1130/0091-7613(2001)029<0399:LQAFAC>2.0.CO;2

Wheaton, J. M., Brasington, J., Darby, S. E., & Sear, D. A. (2010). Accounting for uncertainty in DEMs from repeat topographic surveys: improved sediment budgets. Earth surface processes and landforms: the journal of the British Geomorphological Research Group, 35(2), 136-156. https://doi.org/10.1002/esp.1886

Williams, R. (2012). DEMs of difference. Geomorphological Techniques, 2(3.2).

Yan, W. Y., Shaker, A., & El-Ashmawy, N. (2015). Urban land cover classification using airborne LiDAR data: A review. Remote Sensing of Environment, 158, 295–310. https://doi.org/10.1016/j.rse.2014.11.001

Chapter 4 – Supplemental Material

1 Introduction

Presented in this supplemental are figures which provide ancillary information pertaining to data manipulation and algorithm outputs, and also figures which detail error analyses performed with this work. Additionally, two tables which provide measurements used for error calculations.

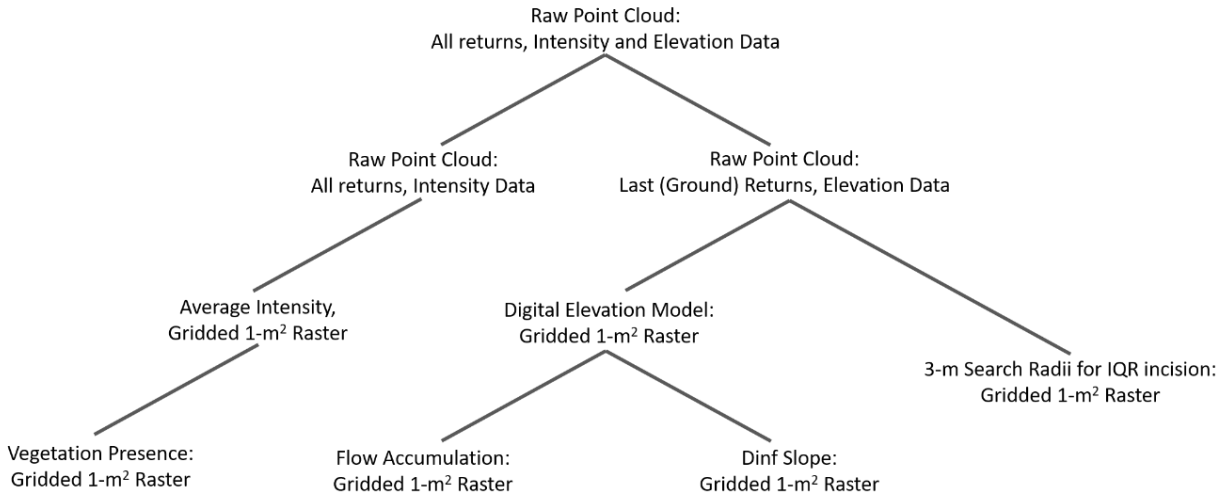

Figure S1. Topographic data manipulation from original point cloud. Final products were all clipped and aligned using ArcMap 10.4 such that extent and cell size match. Points where no data were designated were filtered out prior to calculations.

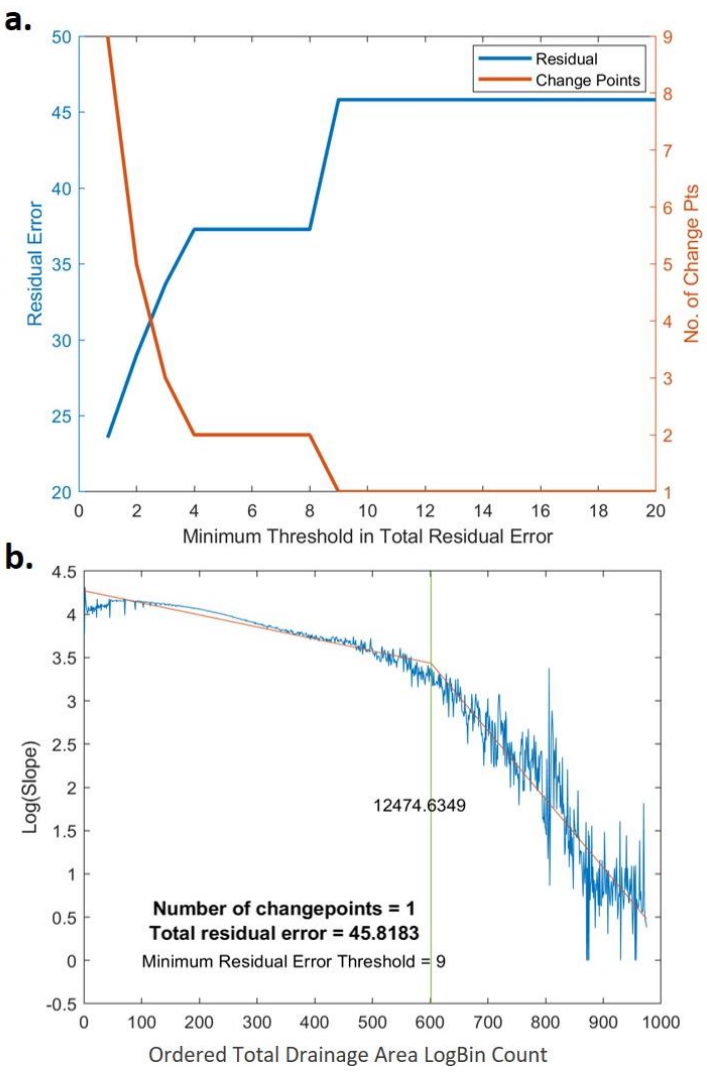

Figure S2. Transition point in total drainage area (TDA) between hillslope and fluvial geomorphic regimes calculated using a change point detection algorithm . Total drainage area was calculated using a D-infinity flow algorithm. The change point detection algorithm fits linear lines to the data, setting change points where the residual error associated with the fit of the linear lines is minimized. Total residual error is the sum of squared residuals for each linear fit. The algorithm can be dialed to a minimum threshold of residual error decrease required to identify a change point by increasing numbers of change points. An informed and reasonable balance between number of change points and residual error will need to be assessed. In our case, we expect one change point between the hillslope and fluvial regime. a. The lower the threshold, the lower the total residual error; however more change points are identified. Too many changepoints may start to identify shifts in the slopes of river channels (knickpoints) or at very high amounts track meaningless noise in the data. b. Using minimum threshold for change in residual error of 9, only one change point is detected. Visual inspection suggest that it tracks the most major shift in slope within the catchment and hence represent the change from the hillslope to the fluvial regime.

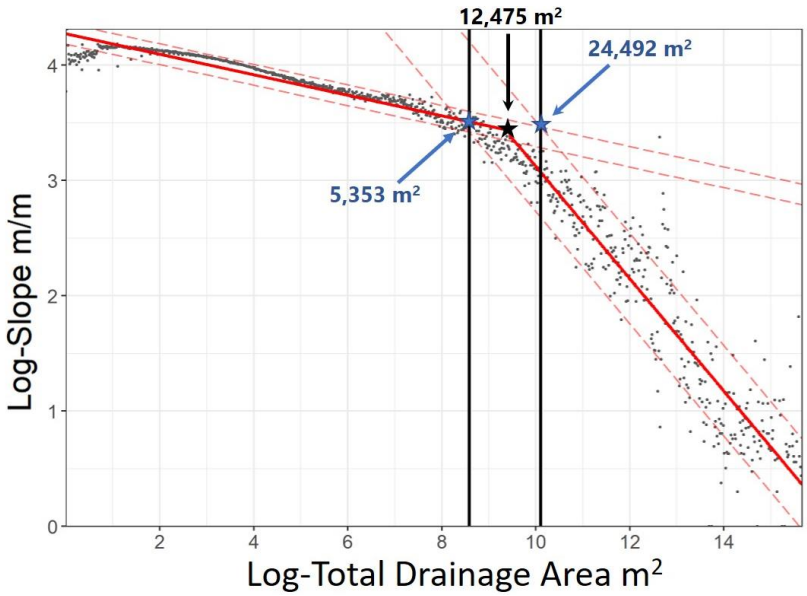

Figure S3. The transition between hillslope and fluvial geomorphic regimes in log total drainage area - log slope space. The break point, (black star, 12,475 m^2), was calculated using a change point detection algorithm based on the goodness of linear model fits and assuming a minimum decrease in residual error of 9 to produce a new change point (cf. Figure S1). Linear models were fit to the two point distributions set by the break point and the intersections of the prediction intervals at 75% confidence (red dashed lines) were calculated to produce error bounds around the break point (black vertical lines with blue stars at the intersections). Most binned means fall within the prediction bounds despite noise in the data and a relatively low confidence interval (75%). The error bounds around the break point are referred to as the transition zone in the text and represent a zone between 5,353 and 24,492 m^2 of total drainage area (marked by blue stars).

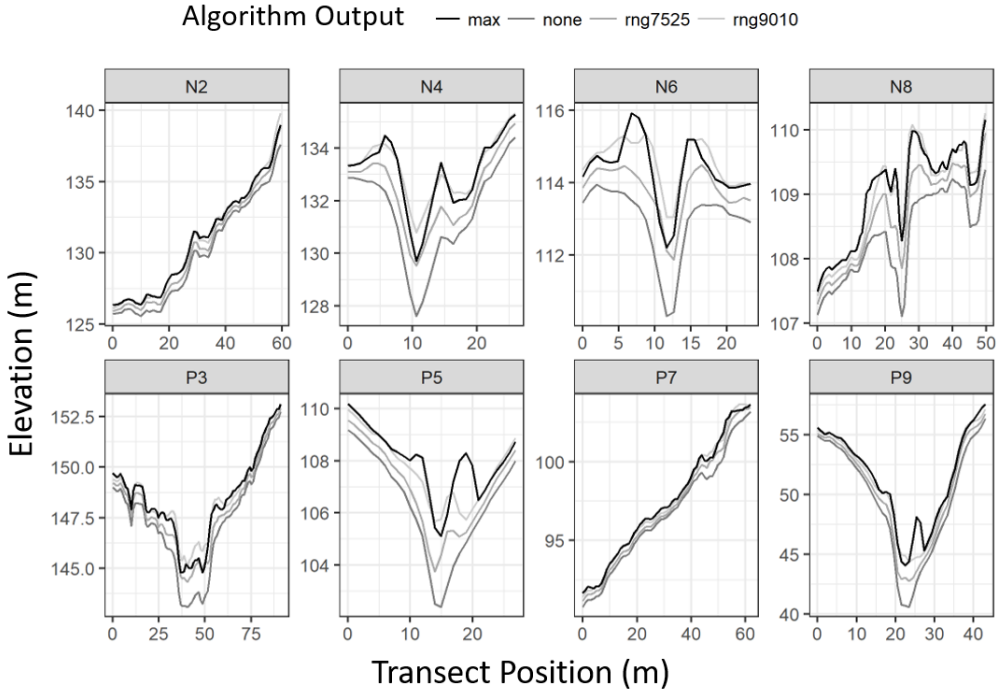

Figure S4. Elevation transects across the test sub-catchment for 2-D comparison of different smoothing algorithm products with a consistent search radius (7 m). Surfaces were produced by adding the incision raster to the original DEM. Optimal method for quantifying total incision fills in gullies with minimal added topographic artifacts. Method “none” is the original DEM. While the interquartile range method fills gullies less than methods like the maximum, visual inspection shows the produced artifacts tend to be less (minimal mounding at the rims of gullies).

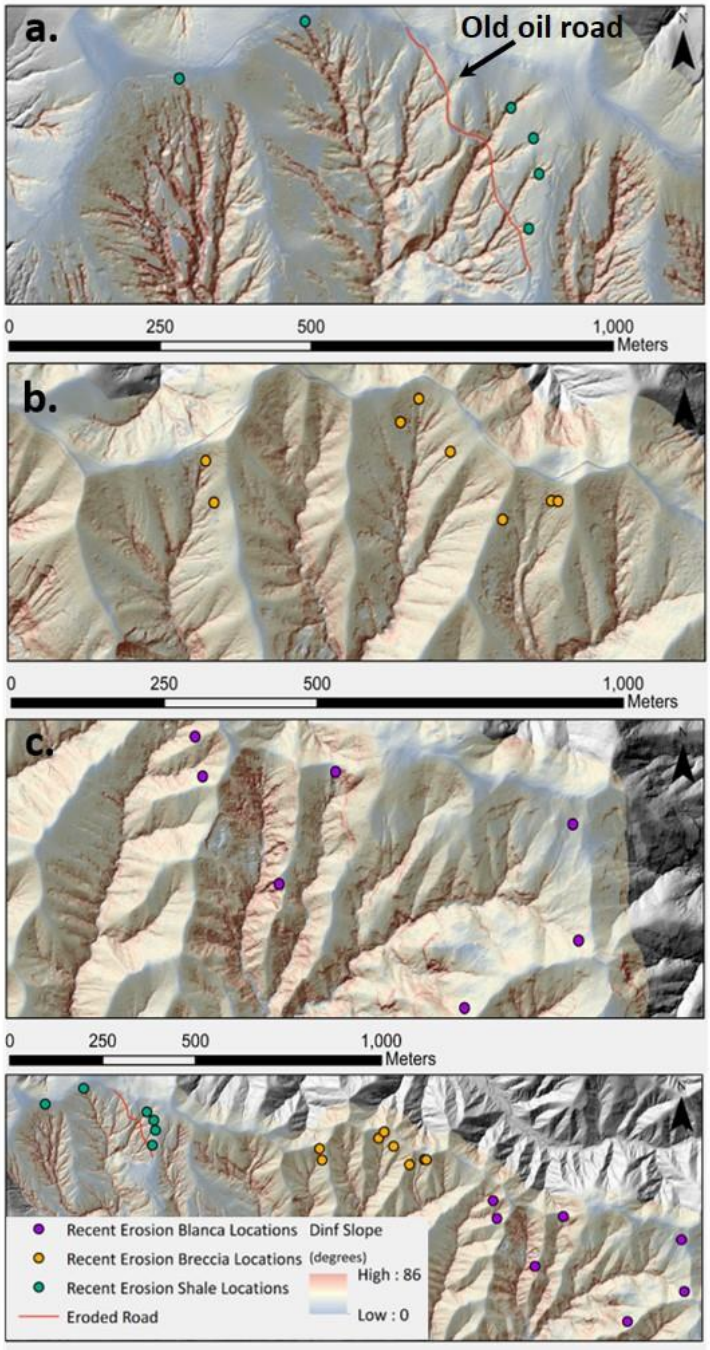

Figure S5. Locations of recent (<140 years) erosion features (colored points) used for width measurements overlaid on a D-infinity slope map for Pozo Catchment. These features were identified in the three major lithologies in Pozo (4a, b, and c) and included significant erosion above a no-longer traversable road used in the 1970's for an oil exploration operation, soil slips at the ridgecrest, and incipient gullies near ridgetops that show minimal steepening in response to the incision. Field work prior to the identification was used to inform choice of features and assure that these features were solely the product of recent perturbations. These features are fall all along the Northern ridge of Pozo in the headwaters of the catchment (bottom panel).

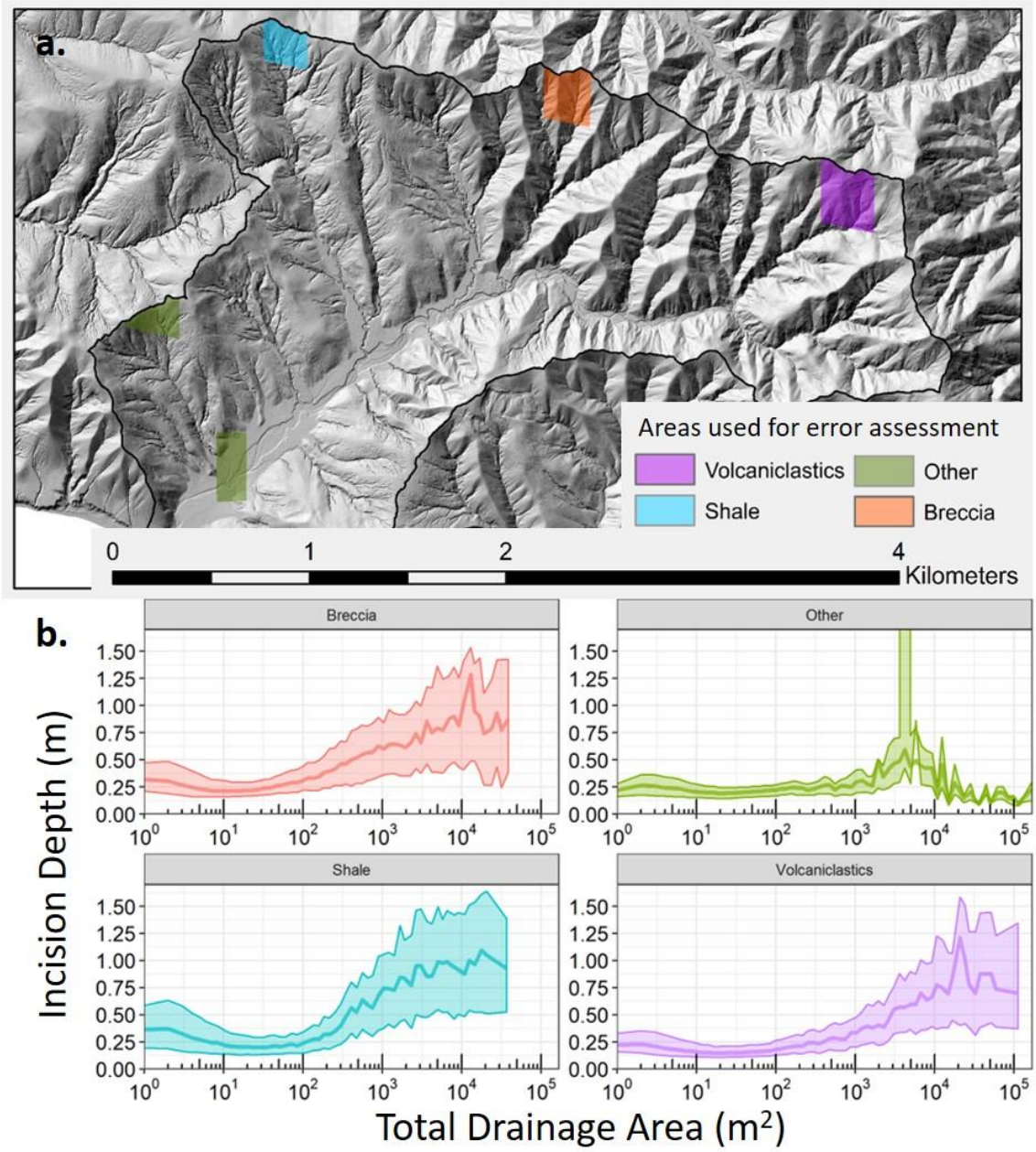

Figure S6. Selected areas used for error analyses and examples of incision error. a. Locations colored by the underlying lithology selected for error analysis – these sections were each approx. 900,000 lidar returns they covered a range in total drainage area from 0 to $>10^5$ m^2, and were underlain by one,

unique lithology. b. Incision depth compared to total drainage area for the selected areas with the error bounds produced by using a 1.7 and 4.8-m search radius shown by the lighter fill color and the 3-m search radius shown by the dark lines. The "Other" lithology here was chosen to include both a hillslope and a fill terrace area as these regions are grouped together in all other analyses.

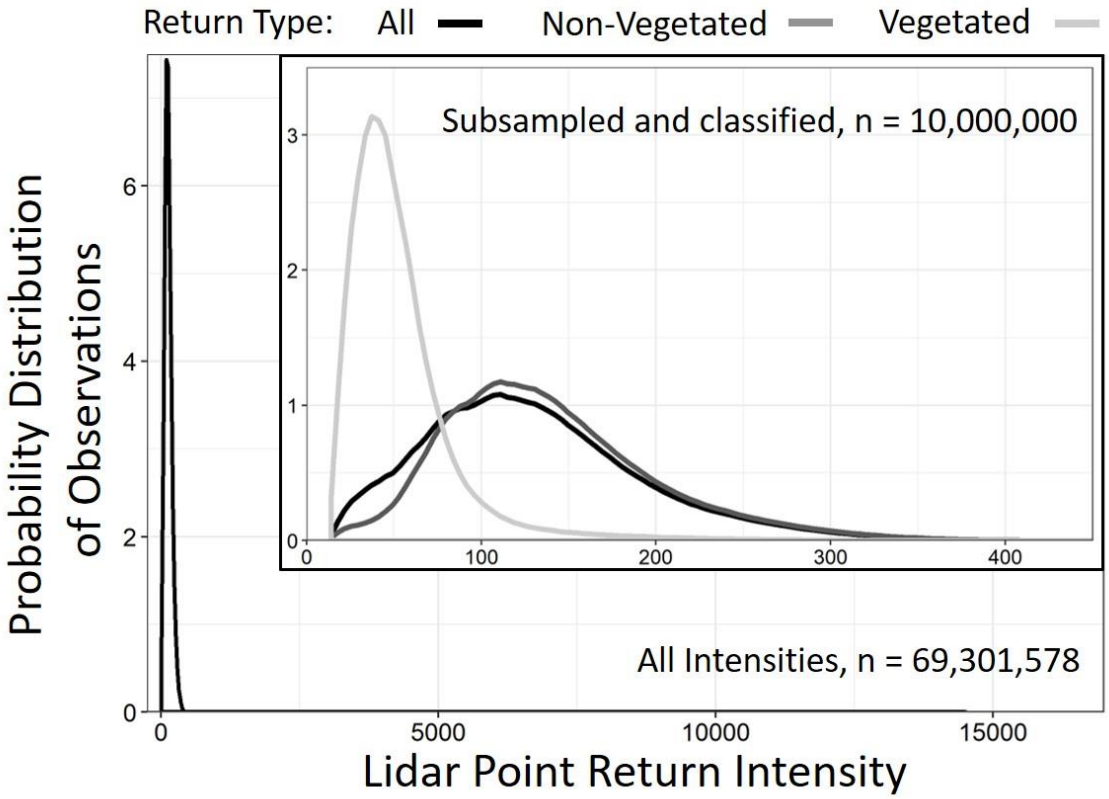

Figure S7. Full distribution of lidar return intensity values for Pozo Catchment (n = 69,301,578, with return intensities min = 16 and max = 14516). These values are stored as 16-bit data with a range specific to the sensor and flight conditions. Due to the lack of surface targets, the intensity data were not calibrated to radiances. There are 68,278,282 intensity values between 16 and 300 or 98.5 % of the return intensities measured fall within this range. inset: Point-cloud classification distributions for a random subset of the points shows lower return intensity values for vegetation returns than non-vegetated returns. The bulk of the intensity values mimic classified non-vegetated return values despite field evidence of widespread grass cover. Data are subsampled from the full dataset and the amount of non-vegetated classified returns is almost 11x more than the vegetation classified returns ($Total_n$ = 10,000,000: Veg_n = 794,472, $Non\text{-}vegetated_n$ = 8,832,554, $Unclassified_n$ = 372,974). These probabilities are produced by a kernel density estimate with a bandwidth set at 0.01 return intensities.

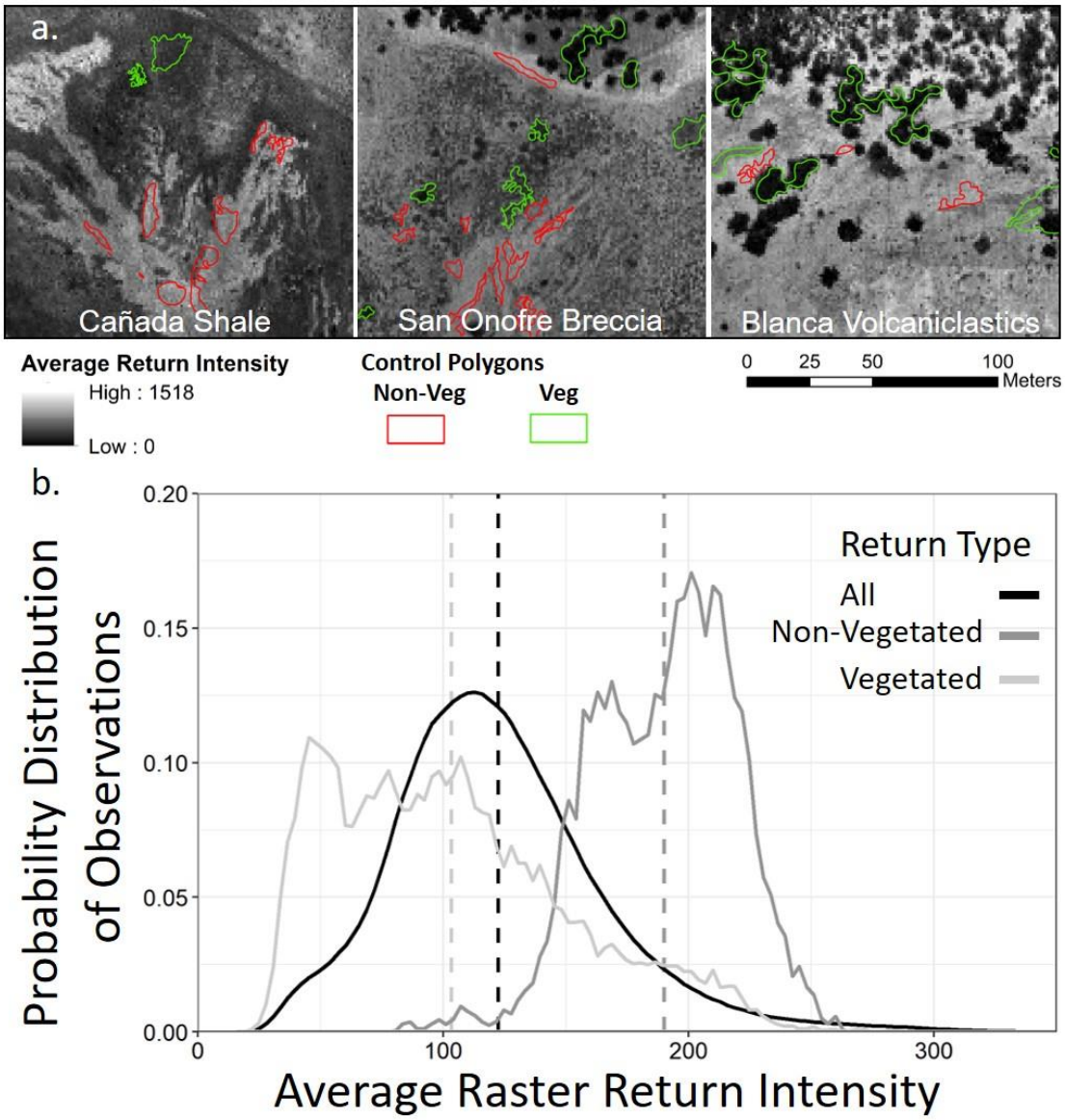

Figure S8. a. Control polygons used for the supervised classification of non-vegetated and vegetated areas. Polygons were delineated using high-resolution satellite imagery and ground-truthed with GPS measurements during fieldwork. Background data are intensity values. Note the clear gray-scale difference between NIR-absorbing vegetation and more reflective non-vegetated areas. b. Distribution of the average raster return intensity for Pozo Catchment, and the distributions from the vegetated and non-vegetated control polygons. Dashed lines display means for each distribution. The data displayed are truncated to highlight patterns for the bulk of the values (maximum average return intensity is 1518). These probabilities are produced by a kernel density estimate with a bandwidth set at 0.1 units of return intensity; Non-vegetated$_n$ = 2,462, Vegetated$_n$ = 10,514, All$_n$ = 2,543,180.

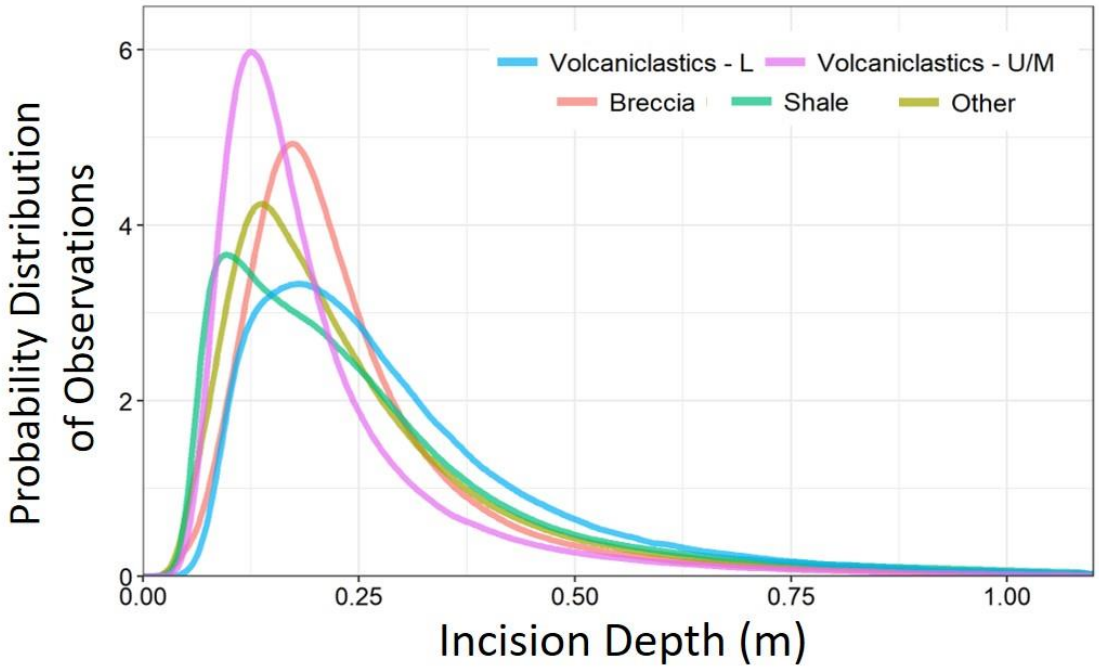

Figure S9. Incision-depth distributions for the major lithologies within Pozo Catchment using a 3-m search radius. The upper and middle members of the Blanca Volcaniclastics and the San Onofre Breccia have narrow distributions with maximums occurring between 10 and 12 cm incision depth. The lower member of the Blanca Volcaniclastics and the Cañada Shale have incision maximums within the same range, however, the breadth of their distributions is noticeably wider, showing more incision depths ranging between 25 and 50 cm. Furthermore, incision depth distribution in the Cañada Shale appears to be slightly bimodal, with the main maximum falling between 10 and 12 cm and a second, more diffuse maximum falling around 25 cm. The category of "Other" for lithologies includes minor formations with similar composition to the Cañada Shale, and the Pozo Catchment valley bottom, which has been incised during the Pleistocene and filled during the Holocene sea-level rise to produce a relatively flat and smooth terrace with a steep-walled drop to the floor of the ephemeral channel. The incision-depth distributions have long tails non-typical of normal distributions, therefore we used a Kruskal-Wallis test to evaluate differences. The test is a non-parametric version of a one-way ANOVA (Breslow, 1970); comparing the medians between the distributions. The Kruskal-Wallis test for incision-depth differences shows a small, but significant difference between different lithologies (a chi-squared value of 125440 with 3 degrees of freedom and a p-value < 2.2 e-16). These probabilities are produced by a kernel density estimate with a bandwidth set at 0.01 meters.

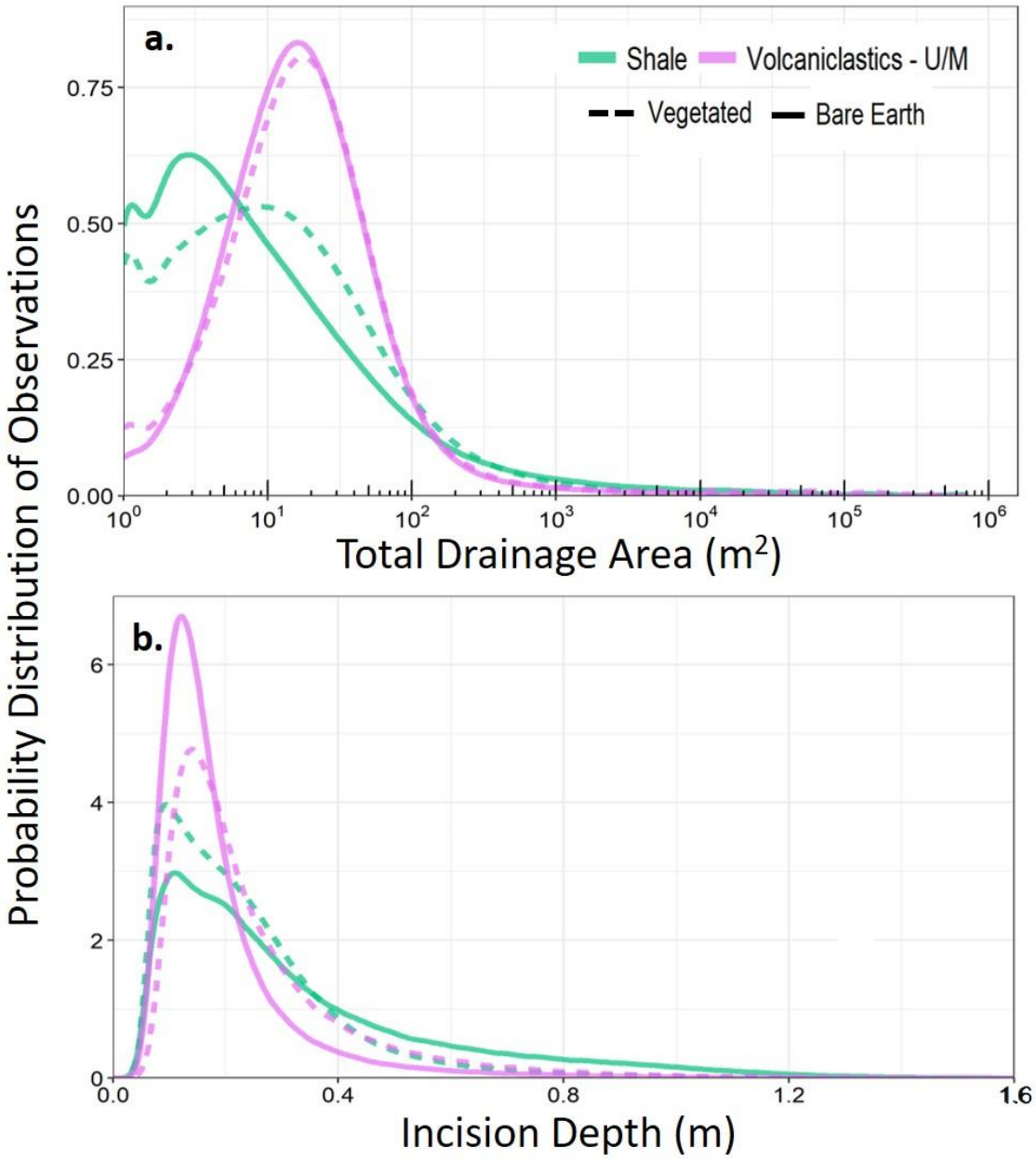

Figure S10. Vegetation distribution and influence on erosion across the landscape. a. Distribution of total drainage area (TDA) for vegetated and non-vegetated regions in the shale and volcaniclastics produced by a kernel density estimate with a bandwidth of 0.1 m^2. b. Distribution of incision depth for vegetated and non-vegetated regions in the shale and volcaniclastics produced by a kernel density estimate with a bandwidth of 0.01 meters.

Table S1. Widths of recent erosional features identified from the hillshade and manually measured using the ruler tool in ArcMap.

Lithology	Feature Width (m)
Shale	10.3
Shale	4.6
Shale	6.6
Shale	4.5
Shale	5.9
Shale	3.1
Breccia	8.2
Breccia	6.7
Breccia	9.0
Breccia	4.5
Breccia	4.7
Breccia	5.5
Breccia	12.3
Volcaniclastics	4.9
Volcaniclastics	2.1
Volcaniclastics	3.7
Volcaniclastics	13.8
Volcaniclastics	10.6
Volcaniclastics	6.5
Volcaniclastics	3.6
Average Width	6.55
Standard Deviation	3.10

Table S2. The percent differences between incision estimates at 1.7, 3.0, and 4.8 m on the sub-catchments used for error calculations (Fig. S5). The "Diff. above" and "Diff. below" indicate the percent difference between the 4.8 and 3.0, and 1.7 and 3.0 mean incision and total incision. These percent above and below values were used to produce high and low estimates for mean and total incision for the whole Pozo Catchment.

Geomorphic Regime	Lith.	3 m Rad. Mean Incision-Depth (m)	Diff. above	Diff. below	% above	% below	3 m Rad. Total Incision (m^3)	Diff. above	Diff. below	% above	% below	Catchment Area (m^2)	% of Total Area
Hillslope	Breccia	0.25	0.12	0.07	0.46	0.30	15,217.35	7,025.64	4,527.36	0.46	0.30	60580	0.2245
Hillslope	Other	0.23	0.08	0.06	0.37	0.28	19,047.37	6,965.75	5,340.31	0.37	0.28	83719	0.3102
Hillslope	Shale	0.29	0.18	0.13	0.63	0.43	12,493.25	7,903.58	5,430.75	0.63	0.43	42750	0.1584
Hillslope	Volcaniclastics	0.17	0.08	0.05	0.47	0.29	13,160.20	6,231.81	3,823.00	0.47	0.29	78415	0.2906
Transition	Breccia	0.92	0.43	0.48	0.47	0.53	302.63	142.02	159.35	0.47	0.53	330	0.0012
Transition	Other	0.37	0.17	0.06	0.47	0.16	231.83	107.81	38.18	0.47	0.16	624	0.0023
Transition	Shale	0.99	0.52	0.47	0.53	0.48	308.74	163.26	147.35	0.53	0.48	313	0.0012
Transition	Volcaniclastics	0.73	0.36	0.35	0.49	0.49	263.77	129.97	128.78	0.49	0.49	363	0.0013
Fluvial	Breccia	0.91	0.50	0.49	0.55	0.54	102.48	56.75	55.60	0.55	0.54	113	0.0004
Fluvial	Other	0.24	0.10	0.09	0.42	0.37	201.12	83.63	73.91	0.42	0.37	826	0.0031
Fluvial	Shale	0.93	0.46	0.40	0.49	0.43	10.21	5.01	4.41	0.49	0.43	11	0.0000
Fluvial	Volcaniclastics	0.82	0.54	0.43	0.65	0.52	163.48	106.65	84.79	0.65	0.52	199	0.0007

Chapter 5. Chemical weathering patterns and evidence for rock-derived nitrogen contributions at the pedon-scale in a Mediterranean grassland

Key Points

- Chemical weathering and nitrogen (N) dynamics studied from a ridgetop positioned, 4-meter pedon.
- Chemical weathering is low compared to total denudation rates.
- Rock-N flux from shale to a semi-arid, Mediterranean grassland is 0.58 – 1.07 kg ha^{-1} yr^{-1}.

Abstract

Rock-derived nitrogen is a globally important contributor to the terrestrial nitrogen cycle, however most research on the pedon-scale mixing of rock-derived nitrogen with atmospherically derived nitrogen is limited to forested, montane ecosystems underlain by mica-schists in Northern California. Little is known about its pedon-scale importance to ecosystems during soil production and its fractional contribution in varying climates and biomes. This work evaluates the relative chemical weathering of a soil within a semi-arid, Mediterranean grassland undergoing moderate uplift and erosion. Furthermore, this work brings together field, geochemical, and nitrogen-specific analyses to show distinct pools of surface and bedrock sourced nitrogen and potential pathways for rock-derived N to enter the ecosystem. We estimate a bedrock-derived N flux to the solum of 0.58 – 1.07 kg ha^{-1} yr^{-1}, which is ~0 to 15% of annual N inputs depending on the atmospheric and fixation fluxes. This work demonstrates that rock-derived N is contributing to our ecosystem but chemical weathering limitations allow atmospheric additions to dominant the total N budget for our semi-arid, Mediterranean grassland ecosystem.

1 Introduction

Recent work demonstrates that nitrogen (N) stored in bedrock as ammonium (NH_4^+) trapped in the interlayer of crystalline minerals can play a substantial role in aboveground primary productivity (Morford et al., 2011). Global and regional models show rock-derived nitrogen adding 6-17 percent to the global N budget (Morford et al., 2016a; Houlton et al., 2018). However, pedon-scale, or surface solum to unweathered bedrock, analysis of rock-derived nitrogen has been limited to low-grade metamorphic lithologies and humid climates (Morford et al., 2016b). Given the complexity of rock weathering, it is necessary to expand pedon-scale research to other lithologies, climates, and tectonic settings if rock-derived nitrogen is to be considered in further ecological studies.

Identifying the contribution of rock-derived N at the pedon-scale is complicated by the significant input of N from the surface, either through wet and dry deposition of different N forms or fixation by free-living bacteria, in the root nodules of some plants, or by lightning (Fig. 1). Identifying rock-derived N can be done using chemical extractions for NH_4^+ bound in the crystal matrix of silicate minerals (Morford et al., 2016b), however much of the N in sedimentary bedrock is in poorly characterized organic and mineral forms requiring different quantitative analyses. Inferences of the preferred pathways and products of the N cycle throughout the pedon and the relative availability of N for plants can be made by identifying mineral forms of N within the pedon (Haynes, 2012). Furthermore, as N is transformed into different forms via these different pathways, the isotopic signature δ15N is altered for the bulk soil and for different N reactants and products (Hobbie and Ouimette, 2009). Inferences for the sourcing of N throughout the profile can be made using the δ15N signature N (Craine et al, 2015), but that is only viable if analyses are extended into unweathered bedrock, where clear surface and depth endmembers can be established.

The rate at which NH_4^+ is released from silicates or fossilized organic matter (FOM) (Holloway and Dahlgren, 2002) is set by the chemical weathering of the bedrock (Fig. 1 – red and blue arrows indicating higher and lower fluxes, respectfully). Chemical weathering rates can vary over lithologic (Heckman and Rasmussen, 2011), climatic (Chadwick et al., 2003), and tectonic (West et al., 2005) gradients. Release of a specific element within an ecosystem can be quantified by combining total denudation rates with mass balance calculations using a minimally mobile index element within the soil and bedrock (Riebe et al., 2003) to assess the proportional flux from chemical weathering within a soil (Riebe et al., 2003). Chemical fluxes of proxy elements can be used to estimate rock-derived N fluxes in the absence of a direct quantification of rock-derived N in the soil (Houlton et al., 2018).

Here we provide an estimate of the importance of rock-derived N to a Mediterranean Oak Grassland ecosystem. We first assess the chemical weathering within the pedon and then use this to explain depth patterns of nitrogen pools and δ15N signatures. We then estimate a rock-derived N flux from the bedrock using chemical weathering mass balances and check these flux estimates against a soil N and δ15N mixing model. This work provides a water-limited end member to existing pedon-scale rock-derived N work, expanding the range of ecosystems over which we understand the contributions of rock-derived N.

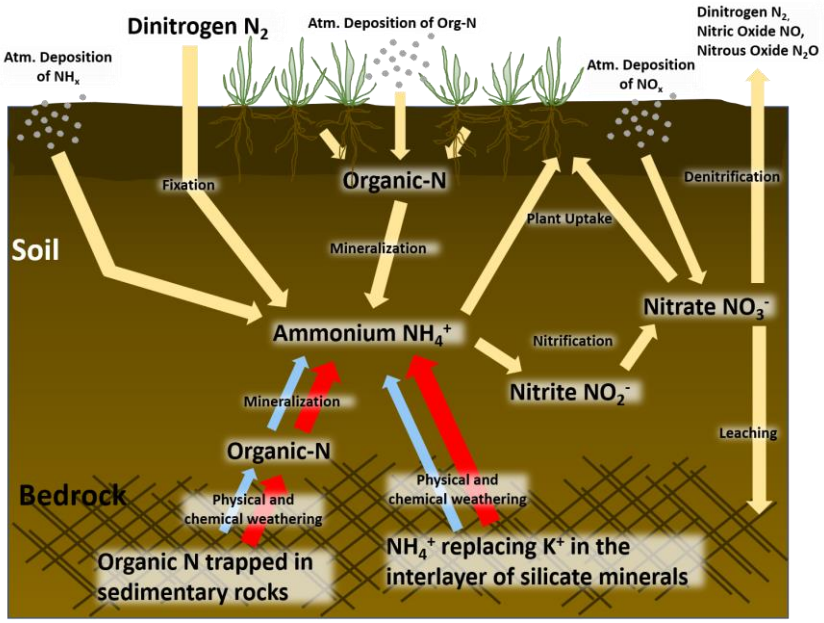

Figure 2. Simplification of the nitrogen cycle including rock-derived N. The colored arrows from the rock-derived nitrogen indicate a relative flux; red (fast) and blue (slow), dependent on the rate of bedrock weathering as set by climate, tectonics, bedrock composition, etc.

2 Materials and Methods

2.1 Study Site

The study site provides a water-limited endmember with comparable bedrock-N concentrations, but different lithology to previous pedon-scale work (Morford et al., 2016b). The pedon is located on Sedgwick Reserve, a UC Reserve in the Santa Ynez Valley of central California (Fig. 2a & b). The area is characterized by a Mediterranean climate; cool, wet winters and warm, dry summers. The mean annual precipitation is 380 mm and the mean annual temperature is 16.8^{o}C. The Santa Ynez mountains reduce marine deposition of N and ions such as chloride (Cl^-), sodium (Na^+), and calcium ($Ca2^+$) are lower than surrounding areas (Chow et al., 1996; National Atmospheric Deposition Program, 2019). Total N deposition between 2015 and 2017 for the sample location averaged 6.07 kg ha^{-1} yr^{-1} and was dominated by NH_x and HNO_3^- forms (National Atmospheric Deposition Program, 2019). Deposition of Cl, Na, and Ca over the same time period was 2.97, 2.90, and 1.21 kg ha^{-1} yr^{-1}

respectively (National Atmospheric Deposition Program, 2018). Precipitation can vary dramatically year to year (Haston and Michaelsen, 1994) which affects the frequency that water infiltrates deep into the soil and bedrock (Chamran et al., 2002). The sampling site is situated in an oak grassland dominated by annual grasses, *Bromus* and *Avena*. The bedrock is a low-energy depositional environment facies of the Paso Robles - organic-rich mudstone with lenses of carbonate facies (Dibblee, 1966). Nitrogen in this type of lithology can be in both NH_4^+ in interlayer crystalline clays or as organic-N trapped as micro-detritus during diagenesis (Holloway & Dahlgren, 2002). The pedon was sampled on a convex ridgetop which loses soil and moisture to downslope catena locations (Gessler et al., 1990; Chamran et al., 2002). Assuming atmospheric deposition is relatively uniform within the study site, higher C and N concentrations in convex positions can be attributed to lower decomposition rates (Lin et al., 2015).

The pedon is placed in a convex, ridegcrest landscape position to assure access to unweathered bedrock and eliminate any influence of colluvial material which would provide an additional source of rock-derived nutrients to the solum and complicate weathering calculations. The ridgecrest pedon was excavated to a depth of 250 cm in early February 2018 (Fig. 2d – h) and extended to 415 cm with an auger in May 2018. We divided the pedon into three distinct sections; 1) the solum (0-100 cm), which encompasses A and B horizons and is most physically disturbed by gopher activity, 2) the saprolite (100-250 cm), which encompasses chemically altered bedrock with minimal physical disturbance, and 3) the unweathered bedrock (250+), which consists of bedrock with minimal chemical and physical weathering. For the purpose of mass balance calculations, the parent material will refer to section 3 of the pedon, the unweathered bedrock. These section breaks were informed by

field observations during excavation of the pedon and a full discussion of the pedon characteristics is presented in section 3.1. These sections will be referenced throughout the rest of this work. Soil samples were taken by identified soil horizon within the 1-m thick surface solum and from visibly identifiable changes within the facies of the underlying saprolite to 250 cm. Samples of the unweathered bedrock were taken by auger-bucket-full at the depth of strongest expression of a bedrock facies.

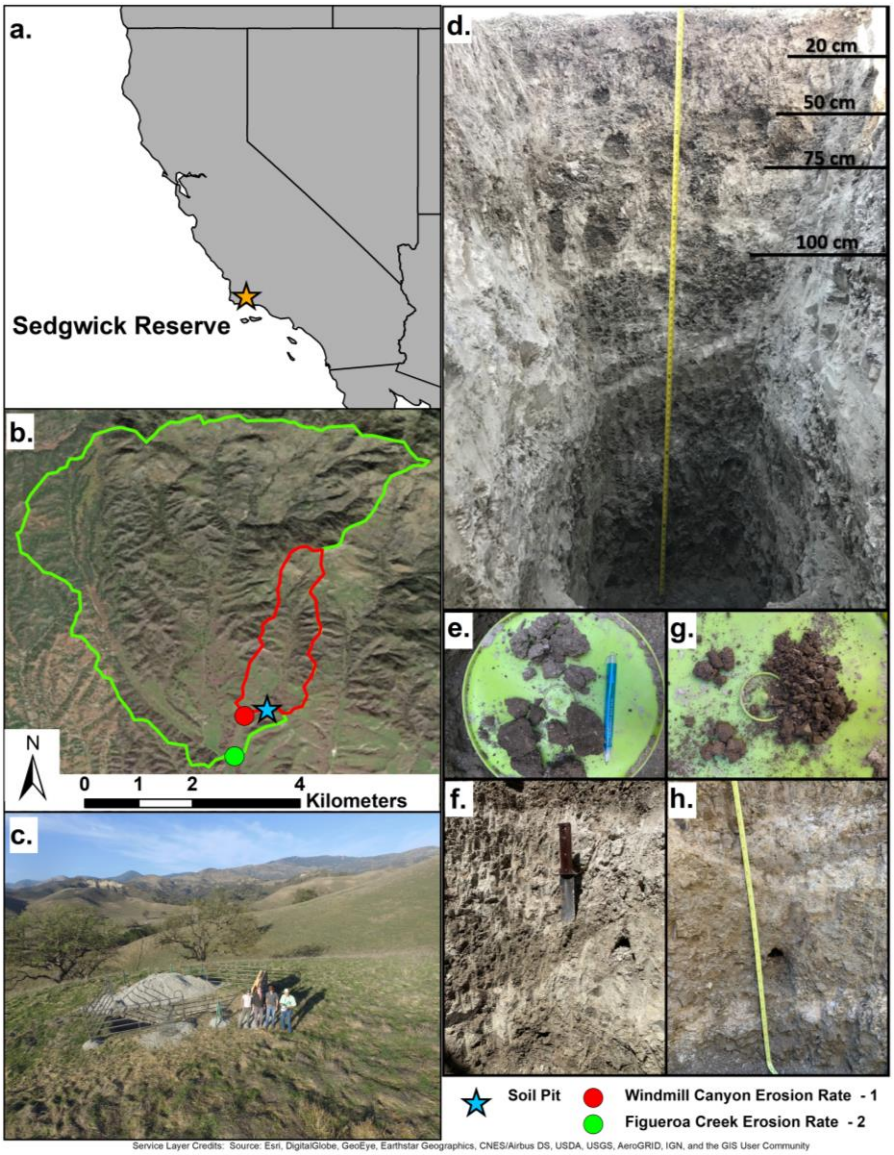

Figure 2. Study site map and photos. a. Location of Sedgwick Reserve. b. The soil pit and catchment average erosion rate sampling locations with the associated catchment outlines in corresponding color. c. Northward view of soil pit and surrounding area. Aerial footage of the soil pit taken by drone on Feb. 11th, 2018. d. Pedon

profile to 250 cm with major horizon depth-breaks within the solum indicated. e. B horizon peds showing drier and more carbonate rich peds on top and more moist and less carbonate rich peds on bottom. f. Pedon profile from ~65 cm to 145 cm showing carbonate horizon and then alternating lenses of carbonate and shale in the saprolite. g. Shale fragments and soil peds from 60-75 cm showing a little reddening and also carbonate mottles. h. Pedon profile from 145 to 200 cm showing more defined alternating shale and carbonate lenses within the saprolite. The gopher hole at depth was dug after excavation and the sampling, when pit infilling raised the bottom of the soil pit sufficiently to allow gophers to dig into physically undisturbed saprolite.

2.2 Soil geochemical analyses & weathering calculations

2.2.1 Analyses & mass balance

Surface solum to unweathered bedrock element concentration profiles are derived from ground <2-mm fraction for the solum and ground bulk samples for saprolite and unweathered bedrock. These samples were analyzed for bulk elemental concentrations via ICP-AES at ALS-Chemex in Reno, Nevada. Weathering patterns in the mobile soil are calculated using a mass-balance approach (Brimhall & Dietrich, 1987; Chadwick et al., 1990). High field strength elements are less likely to be chemically mobile within a soil profile and can be used as a normalizing index (i) against which biologically relevant elements (j) can be referenced to understand chemical weathering. We use the index element to calculate change in individual elements within the solum (w) and saprolite bedrock (w) relative to their concentrations in unweathered bedrock (p). This chemical mass transfer coefficient (τ) (Eqn. 1) provides relative loss or gain of an element within the solum.

$$\text{Equation 1. } \tau = \left(\frac{C_{j,w} * C_{i,p}}{C_{j,p} * C_{i,w}}\right) - 1$$

Here we use titanium as the "immobile" index element - see the Supplemental Material (S2) for further discussion on the choice of index element. The elemental composition of parent material was determined by depth-averaging concentrations for the varying rock facies identified from 250 to 415 cm. Positive Tau values indicate additions with respect to the parent material, while negative values indicate losses with respect to the parent material.

2.2.2 Rock-derived N flux estimates

Nitrogen specific chemical weathering flux from the unweathered bedrock to the solum is estimated using proxies for both silicate-bound N and organic-N. We estimate the fluxes of silicate-bound N proxies (W_e) as a fraction of the total denudation (D) within a landscape by combining the mass balance of elements between the soil and parent material and an estimate of total denudation (Riebe et al., 2003). If a landscape is in steady state, total denudation is equivalent to the rate of soil production everywhere on the landscape (Heimsath et al., 1997). Constraining total denudation rates, and consequently the soil production rates, at the study site is complicated due to an imbalance between erosion and uplift in the region which sets the system out of steady-state (c.f. Chapter 3). The landscape is eroding more slowly than the current estimated uplift rates, producing widespread valley infilling. This infilling leads to spatial variation in soil thickness which corresponds to spatial variations in soil production rates where soil production rates may still be in balance with uplift rates at the ridgecrest but slow dramatically downslope (Yoo et al., 2009). Therefore, we use a range of total denudation rates that bracket the potential soil production rates for the area given the balance between geologic-timescale uplift and erosion rates, 0.1 – 1.0 mm yr^{-1}. See Chapter 3 of this thesis for a further discussion on the choice of denudation/soil production rates. Combining the erosion rate with a negative, profile averaged τ value for a given element (Tau_e or τ_e), the concentration of the element in the parent material (C_e), and the bulk density (B) estimate for the parent material provides the element specific flux (W_e) from the parent material to the mobile soil (Eqn. 2).

Equation 2. $W_e = C_e * B * -Tau_e * D$

Bulk density (B) was only calculated for samples between 0 and 250 cm because auger sampling (250-415 cm) destroys the structure of peds and rock fragments (Table S2-1). Depth weighted averages were calculated for soil (0-100 cm) and lower half of the saprolite (150-250 cm). This saprolite bulk density value is used to approximate unweathered rock density.

Chemical weathering fluxes W_e) were calculated using a set of elements (Si, K, P) assumed to bound the weatherability of NH_4^+ in silicate minerals. Silicon is a low-estimate end-member given its relatively immobile behavior in soil. Potassium is often replaced by ammonium within silicate minerals due to similar ionic radii (Juster et al., 1987; Holloway and Dahlgren, 2002). Lastly, P offers a single-source comparison for nitrogen: P is primarily derived from bedrock (Vitousek et al., 2010). We did not use Na, despite previous work using Na for continental- and global-scale weathering models focused on rock-derived N fluxes (Houlton et al., 2018). Sodium concentration is elevated in the solum, suggestive of a significant atmospheric addition that would skew parent material weathering calculations.

To calculate an organic-N flux we use a range of fossilized organic matter (FOM) erosion rates from Copard et al (2007) combined with the C/N ratio of the parent material in the style of Houlton et al (2018). Here, FOM refers to organic matter trapped with the sediment and retained during diagenesis. We chose a range of FOM flux rates for the central California region derived from a global FOM flux rate map at the 1^o pixel scale (Copard et al., 2007). These rates in units of t yr^{-1} were converted to kg ha^{-1} yr^{-1} using 34^{o}N as the conversion latitude for degrees to meters. We do not parse the proportions of organic-bound N versus silicate-bound N in this study, but provide a possible range of fluxes if the N was entirely organic- or silicate-bound.

2.3 Nitrogen-specific analyses

2.3.1 Extractions and mineral forms

Total C [C_{total}] and N [N_{total}] were determined via combustion using a PDZ Europa ANCA-GSL elemental analyzer at UC Davis Stable Isotope Facility on ground <2-mm fractions for the solum and ground whole samples from the saprolite and unweathered bedrock. Mineral forms of N and labile anions were measured from ground samples extracted using 1 M KCl and milliQ-water in a 5:1 ratio of solute to sample for 3 hours. Water extracts were used to determine labile anion concentrations. Potassium chloride (KCl) extracts were used to separately determine [NO_3^-] and [NH_4^+]. Samples were ground to minimize extraction discrepancies produced by particle size differences between solum, saprolite, and unweathered bedrock. Labile anions, including phosphate (PO_4^{3-}), chloride (Cl^-), and sulfate (SO_4^{2-}), were measured on an ion-chromatograph at UC Riverside.

Following Hood-Nowotny et al (2010), NH_4^+ concentration was determined by a colorimetric analysis using Berthelot's reaction and measured at 600 nm wavelength on a micro-plate reader. Nitrate concentration from the KCl extraction was determined by the reduction of nitrate to nitrite using vanadium (III) chloride and the colorimetric reaction of nitrite with the Greiss solution and subsequent measurement on the plate-reader at 540 nm (Hood-Nowotny et al., 2010). Mineralization can continue within the lab even as the samples are dried down (Scherer et al, 1992), therefore our mineral N data should be interpreted as internally robust patterns but care should be taken when comparing our results to "field-status" mineral-N data.

2.3.2 Nitrogen Isotopes

Ground samples (25-35 mg subsample, duplicated) were foil wrapped and natural abundance isotopes of total N were measured at UC Davis Stable Isotope Facility using a

PDZ Europa ANCA-GSL elemental analyzer connected to a PDZ Europa 20-10 isotope ratio mass spectrometer. Standard deviation for these values is 0.3 per mil for δ15N. Water extracted NO_3^- was analyzed for natural abundance $\delta^{15}N$ at the UC Riverside Facility for Isotope Ratio Mass Spectrometry using the bacterial denitrifier method, which relies on the production and analysis of N_2O from denitrifying bacteria consuming NO_3^- (Sigman et al., 2001). For both analyses data are presented in delta notation using air as the standard (Eqn. 3).

$$\text{Equation 3. } \delta^{15}N‰ \text{ vs. Air } = 1000 * \frac{{}^{15N_S}/_{14N_S} - {}^{15N_{Air}}/_{14N_{Air}}}{{}^{15N_{Air}}/_{14N_{Air}}}$$

3 Results

This section first presents a detailed field description of the pedon and the soil taxonomic classification for the solum. We then explore the concentration-depth patterns of total N and the mineral fractions. Anion data is presented in conjunction to the mineral N to help elucidate depth patterns. We also include a depth profile of total N-δ15N values to explore the usage of isotopes as a tracer for rock-derived N. Lastly, we explore depth patterns of the elements used as proxies for rock-derived N and estimate the flux of rock-derived N to the solum.

3.1 Pedon description and taxonomic classification

The plants surrounding the pedon are primarily annual grasses (*Bromus* and *Avena*) with a rooting depth about 20 cm. The pedon is heavily bioturbated from gopher (*Thomomys bottae*) burrowing. The deepest gopher burrow uncovered during the digging process was 110cm, however most gopher burrows were between 0-75 cm, with the highest density near the surface of the pedon. In deeper horizons (50-75 cm) gopher spacing is 20-40 cm in any

direction and hole dimensions are either 10 cm tunnels running sub vertical or vertical or spheroid with 10 cm diameter. In-place bedrock structure appears at 50 cm, but 50% of the horizon at 50-60 cm shows pedogenic structure and carbonate accumulation within the gopher back-filled burrows. Mottles of calcium carbonate ($CaCO_3$) appear by 20 cm and increase in size and percent area coverage to 75 cm, where there is a $CaCO_3$ cemented horizon. There is a visual reddening of the Bk/C2 horizon which sits directly above the $CaCO_3$ cemented horizon. The horizons with $CaCO_3$ present are reflected in the concentration of inorganic carbon, [C_{inorg}], with depth (Fig. 3).

The presence of $CaCO_3$ in the soil pit is unique to this study site – field observations of in other parts of Sedgwick Reserve show limited presence of calcic horizons. Atmospheric deposition maps show a non-insignificant flux of Ca per year to the surface (National Atmospheric Deposition Program, 2019), however the patchy nature of calcic horizons in the area implicate another source or control on the presence of $CaCO_3$ within the soils. Given the presence of $CaCO_3$ layers within the unweathered bedrock (Fig. 3, >250 cm), we assume the source of $CaCO_3$ for this horizon is at least in part from the bedrock. Gophers are the mechanism for bedrock-derived $CaCO_3$ present in the soil: bringing $CaCO_3$ up from the saprolite to the surface where it can be dissolved, mobilized, and reprecipitated. The significant accumulation of $CaCO_3$ in the BkC3 horizon is similar in composition ($CaCO_3$ matrix surrounding tiny shale fragments) to deeper $CaCO_3$ layers which suggests the $CaCO_3$ in this horizon may be both pedogenic- and bedrock-derived. We consider the base of the solum as the bottom of this horizon (100 cm) – marking the transition between pedogenic-influenced and bedrock-influenced portions of the pedon.

Beneath the solum, the saprolite gradually increases with physical competency with depth. The increase in physical competency is demonstrated by the increase in fragment size for the shale facies; 1-3 cm near 100 cm to 3-5 cm by 200 cm. Additionally, the distinction between carbonate-rich and shale facies of the Paso Robles becomes more pronounced with depth (Fig. 2f versus 2h). During excavation of the pedon, these shifts in physical characteristics were used as an indicator for a decrease in chemical weathering and a transition to unweathered bedrock by 250 cm. A detailed description of the pedon is presented in Table 1.

The pedon lies within a unit mapped at 1:24,000 scale by the US Department of Agriculture Natural Resources Conservations Service (NRCS) on a as Typic Xerorthents, indicative of minimal soil development (Soil Survey Staff, 2019). However, the pedon-specific field description classifies it as a Calcic Haploxeroll because of the presence of there a mollic epipedon and calcic horizons in the solum (Table 1). The soil color for the surface horizon are on the lighter side for a mollic epipedon classification, which may be due to dispersed carbonates within the A horizon. Previous work in the area also described soils in ridgetop locations as Calcic Haploxerolls (Lin et al., 2015).

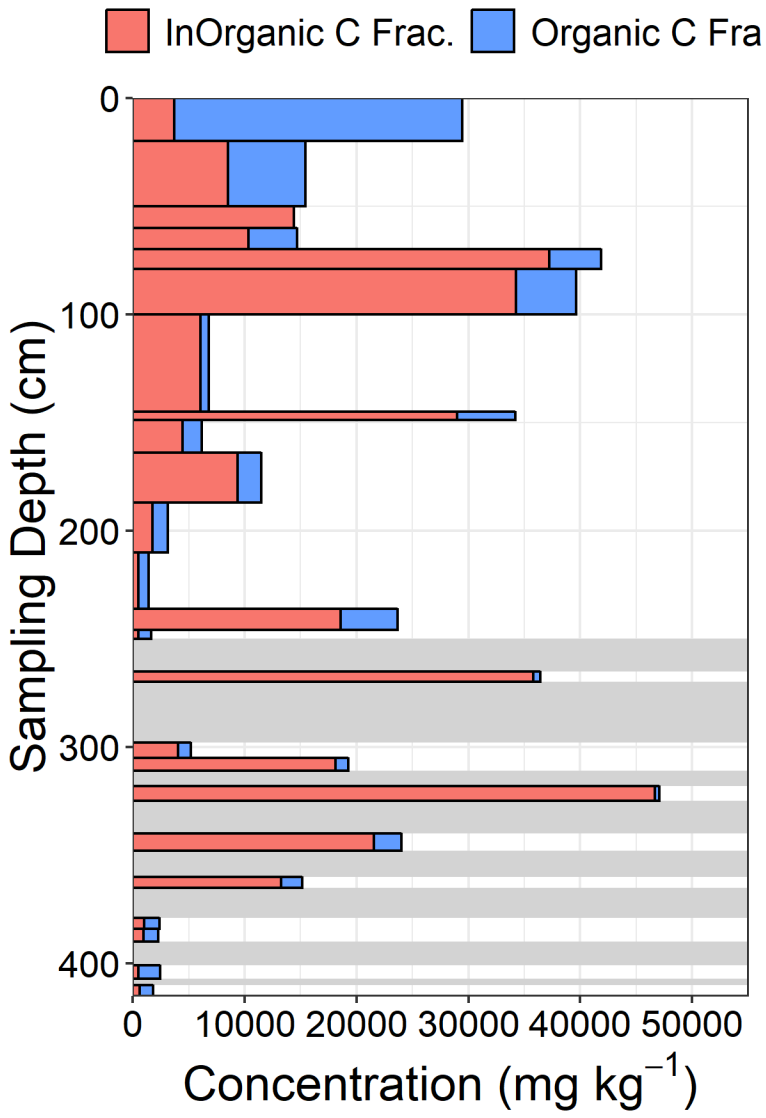

Figure 3. Organic and inorganic carbon concentrations in the soil and parent material for the soil. Grey bars indicate unsampled depth ranges.

Table 2. Detailed profile description of the first 150 cm of regolith.

Horizon Designation	Major distinction	Horizon Break	Depth (cm)	Texture Class	Structure	Color (moist)	Color (dry)	Rock Fragments	Mottles (% Area)	Chemical Reaction with 10% HCl
A	Rooting depth for annual grasses. Many very fine and fine roots.	clear, smooth	0-20	Silt loam/Silty clay loam (least clay)	strong, medium, subangular blocky	10YR 3/1,2; 2.5Y 3/1,3	N/A	10% ≤1mm shale and carbonate pebbles	n/a	slightly effervescent
Bw/Bk	Soil without bedrock, some areas are drier and have visible accumulation of carbonate (dry peds - 50% area)	gradual, smooth	20-50	Silty clay loam (3rd least clay)	strong, coarse, subangular blocky	moist peds: 2.5Y 3 or 4/2, dry peds: 2.5Y 4/2	dry peds: 2.5Y 5 or 6/2	moist peds: 10% ≤1mm shale and carbonate pebbles, dry peds: 15% ≤1mm shale and carbonate pebbles	dry peds have 10% 1-3mm mottles	strongly effervescent
Bk/C1	Pedogenic-influence to form peds (60% of area), but also distinct areas of bedrock fracture pattern (40% of area), both sections have carb accumulation	clear, wavy	50-60	Silty clay loam (2nd most clay)	soil: weak, medium, subangular blocky, bedrock: 1-2 cm shale fragments with in-place fracture texture	soil: 2.5 Y 4/3, dry shale: 2.5Y 6/3, moist shale: 2.5Y 5/2, carbonate mottles: N or 2.5Y 9.5/1 , carbonate flecks: 2.5Y 9/1	dry shale: 2.5Y 5/2	15% ≤1mm shale and carbonate pebbles	15% powdery mottles present on fracture faces	soil strongly effervesces, shale does not, carbonate mottles strongly effervesces
BkC2	Reddening of this horizon and higher accumulation of carbonates, shale dominates this horizon (60%) and soil is present in between shale fragments or in gopher holes (40% of area). This is the deepest horizon with roots: very few and very fine roots.	abrupt, irregular	60-75	Silty clay loam (most clay), Shale fragments have shiny or slick faces	shale bedrock predominates, the soil structure is around and between shale or in a backfilled gopher hole. Soil: weak, very fine subangular blocky crumbling to very fine to fine granular (especially in gopher holes). Bedrock: 1 cm shale frags in-place fracture texture	soil: 2.5Y 4/3, shale: 2/5Y 4/2 (Looks redder in the field and pictures but was not reflected in the color necessarily), carbonate mottles: N or 2.5Y 9.5/1	n/a	15% ≤1mm shale and carbonate pebbles	20% powdery mottles present on fracture faces, bigger blotches than horizon above	strongly effervescent
BkC3	Strong, bright white carbonate horizon, likely this calcium carbonate is both reprecipitated and in-situ derived form a	clear, wavy	75-90	n/a	massive	5Y 7.5/1	5Y 8/1	%15 <1 -3 mm pebbles within the carbonate matrix	n/a	violently effervescent

	calcium carbonate rich lens of the bedrock									
Cr1	Discontinuous shale and carbonate layers	clear, broken	90-145	n/a	alternating 1-3 cm fractured shale and massive carbonate lenses. Shale is brittle and firm to very firm, carbonate is brittle and moderately cemented (drier) or weakly cemented (wetter).	shale: 5Y 4 or 5/2, carbonate: 5Y 7/2 with bright white (N) very thing <1mm veins within the carbonate matrix	n/a	%15 <1 -3 mm pebbles within the carbonate matrix	n/a	shale does not effervesce, carbonate strongly effervesces
Cr2	More continuous and distinct shale and carbonate layers	n/a	145+	n/a	Alternating 3-5 cm fracture shale and massive carbonate lenses, spacing is ~30 cm between thinner carb lenses (2-5 up to 10 cm in thickness), shale is friable to v. hard (depending on the expression of fracture texture, better expression of fracture texture is harder), carbonate is extremely weakly cemented.	shale: 5Y 5 or 6/2, carbonate: 5Y 8/1	n/a	%15 <1 -3 mm pebbles within the carbonate matrix	n/a	shale does not effervesce, carbonate strongly effervesces

*** based on this description, tentatively a Calcic Haploxeroll.**

3.2 Mineral N and anion depth patterns

Total N, ammonium (NH_4^+), and nitrate (NO_3^-) show peaks in concentration, at the surface and subsurface (Fig. 4). Concentrations peak in the A horizon (0-20 cm) and decline with depth in the solum. Total nitrogen concentration in the saprolite and unweathered bedrock is variable but shows a slight increase at 175 cm before decreasing to 250 cm. Overall, [N_{total}] are less variable than the [C_{total}] depth patterns, but [N_{total}] is the lowest when [C_{total}] is highest (c.f. Fig. 3). Both NO_3^- and NH_4^+ increase in concentration to 175 cm but below this depth [NO_3^-] peaks and sharply declines (denoted by the increasing red and decreasing blue arrows) while [NH_4^+] remains enriched to the limit of our sampling depth (denoted by the increasing red and vertical black arrows).

We compared the depth-concentration patterns of water-extracted PO_4^{-3}, NO_3^-, and Cl^- to look for evidence of NO_3^- leaching producing the accumulation at depth observed in the KCl extracted NO_3^- (Fig. 5). Phosphate, nitrate, and chloride concentrations are all enriched within the A horizon (0-20 cm). Water extractable [NO_3^-] shows similar (and expected) patterns to the KCl extracted [NO_3^-] through the pedon, including the subsurface peak around 175 cm. There is a substantial [Cl^-] spike in the A horizon but no discernable subsurface accumulation patterns through the saprolite and unweathered bedrock (denoted by the vertical black arrow). Phosphate shows highly variable concentrations through the

saprolite and unweathered bedrock, including noticeable peaks in concentration at 100 and 320 cm Noticeably, the solum between 20 and 60 cm contains no detectable [PO_4^{-3}].

3.3 Depth patterns of δ15N

The total δ15N of the pedon does not follow [N_{total}] with depth (Fig. 6). Instead, the δ15N of the pedon has two distinct isotope groupings: the solum has a mean δ15N value of 3.51 ± 0.46 ‰ and the saprolite and unweathered bedrock have a mean δ15N value of 6.04 ± 0.58 ‰. The lack of δ15N depth pattern within the solum is attributed to the significant gopher bioturbation within the upper 100 cm of the pedon (Hobbie and Ouimette, 2009).

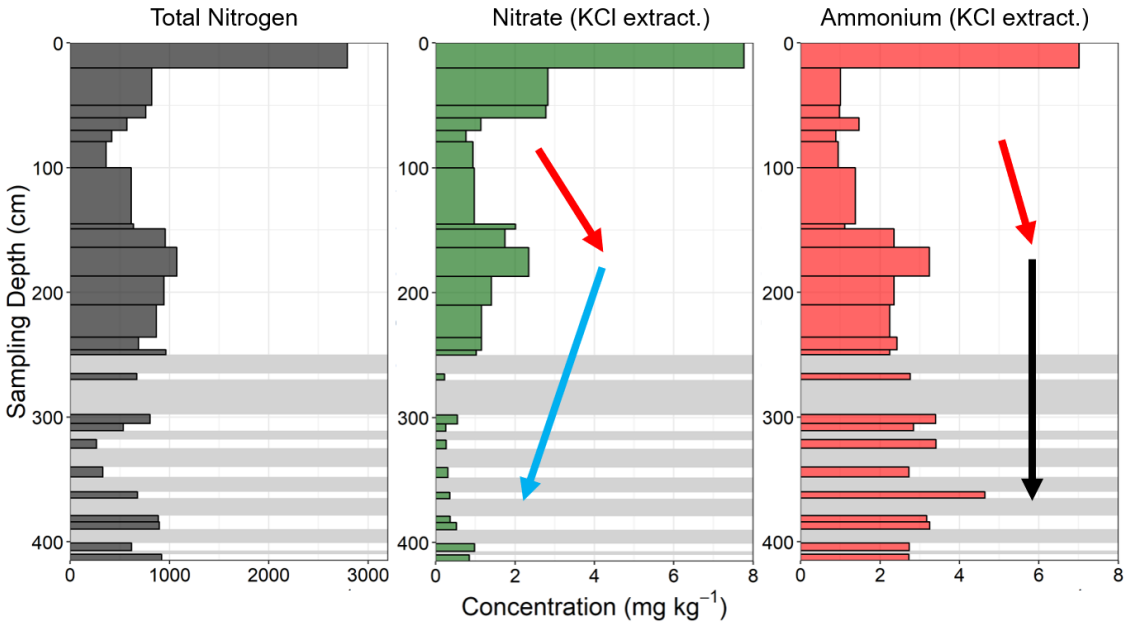

Figure 4. Depth patterns of bulk nitrogen, and KCl extractable nitrate and ammonium concentrations. Arrows indicate general depth trends: red – increase, blue – decrease, black – constant. Grey bars indicate unsampled depth ranges.

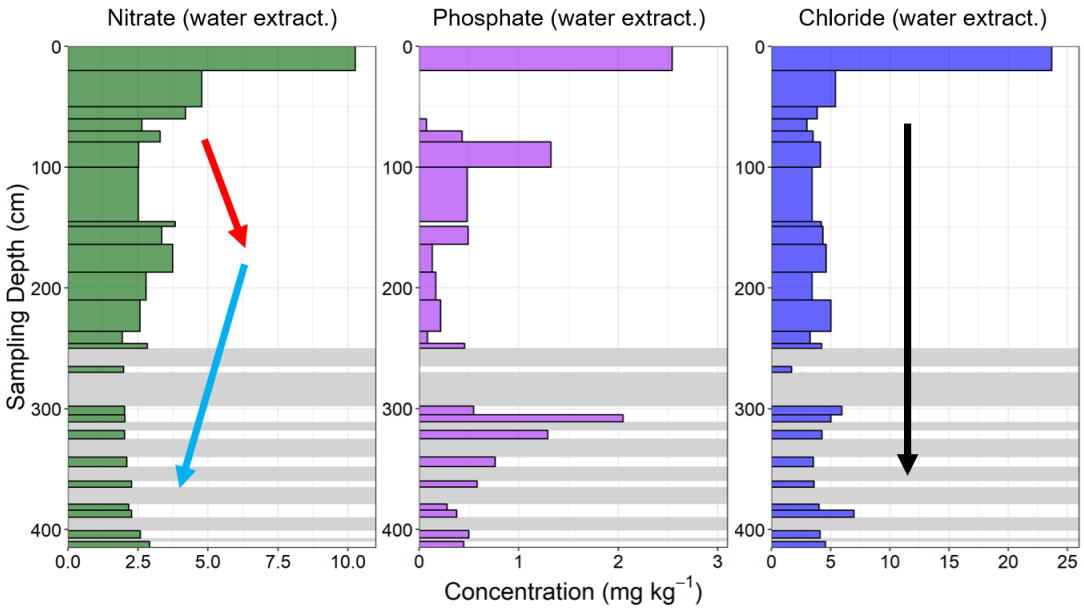

Figure 5. Concentration-depth patterns for biologically utilized anions such as nitrate and phosphate and biologically-inert anion chloride.

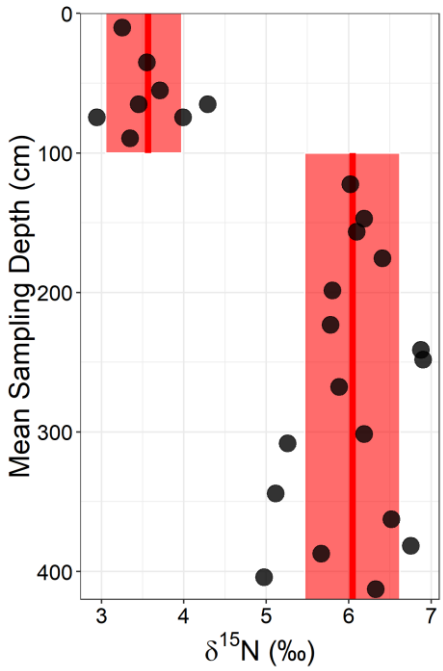

Figure 6. Total soil- δ15N depth profile. Red lines and shaded boxes indicate mean values and ± one standard deviation from the mean for the two groups of points. Points at the same depth reflect sampling of horizons where there was both shale and soil present (50-60 and 60-70).

3.4 Element concentration profiles and weathering calculations

We measured the concentration of several macro elements and evaluated their change relative to the underlying bedrock in order to better understand the role that weathering plays in releasing N into the ecosystem. Silicon and K concentrations do not show distinctive variation throughout the depth profile (Fig. 7). Excluding the surface sample, [Si] follows a similar depth profile to [N_{total}] (c.f. Fig. 4). Silicon does seems sensitive to increased [C_{inorg}] in the profile (c.f. Fig. 3), increases in [Si] correspond to increases in [C_{inorg}]. Potassium concentration does not fluctuate with [C_{inorg}]. Sodium has the highest concentrations between 0 and 50 cm and is lower but variable from 50 – 415 cm. The [P] is relatively uniform and low within the solum and higher but variable in the saprolite and rock. The peaks in [P] correspond with some of the subsurface peaks inorganic carbon (c.f. Fig. 3).

Specific element loss or gain throughout the solum (Fig. 8) is quite low (~20 % or less lost from parent material value, with P as the exception (~50% lost). Silicon is the least depleted, with just a slight depletion in concentration in the horizons with higher [C_{inorg}]. Potassium is most depleted in the Bk horizons. Phosphorus is depleted within the solum (> 35% loss in every horizon). Integrating the change in elements relative to the unweathered bedrock over the solum thickness provides a depth-average value to include in an estimate of chemical weathering flux. We use a range of elements designed to bracket an estimate of rock-derived N to this ecosystem (Table 2). Given that the parent material is an organic-rich shale, we also include an estimate of FOM-N flux adapted from Copard et al., 2007. The flux of rock-derived N to the solum is between 0.058 and 0.58 kg ha^{-1} yr^{-1} using an organic-N flux estimate and between 0.08 and 5.78 kg ha^{-1} yr^{-1} using our proxy elements for silicate-bound N.

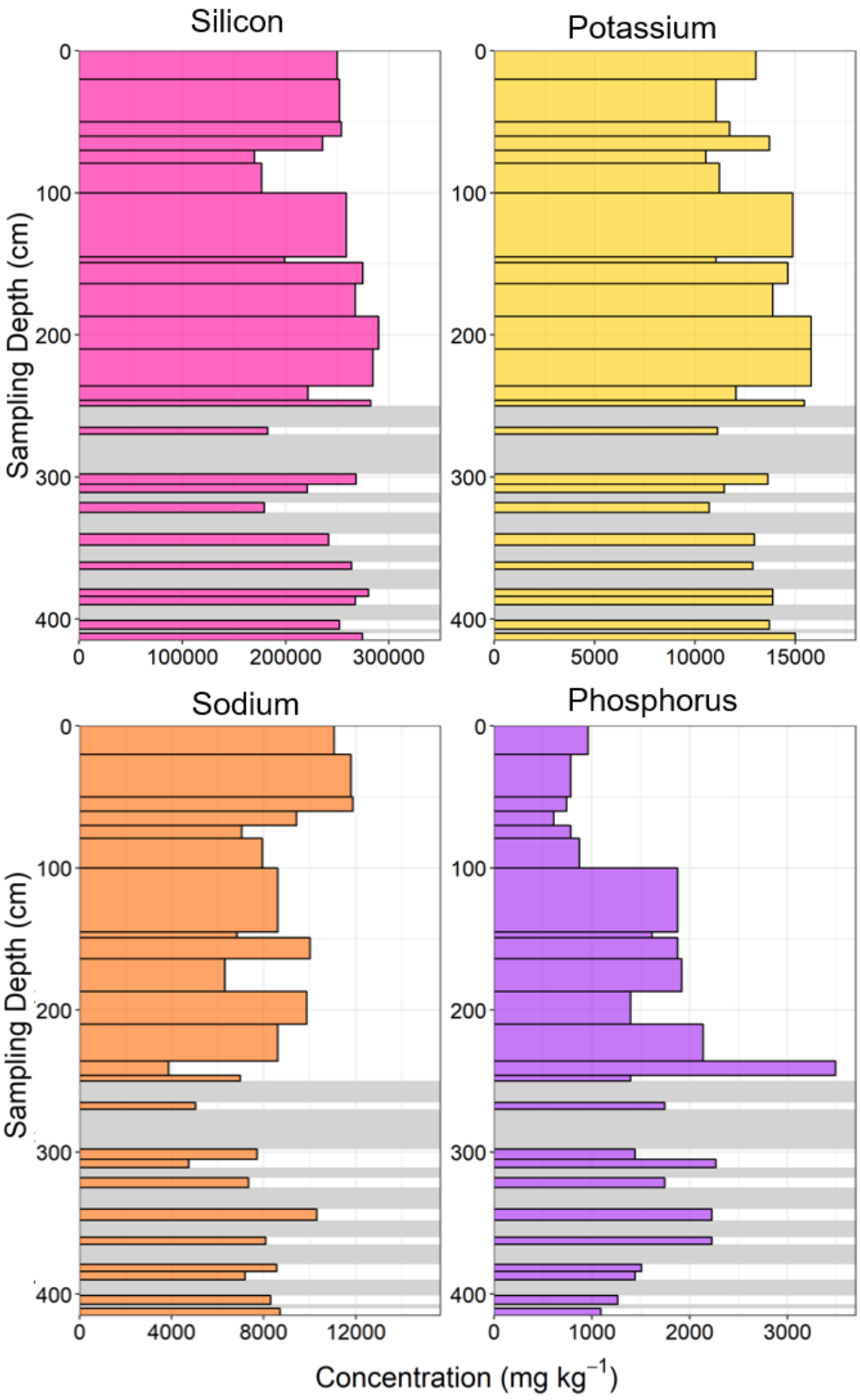

Figure 7. Concentration-depth profiles for selected elements.

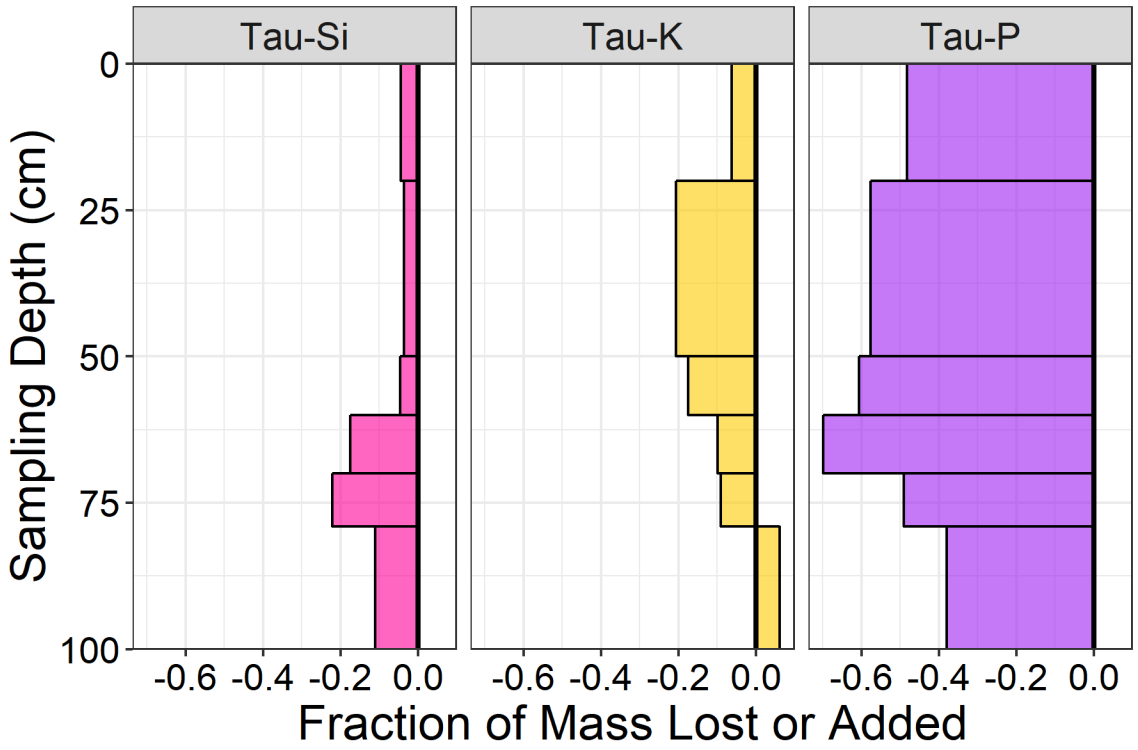

Figure 8. Tau profiles, or mass lost or added for the mobile soil for selected elements. The fraction is calculated by comparing [Ti] with a parent material value of [Ti]. A value of 0 indicates no change between parent and soil values, positive values indicate additions (+) and negative values indicate losses (-).

Table 2. Organic-N and silicate-bound N proxies for bedrock-to-mobile soil nitrogen flux. The proxy weathering fraction is the negative mobile soil integrated Tau value. N flux estimates for silicate-bound N are given for low and high erosion rate boundaries (0.082; 1.00 mm yr^{-1}).

Organic-N weathering proxy	Proxy weathering flux (kg ha^{-1} yr^{-1})	Estimated N flux (kg ha^{-1} yr^{-1})
FOM-C/N	0.10 - 1.00	0.058 - 0.58
Silicate weathering proxy	**Proxy weathering frac.**	**Estimated N flux (kg ha^{-1} yr^{-1})**
Si	0.08	0.08; 0.93
K	0.10	0.09; 1.07
P	0.52	0.47; 5.78

4 Discussion

4.1 Chemical weathering in the pedon

There is little chemical weathering throughout the pedon – the geochemical data reflecting the physical properties of the soil pit outlined in the field description for the pedon.

The element specific chemical weathering fractions showed small mass loss between the solum and the unweathered parent material (P excluded, see section 4.3). Furthermore, the solum had significant addtions of Cl and Na, especially within the A horizon. This concentration of ions within the surface horizon can be attributed to atmospheric deposition of salts to the study site (The National Atmospheric Deposition Program, 2018) and also the deposition of salts when water is drawn up from deeper horizons via evapotranspiration (Vengosh, 2003). There was also significant $CaCO_3$ accumulations within the solom starting at a shallow depth of 20 cm. These salts are accumlated in the solum because of low rates of ion leaching which we infer from the $CaCO_3$ accumulation patterns. We can interpret the presence of the $CaCO_3$ cemented horizon at 75 cm as the annual average depth of wetting – reprecipitating $CaCO_3$ dissolved in the A and B horizons as infiltrating water evaporates. The visual reddening of the horizon directly above the $CaCO_3$ cemented horizon is evidence that in years where water could infiltrate further, the BkCr3 horizon at 75 cm may be impeeding further infiltration and increasing chemical weathering in the form of iron oxidation within this horizon. The absence of mobile ion accumulations (Na^+, Cl^-) within the saprolite reinforces the idea that most infilitrating water either does not make it to 75 cm or is prevented from further infiltration because of the $CaCO_3$ cementation. Preferential flow routing via gopher burrows means some water does make it deeper than 75 cm, but only on the wettest years (Gabet Study about infilitration; Chamran et al., 2002). Water that makes it below the solum is doing some chemical weathering given our observations of the physical competancy of the saprolite compared to the unweathered bedrock. However, the [Si], [K], and [P] show little differences between the saprolite and unweathered bedrock indicating minimal chemical weathering beneath the solum. The geochemical data and physical

description of the pedon both point towards the pedon functioning as a weathering-limited system.

4.2 Nitrogen dynamics within the pedon

4.2.1 Depth patterns N

Depth-concentration profiles of N indicate distinct pools within the pedon. We interpret the concentration peak in total and mineral forms of N in the A horizon as representing N derived from atmospheric deposition and N fixation, as well as N that is recycled by decomposition of organic matter. The large pool of total N in the saprolite and unweathered bedrock (depth average value of 773.55 mg kg^{-1}) does not correlate with equally large pools of organic C as is seen in the solum. Additionally, [NO_3^-] declines in the unweathered bedrock while [NH_4^+] is relatively high and constant indicating NH_4^+ as the favored mineral form of N within the unweathered bedrock. It is difficult to argue for substantial illuviation of NH_4^+ the difference in N isotope values between solum and rock. As a consequence, we argue that the unweathered bedrock and saprolite contain substantial N that is either being released directly as NH_4^+ or is being mineralized from rock-derived organic matter.

4.2.2 Conversion of saprolite NH4+ to NO3-

Mineral N depth patterns in conjunction with anion data provide a look into potential pathways for the release of rock-derived N. The decline in [NH_4^+] toward the surface associated with the peak in [NO_3^-] within the saprolite could be from nitrification of the NH_4^+, however NO_3^- mobility from the surface is also a plausible explanation. Our isotope data imply that illuviation of N from the surface is unlikely (this would result in lighter δ15N signature between 150 and 200 cm). However, we use Cl^- as conservative tracer as a further test for illuviation within the profile. Studies in semi-arid climates have shown that nitrate

can also be mobilized from the top soil and accumulated when the water carrying it dries up (Walvoord et al., 2003). This process leads to subsurface accumulations of NO_3^- corresponding to similar-depth subsurface peaks in the biologically-inert Cl^-. The uniform and lower Cl^- concentrations in our soil depth profile indicates a small amount of chloride is making its way through the profile, however there is no subsurface accumulation to imply mobilization and re-accumulation between 150-200 cm. Minimal anion mobilization is reinforced by the presence of an infiltration-hindering $CaCO_3$ cemented horizon within the solum and the surface accumulations of Cl^-. Therefore, we attribute the $[NO_3^-]$ peak in the saprolite to nitrification of NH_4^+ from the rock, identifying a conduit for the eventual introduction of rock-derived N to the solum.

4.3 Concentration patterns of P inform N dynamics

Bedrock as the single source of P to the pedon means depth patterns of total [P] and $[PO_4^{-3}]$ provide important context for interpreting N dynamics. The surface enrichment of PO_4^{-3} indicates biocycling – a surface-proximal recycling of essential, but sparse nutrients by plants (Jobbágy and Jackson, 2004). The tight bio-cycling of P is to be expected given the depletion of P in the mobile soil shown by [P] depth profile and the P-specific weathering fraction (Fig. 8 & Table 2). The low chemical weathering in the solum may be limiting the introduction of fresh P-carrying minerals to the soil. The slow rates of P introduction coupled with particulate loss of P via gopher-driven soil disturbance (Gabet et al., 2005) and loss of Oak-biomass associated P during the decline in Oak density in last two centuries (Whipple et al., 2011) may intensify the depletion of P within the solum compared to other elements and drive tighter biocycling. Nitrate does not show the same biocycling dynamics as P, perhaps due to multiple sources of N to the mobile soil for the nutrient (N-rich bedrock and large

surface contributions of the element). Whereas bedrock weathering is the only source of P to the ecosystem, N entering via bedrock-weathering is supplemented by N coming in from the surface.

4.4 N flux estimates compared to atmospheric sources and other ecosystems

Surficial inputs of N are the dominant source of N for our study site. The range of rock-derived N flux estimates is 0.06 to 5.78 kg ha^{-1} yr^{-1}, with most estimates between 0.47 and 1.07 kg ha^{-1} yr^{-1}. Previously discussed P dynamics and sourcing make the high end of this range (5.78 kg ha^{-1} yr^{-1}) less likely for nitrogen and we will exclude this flux estimate from further calculations. Atmospheric deposition for the region, including ammonia and nitric- compounds is estimated to be 6.04 kg ha^{-1} yr^{-1} by the National Atmospheric Deposition Program (2019) and validated by Fenn et al (2003) who suggested a rate of ~6 kg ha^{-1} yr^{-1} for the region. Terrestrial biological nitrogen fixation for grassland ecosystems is spatially and temporally heterogenous (Jones and Woodmansee, 1979), however previous work has used a range of 0.9-3.1 kg ha^{-1} yr^{-1} to approximate yearly average fixation rates for grassland ecosystems (Brenner et al., 2001; Cleveland et al., 1999). These estimates of biological nitrogen fixation and anthropogenically produced nitrogen deposition sum to produce a range of surface additions between 6.97 and 9.17 kg ha^{-1} yr^{-1}. Our flux estimates of rock-derived N are between less than a percent and 15 percent of the total surficial inputs estimated from the area; the higher end of this estimate is a small but significant contribution to the total N budget.

The low rock-derived N flux estimates for this study site are attributed to the weathering-limited conditions set by the semi-arid climate. Excluding the high P-derived flux estimate, the range of fluxes in this study are lower than those from a forested ecosystem

forming on nitrogen-rich mica schist in Northern California (NCA). Rock-derived N studies from forested ecosystems in NCA found chemical weathering fractions for K, Na_2O, and N (N was derived from a silicate-N targeted extraction) were between 22% and 48% across three different study sites, these weathering fractions are much higher than our chemical weathering fractions for K and Si (8% and 9% respectively). Accordingly, the rock-derived N fluxes from NCA are higher: 1.6-10.7 kg ha^{-1} yr^{-1} (Morford et al., 2016b), and 3.0-10.9 kg ha^{-1} yr^{-1} (Morford et al., 2011). Northern California receives more than twice as much annual precipitation than Sedgwick (~1000 mm vs 380 mm). The increased precipitation produces an increase in chemical weathering as observed from the chemical weathering fractions at those study sites which in turn increases the flux of rock-derived N to the ecosystem. Despite an N-rich bedrock and higher potential total denudation rates, the lower rainfall at Sedgwick seems to be limiting the flux of rock-derived N to the ecosystem.

4.5 Predicting total N and total δ15N with the N-flux estimates

The distinct and uniform difference between total δ15N values in the solum, and the saprolite and unweathered bedrock provide a fingerprint for tracing rock-derived N through the pedon, which allows us to check our rock-derived N flux estimates. Given the large concentration of N in the saprolite and unweathered bedrock not associated with surficial organic matter inputs and the lack of evidence for significant N mobility out of the solum from the anion data, we interpret the δ15N values below 100 cm as a rock-derived nitrogen signature. Bioturbation by gophers homogenizes the δ15N signature within the solum and as a consequence the δ15N values represent a mixture of surface input-derived N and rock-derived N. If the N cycling within an ecosystem is assumed to be within steady state (the reality for soil ages and residence times of over few thousand years – Brenner et al., 2001),

then it's been shown that the total N concentration within the soil can be approximated by the sum of the inputs divided by a rate constant for N losses (Eqn. S3 – 1a, b, Amundsen and Baisden, 2000; Brenner et al., 2001). In the same manner, the soil δ15N can be approximated by the weighted sum of the N inputs divided by a fractionation constant for total losses (Eqn. S3 - 2).

The simple concentration and isotope model can be used to check our estimated rock-derived N fluxes; parameterizing the equations with concentration and δ15N values for the solum, and the flux rate of rock-derived N and bedrock δ15N signatures for our soil pit, and estimates of surface input N concentrations and δ15N signatures. We use data from a Mediterranean annual grassland ecosystem in the Central Valley of California with a similar MAT and MAP which provides comparable parameters for the model when inputs are absent (estimates of nitrogen residence time (k_{ex}) and nitrogen loss fractionation values (α_{ex}) (Brenner et al., 2001). Rock-derived N fluxes between 0.58 to 1.07 kg ha^{-1} yr^{-1} can predict the study site's solum [N] and δ15N signature (Table 3; see also S3-Table 1). A caveat to this estimate is that atmospheric deposition of nitrogen can have a temporally and spatially varied δ15N (Heaton, 1986), and our best fit model results require the average signature of atmospheric deposition to have a positive per mil signature. This study's utilization of δ15N as a tracer for rock-derived N within the solum are unique to rock-derived N research thus far. Previous work tracking rock-derived N through the ecosystem utilized average values of δ15N for the soil, rock, and plants to track plant utilization of the rock-derived N within a montane ecosystem. However, this study lacked depth resolution of δ15N within the soil and bedrock to apply as a tracer for rock-derived nitrogen within the solum (Morford et al.,

2011). The simple model results indicate that a rock-derived N flux between 0.58 and 1.07 kg ha^{-1} yr^{-1} is realistic for our study site.

Table 3. Best model fits for nitrogen concentration and δ15N signature of the mobile soil. Parameters are either sourced from previous work or come from this study. Target [N_{total}] and δ15N or our soil pit are 16,683.03 kg ha^{-1} and 3.52‰ respectively.

Atmospheric Deposition[a] (kg ha^{-1} yr^{-1})	δ15N Atm. Dep.[b] (‰)	N Fix.[c] (kg ha^{-1} yr^{-1})	δ15N Fix. (‰)	Rock-derived N (kg ha^{-1} yr^{-1})	δ15N Rock (‰)	Total N Inputs (kg ha^{-1} yr^{-1})	modeled δ15N soil, *α_{ex} = 0.9905, -5 ‰	modeled total N for 1-m soil (kg ha^{-1}) *k_{ex} = 0.000615
6.07	5	3.1	0	0.58	6.04	9.75	3.48	15856.15
6.07	5	3.1	0	0.93	6.04	10.10	3.57	16425.26
6.07	5	3.1	0	1.07	6.04	10.24	3.61	16652.90

[a] National Atmospheric Deposition Program, 2018
[b, c] Brenner et al., 2001; Heaton, 1987; Garten, 1992; Hoering, 1957

5 Conclusions

The inclusion of N as a rock-derived nutrient requires analyses that span from the surface down to the bedrock. Currently, these rock-derived N targeted pedon-scale analyses only exist for a narrow set of climate, lithologic, and tectonic regimes and diversifying the sets of soil forming factors is necessary for establishing rock-derived N within pedon to catchment-scale ecological studies. This study examines N dynamics within a soil derived from nitrogen-rich shale within a semi-arid, Mediterranean grassland – adding a water-limited endmember to existing pedon-scale, rock-derived N research. We find distinct pools of N within the solum, and the underlying saprolite and unweathered bedrock. Furthermore, we show convergent evidence for the conversion of bedrock derived NH_4^+ to NO_3^- within the saprolite as a pathway for rock-derived N introduction into the ecosystem. Rock-derived N flux for the study site is between 0.58 and 1.07 kg ha^{-1} yr^{-1} as determined by proxies for silicate- and organic-N and verified by a simple isotope-driven mixing model. The rock-derived N flux is low despite high estimates of total denudation because of the chemical

weathering limited conditions set by the semi-arid environment. Additionally, large contributions of N from wet and dry atmospheric deposition dwarf contributions of rock-derived N within this study-site. This work shows evidence for rock-derived N utilization within the pedon but a diminished importance of rock-derived N for the total N budget compared to wetter and more remote ecosystems.

6 Acknowledgments

This work was funded by the NSF-EAR grant no. 1411309, “Bedrock nitrogen and the Earth system: From geobiological mechanisms to climate change forecasts.”

References

Amundson, R., & Baisden, W. T. (2000). Stable isotope tracers and mathematical models in soil organic matter studies. In Methods in Ecosystem Science (pp. 117-137). Springer, New York, NY.

Brenner, D. L., Amundson, R., Baisden, W. T., Kendall, C., & Harden, J. (2001). Soil N and 15N variation with time in a California annual grassland ecosystem. Geochimica et Cosmochimica acta, 65(22), 4171-4186.

Brimhall, G. H., & Dietrich, W. E. (1987). Constitutive mass balance relations between chemical composition, volume, density, porosity, and strain in metasomatic hydrochemical systems: results on weathering and pedogenesis. Geochimica et Cosmochimica Acta, 51(3), 567-587.

Chadwick, O. A., Gavenda, R. T., Kelly, E. F., Ziegler, K., Olson, C. G., Elliott, W. C., & Hendricks, D. M. (2003). The impact of climate on the biogeochemical functioning of volcanic soils. Chemical Geology, 202(3-4), 195-223.

Chamran, F., Gessler, P. E., & Chadwick, O. A. (2002). Spatially explicit treatment of soil-water dynamics along a semiarid catena. Soil Science Society of America Journal, 66(5), 1571-1583.

Chow, J. C., Watson, J. G., Lowenthal, D. H., & Countess, R. J. (1996). Sources and chemistry of PM10 aerosol in Santa Barbara County, CA. Atmospheric Environment, 30(9), 1489-1499.

Cleveland, C. C., Townsend, A. R., Schimel, D. S., Fisher, H., Howarth, R. W., Hedin, L. O., ... & Wasson, M. F. (1999). Global patterns of terrestrial biological nitrogen (N2) fixation in natural ecosystems. Global biogeochemical cycles, 13(2), 623-645.

Copard, Y., Amiotte-Suchet, P., & Di-Giovanni, C. (2007). Storage and release of fossil organic carbon related to weathering of sedimentary rocks. Earth and Planetary Science Letters, 258(1-2), 345-357.

Craine, J. M., Brookshire, E. N. J., Cramer, M. D., Hasselquist, N. J., Koba, K., Marin-Spiotta, E., & Wang, L. (2015). Ecological interpretations of nitrogen isotope ratios of terrestrial plants and soils. Plant and Soil, 396(1-2), 1-26.

Dibblee, T. W. (1966). Geology of the central Santa Ynez Mountains, Santa Barbara County, California (Vol. 186). California Division of Mines and Geology.

Fenn, M. E., Baron, J. S., Allen, E. B., Rueth, H. M., Nydick, K. R., Geiser, L., ... & Neitlich, P. (2003). Ecological effects of nitrogen deposition in the western United States. BioScience, 53(4), 404-420.

Gabet, E. J., Fierer, N., & Chadwick, O. A. (2005). Prediction of sediment-bound nutrient delivery from semi-arid California watersheds. Journal of Geophysical Research: Biogeosciences, 110(G2).

Garten Jr, C. T. (1992). Nitrogen isotope composition of ammonium and nitrate in bulk precipitation and forest throughfall. International Journal of Environmental Analytical Chemistry, 47(1), 33-45.

Haston, L., & Michaelsen, J. (1994). Long-term central coastal California precipitation variability and relationships to El Niño-Southern Oscillation. Journal of Climate, 7(9), 1373-1387.

Haynes, R. J. R. J. (2012). Mineral nitrogen in the plant-soil system. Elsevier.

Heaton, T. H. (1986). Isotopic studies of nitrogen pollution in the hydrosphere and atmosphere: a review. Chemical Geology: Isotope Geoscience Section, 59, 87-102.

Heckman, K., & Rasmussen, C. (2011). Lithologic controls on regolith weathering and mass flux in forested ecosystems of the southwestern USA. Geoderma, 164(3-4), 99-111.

Heimsath, A. M., Dietrich, W. E., Nishiizumi, K., & Finkel, R. C. (1997). The soil production function and landscape equilibrium. Nature, 388(6640), 358.

Hobbie, E. A., & Ouimette, A. P. (2009). Controls of nitrogen isotope patterns in soil profiles. Biogeochemistry, 95(2-3), 355-371.

Hoering, T. (1957). The isotopic composition of the ammonia and the nitrate ion in rain. Geochimica et Cosmochimica Acta, 12(1-2), 97-102.

Holloway, J. M., & Dahlgren, R. A. (2002). Nitrogen in rock: occurrences and biogeochemical implications. Global Biogeochemical Cycles, 16(4).

Homyak, P. M., Blankinship, J. C., Marchus, K., Lucero, D. M., Sickman, J. O., & Schimel, J. P. (2016). Aridity and plant uptake interact to make dryland soils hotspots for nitric oxide (NO) emissions. Proceedings of the National Academy of Sciences, 113(19), E2608-E2616.

Hood-Nowotny, R., Umana, N. H. N., Inselbacher, E., Oswald-Lachouani, P., & Wanek, W. (2010). Alternative methods for measuring inorganic, organic, and total dissolved nitrogen in soil. Soil Science Society of America Journal, 74(3), 1018-1027.

Houlton, B. Z., Morford, S. L., & Dahlgren, R. A. (2018). Convergent evidence for widespread rock nitrogen sources in Earth's surface environment. Science, 360(6384), 58-62.

Jobbágy, E. G., & Jackson, R. B. (2004). The uplift of soil nutrients by plants: biogeochemical consequences across scales. Ecology, 85(9), 2380-2389.

Jones, M. B., & Woodmansee, R. G. (1979). Biogeochemical cycling in annual grassland ecosystems. The Botanical Review, 45(2), 111-144.

Juster, J. T., Brown, P. E., & Bailey, S. W. (1987). NH4-bearing illite in very low grade metamorphic rocks associated with coal, northeastern Pennsylvania. American Mineralogist;(USA), 72.

Lin, Y., Prentice III, S. E., Tran, T., Bingham, N. L., King, J. Y., & Chadwick, O. A. (2016). Modeling deep soil properties on California grassland hillslopes using LiDAR digital elevation models. Geoderma regional, 7(1), 67-75.

Morford, S. L., Houlton, B. Z., & Dahlgren, R. A. (2011). Increased forest ecosystem carbon and nitrogen storage from nitrogen rich bedrock. Nature, 477(7362), 78.

Morford, S. L., Houlton, B. Z., & Dahlgren, R. A. (2016a). Geochemical and tectonic uplift controls on rock nitrogen inputs across terrestrial ecosystems. Global Biogeochemical Cycles, 30(2), 333-349.

Morford, S. L., Houlton, B. Z., & Dahlgren, R. A. (2016b). Direct quantification of long-term rock nitrogen inputs to temperate forest ecosystems. Ecology, 97(1), 54-64.

National Atmospheric Deposition Program (NRSP-3). 2019. NADP Program Office, Wisconsin State Laboratory of Hygiene, 465 Henry Mall, Madison, WI 53706.

Riebe, C. S., Kirchner, J. W., & Finkel, R. C. (2003). Long-term rates of chemical weathering and physical erosion from cosmogenic nuclides and geochemical mass balance. Geochimica et Cosmochimica Acta, 67(22), 4411-4427.

Scherer, H. W., Werner, W., & Rossbach, J. (1992). Effects of pretreatment of soil samples on N mineralization in incubation experiments. Biology and fertility of soils, 14(2), 135-139.

Schwinning, S. (2010). The ecohydrology of roots in rocks. Ecohydrology: Ecosystems, Land and Water Process Interactions, Ecohydrogeomorphology, 3(2), 238-245.

Sigman, D. M., Casciotti, K. L., Andreani, M., Barford, C., Galanter, M. B. J. K., & Böhlke, J. K. (2001). A bacterial method for the nitrogen isotopic analysis of nitrate in seawater and freshwater. Analytical chemistry, 73(17), 4145-4153.

Soil Survey Staff, Natural Resources Conservation Service, United States Department of Agriculture. Web Soil Survey. Available online at the following link: https://websoilsurvey.sc.egov.usda.gov/. Accessed [03/7/2019].

Vengosh, A. (2003). Salinization and saline environments. Treatise on geochemistry.

Vitousek, P. M., Porder, S., Houlton, B. Z., & Chadwick, O. A. (2010). Terrestrial phosphorus limitation: mechanisms, implications, and nitrogen–phosphorus interactions. Ecological applications, 20(1), 5-15.

Walvoord, M. A., Phillips, F. M., Stonestrom, D. A., Evans, R. D., Hartsough, P. C., Newman, B. D., & Striegl, R. G. (2003). A reservoir of nitrate beneath desert soils. Science, 302(5647), 1021-1024.

West, A. J., Galy, A., & Bickle, M. (2005). Tectonic and climatic controls on silicate weathering. Earth and Planetary Science Letters, 235(1-2), 211-228.

Whipple, A. A., Grossinger, R. M., & Davis, F. W. (2011). Shifting baselines in a California oak savanna: nineteenth century data to inform restoration scenarios. Restoration Ecology, 19(101), 88-101.

Yoo, K., Mudd, S. M., Sanderman, J., Amundson, R., & Blum, A. (2009). Spatial patterns and controls of soil chemical weathering rates along a transient hillslope. *Earth and Planetary Science Letters*, 288(1-2), 184-193.

Chapter 5 - Supplemental Material

S1. Choosing a soil production rate

This is discussed in detail within Chapter 3 of the dissertation.

S2. Evaluating index elements for chemical weathering calculations

Mass balance that accounts for volume change within a profile can be utilized to evaluate loss or gain within a soil profile during weathering (Brimhall and Dietrich, 1987; Chadwick et al., 1990). Index elements, that are assumed immobile during chemical weathering, are used to account for volume change via a metric called strain. The complicating factor is that "immobile" elements are rarely actually immobile (Kurtz et al., 2000; Jin et al., 2010) – elements such as Ti, Zr, and Nb are often used due low solubility, but these elements can be mobilized during weathering as part of soil colloids or organic matter complexes (Sudom and Arnaug, 1971; Thompson et al., 2006). Work by Bern et al (2015) describes a mass balance model that explicitly accounts for colloidal movement of these index elements, however given the water-limited weathering system at Sedgwick Reserve we expect minimal redistribution of these elements. We instead compare concentration (Fig. 1), strain and chemical depletion factors (Fig. 2), and tau profiles (Fig. 3) from several high field strength elements to assess which will be used as an index element for profile mass balance calculations.

Bulk density, the ratio of mass to the volume for a ped, is essential to the calculations of strain and tau. Weathering calculations in the following sections are only for samples between 0 and 250 cm, the range for which measured bulk density exists. Bulk density for sampled horizons between 0 and 250 cm was determined via clod method (Burt, 2004). Peds

were oven-dried overnight at 40^{o}C before being weighed to determine mass at a controlled moisture content. Weighed peds were dipped in liquid saran and let to dry. Volume was estimated by submerging the coated peds and measuring displaced water. Five clods per horizon were measured to produce an average bulk density with a standard deviation to assess spread in data. The soil (0-100 cm) mean bulk density was slightly higher than the rock (100-250 cm), 1.85 g cm^{-3} and 1.73 g cm^{-3} respectively. We attribute the differences in bulk density to the variation in parent material composition, between slightly denser shale and less dense lightly cemented carbonate layers.

Table S2-3. Average and standard deviation for bulk density of the regolith.

Sample Depth (cm)	Mean* D_b (g cm^{-3})	Std.* D_b (g cm^{-3})
0-20	1.71	0.16
20-50	2.10	0.21
50-60	1.59	0.11
60-70	1.67	0.21
70-79	1.83	0.08
79-100	1.88	0.20
100-145	1.80	0.10
145-149	1.50	0.13
149-164	1.63	0.06
164-187	1.62	0.14
187-210	1.67	0.17
210-236	1.70	0.13
236-246	1.85	0.20
246-250	2.47	0.27
* Mean and standard deviation D_b were calculated on n=5 for each horizon		

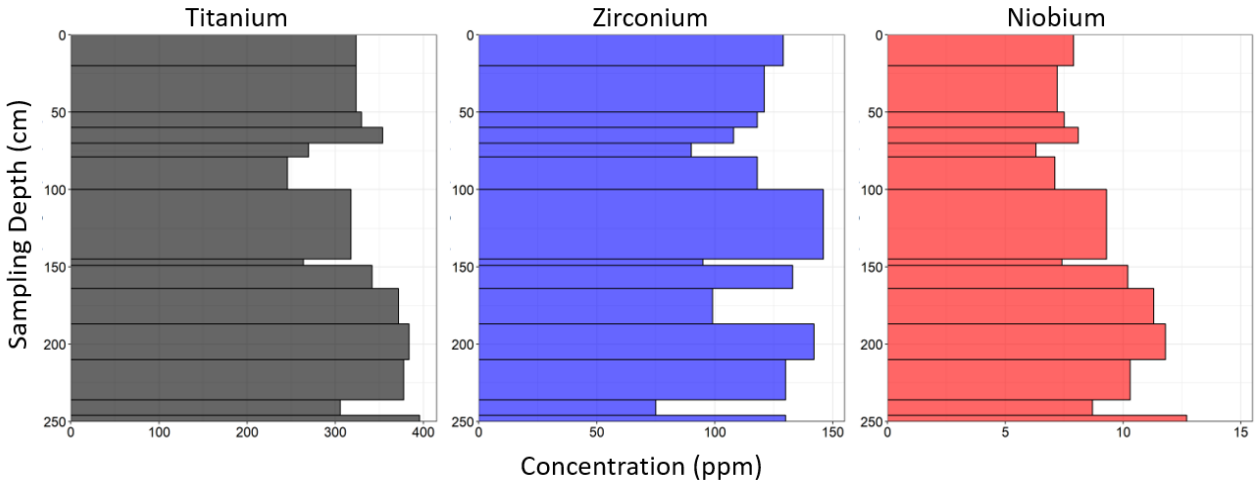

Figure S2-3. Concentration-depth profiles of 3 potential index elements

Chemical concentrations, non-normalized, are subject changes based on the concentrations of other elements within the sample – much higher concentrations of other elements might push the concentration of the element in question down or vice versa. However, comparisons between concentration profiles can give insight into chemical dynamics. A major driver in changes of chemical concentration between horizons in this profile is the presence of carbonates. A significantly increased calcium concentration can

drive down the concentrations of other elements. Calcium carbonate increases seem to be driving down titanium concentrations (Fig. 1) – lows in Ti concentration align with highs in Ca and inorganic C concentrations. This affect is also present for Zr concentrations however they seems to be additional factors influencing the Zr pattern. From the concentrations, we see that there is a loss of niobium compared to the parent material – this pattern could be a weathering related loss or it could be the artefact of Nb-depleted atmospheric additions – but either way it is a concerning pattern an "immobile" element. Both zirconium and niobium are present in trace element quantities within the soil, which mean the concentration within a sample is more likely to be subject to slight variations than elements present in higher concentrations.

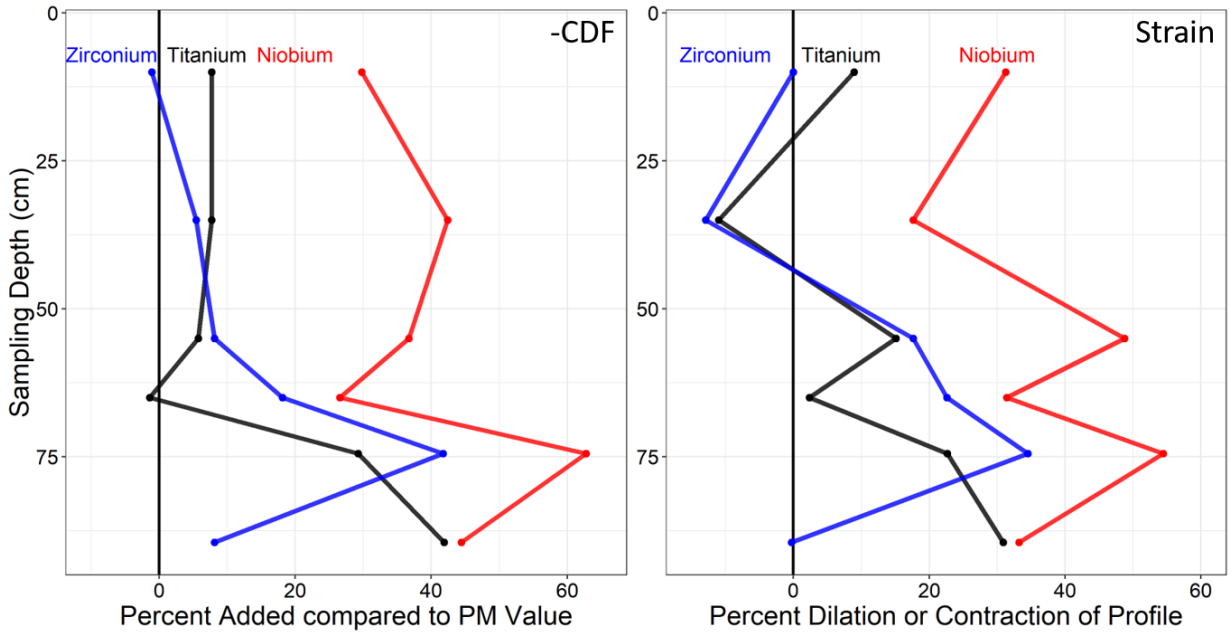

Figure S2-4. left. The negative chemical depletion fraction, -CDF, calculated using Zr, Ti, and Nb as index elements. right. Profile expansion or collapse calculated as measured by strain, ε, calculated using Zr, Ti, and Nb as index elements.

Here we examine how two metrics of assessing total losses or additions to the profile are changed by the index element used for calculation (Fig 2). The chemical depletion

fraction, CDF, was termed in part because of its use is conjunction with total denudation rates to assess the fraction of total weathering that is attributed to chemical weathering (see application within the main text). By assuming the index element is immobile within the profile, increases or decreases to the concentration of the index element are only produced by the loss or addition of other elements within the soil and therefore the change is attributed as total element losses or gains for the profile. In the case of arid climates, where chemical weathering losses are minimal, the CDF may be negative. For ease of interpretation between strain and CDF, figure 2 shows the negative CDF such that positive values represent additions. Profile strain, ε, is a similar metric but also includes the bulk density of the soil and parent material. Bulk density is subject to change via soil compaction, texture changes, organic matter additions, etc. (Brady and Weil, 1990). We see that niobium as an index element indicates more additions for both strain and CDF than Ti and Zr. In contrast, Ti and Zr from 0-50 are similar and show minimal additions and losses, but have diverging patterns in horizons with more calcium carbonate accumulation within them (50-100 cm). Zirconium-indexed CDF and strain indicates minimal additions in the bottom soil horizon – a horizon which has almost the same amount of inorganic carbon as the horizon above it and much more inorganic carbon that the horizon at 65 cm (where Zr is indicating more weathering). Titanium-indexed CDF tracks closely with the additions of carbonates, showing profile inflation (ε) or mass additions (-CDF) in carbonate rich layers.

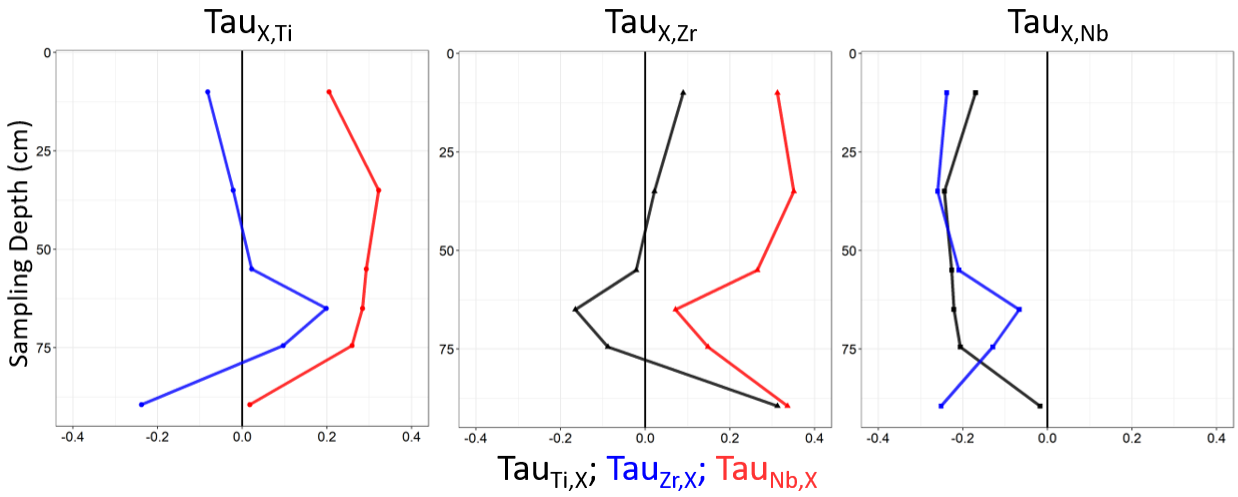

Figure S2-5. Mass transfer coefficients, Tau, for Ti, Zr, and Nb, using Ti, Zr, or Nb as the index element.

Lastly, by treating a potential index element as a mobile element, we can calculate the mass transfer coefficient (Tau) to assess the relative mobility of that index element with respect to the other two index elements. This technique also sheds light on how the addition or depletion of an index element will affect the tau calculations for other mobile elements – ie: niobium's depletion produces more enriched tau profiles for Ti and Zr. The uniform depletion of niobium with respect to the parent material using Ti and Zr as an index element suggests that Nb would be a bad element to use as an index element (mobile where it should not be mobile). Zirconium and titanium are both relatively immobile, however the slight enrichment of Zr (89 cm) in some carbonate horizons but depletion (75 cm) in others is worrying as the pattern is not easily explainable and could indicate mobility of Zr within the profile.

Given the potential mobility of Zr and the uniform depletion of Nb, this study will use Ti as an index element. The concentration of Ti is significantly more than Zr and Nb within the soil, therefore we presume that the element is less sensitive to heterogeneities within the soil horizons. Furthermore, the Tau of Ti, using Zr as an index element shows relative

immobility. The horizons which show the most mobility within Ti are calcium carbonate enriched horizons – here Ti is depleted. The depletion of Ti will produced slightly more enriched profiles in elements that do not see concentration declines in carbonate rich horizons (see $Tau_{Ti,Zr}$ for 89 cm). If elements do see depletions in carbonate rich horizons, the depletion of Ti will dampen the Tau signal, showing less depletion than is likely occurring (see $Tau_{Ti,Nb}$).

S3. Nitrogen isotope mixing model

This work utilized a simple black box model described in Brenner et al. (2001) to check our rock-derived nitrogen fluxes. The model states that at steady state (nitrogen in = nitrogen out), the stored total nitrogen in the soil (N_{bulk}; kg m^{-2}) is equal to the sum of the inputs (N_{atm}, N_{fix}; kg m^{-2} yr^{-1}) divided by a rate constant for the outputs (k_{ex}; yr^{-1}) (Eqn. S3 – 1a). We've modified the equation to add rock-derived nitrogen, N_{rock}, as an input, which functions similarly to N_{atm} in the model (Eqn. S3 – 1b.).

Equation S3 – 1a $$N_{bulk} = \frac{N_{atm}+N_{fix}}{k_{ex}}$$

Equation S3 – 1b $$N_{bulk} = \frac{N_{atm}+N_{fix}+N_{rock}}{k_{ex}}$$

Brenner et al. (2001) designated that the corresponding δ15N signature of the bulk soil at nitrogen-steady-state was described as the sum of the flux-proportional fractions of δ15N from each input ($\underline{R}_{inputs}$) divided by a fractionation factor (α_{ex}) which accounts for the change in δ15N when soil N is transferred out of the soil reservoir. For our soil this is represented by Eqn. S3 – 2.

Equation S3 – 2a $$R_{bulk} = \frac{\underline{R}_{inputs}}{\alpha_{ex}}$$

We utilized data from the 4-40kyr terraces (brackets the approximate residence time for our ridgecrest-located soil) studied in Brenner et al. (2001) to supply values for the loss rate constant and fractionation factors. Literature from previous studies on fixation in California grasslands provides an estimate of nitrogen fixation inputs (Jones and Woodmansee, 1979; Cleveland et al., 1999; Brenner et al., 2001). Nitrogen deposition for the 30 km^2 grid cell containing our study site was sourced from the National Atmospheric Deposition Program (2019). Lastly, we used the same range of δ15N signatures of atmospheric deposition as Brenner et al. (2001), which sourced their values from Hoering (1957), Heaton (1987), and Garten (1992). Using equations S3-1b and S3-2, we solved for total nitrogen concentration in the 1-m soil profile and the δ15N-bulk nitrogen value and compared our modeled estimates against the total N concentration in the 1-m profile (16,683 kg ha^{-1} using a soil bulk density of 1.73 g cm^{-3}) and the average δ15N-bulk nitrogen value (3.53 ‰). The results of our estimates are in Table S3-1.

Table S3-4. Soil nitrogen concentration and isotope mixing model inputs and results.

Atm. Dep. (kg ha^{-1} yr^{-1})	δ15N Atm. Dep (‰)	Fix. (kg ha^{-1} yr^{-1})	δ15N Fix. (‰)	δ15N Rock (‰)	Rock-N (kg ha^{-1} yr^{-1})	Total N Inputs (kg ha^{-1} yr^{-1})	Atm. Dep. Frac	Fix. Frac	Rock-N Frac	modeled δ15N soil, α_{ex} = 0.9905, -5‰	modeled δ15N soil, α_{ex} =0.9965, 0‰	modeled total N for soil (kg ha^{-1}) k_{ex} = 0.000363	modeled total N for soil (kg ha^{-1}) k_{ex} = 0.000615	modeled total N for soil (kg ha^{-1}) k_{ex} = 0.00147	modeled total N for soil (kg ha^{-1}) k_{ex} = 0.00198
6.07	-5	0.9	0	6.04	0.06	7.03	0.86	0.13	0.01	-4.31	-4.28	19370.61	11433.39	4783.36	3551.28
6.07	5	0.9	0	6.04	0.06	7.03	0.86	0.13	0.01	4.41	4.38	19370.61	11433.39	4783.36	3551.28
6.07	-5	0.9	0	6.04	0.58	7.55	0.80	0.12	0.08	-3.59	-3.57	20803.12	12278.92	5137.10	3813.91
6.07	5	0.9	0	6.04	0.58	7.55	0.80	0.12	0.08	4.53	4.50	20803.12	12278.92	5137.10	3813.91
6.07	-5	0.9	0	6.04	0.93	7.90	0.77	0.11	0.12	-3.16	-3.14	21767.31	12848.02	5375.19	3990.67
6.07	5	0.9	0	6.04	0.93	7.90	0.77	0.11	0.12	4.60	4.57	21767.31	12848.02	5375.19	3990.67
6.07	-5	0.9	0	6.04	1.07	8.04	0.76	0.11	0.13	-3.00	-2.98	22152.98	13075.66	5470.43	4061.38
6.07	5	0.9	0	6.04	1.07	8.04	0.76	0.11	0.13	4.62	4.59	22152.98	13075.66	5470.43	4061.38
6.07	-5	3.1	0	6.04	0.06	9.23	0.66	0.34	0.01	-3.28	-3.26	25431.22	15010.62	6279.95	4662.39
6.07	5	3.1	0	6.04	0.06	9.23	0.66	0.34	0.01	3.36	3.34	25431.22	15010.62	6279.95	4662.39
6.07	-5	3.1	0	6.04	0.58	9.75	0.62	0.32	0.06	-2.78	-2.76	26863.73	15856.15	6633.70	4925.02
6.07	5	3.1	0	6.04	0.58	9.75	0.62	0.32	0.06	3.51	3.48	26863.73	15856.15	6633.70	4925.02
6.07	-5	3.1	0	6.04	0.93	10.10	0.60	0.31	0.09	-2.47	-2.46	27827.91	16425.26	6871.79	5101.78
6.07	5	3.1	0	6.04	0.93	10.10	0.60	0.31	0.09	3.60	3.57	27827.91	16425.26	6871.79	5101.78
6.07	-5	3.1	0	6.04	1.07	10.24	0.59	0.30	0.10	-2.36	-2.34	28213.59	16652.90	6967.03	5172.49
6.07	5	3.1	0	6.04	1.07	10.24	0.59	0.30	0.10	3.63	3.61	28213.59	16652.90	6967.03	5172.49

References

Bern, C. R., Thompson, A., & Chadwick, O. A. (2015). Quantification of colloidal and aqueous element transfer in soils: the dual-phase mass balance model. Geochimica et Cosmochimica Acta, 151, 1-18.

Brady, N. C., Weil, R. R., & Weil, R. R. (1990). The nature and properties of soils.

Brenner, D. L., Amundson, R., Baisden, W. T., Kendall, C., & Harden, J. (2001). Soil N and 15N variation with time in a California annual grassland ecosystem. Geochimica et Cosmochimica acta, 65(22), 4171-4186.

Burt, R. (2004). Soil survey laboratory methods manual.

Chadwick, O. A., Brimhall, G. H., & Hendricks, D. M. (1990). From a black to a gray box—a mass balance interpretation of pedogenesis. Geomorphology, 3(3-4), 369-390.

Cleveland, C. C., Townsend, A. R., Schimel, D. S., Fisher, H., Howarth, R. W., Hedin, L. O., ... & Wasson, M. F. (1999). Global patterns of terrestrial biological nitrogen (N2) fixation in natural ecosystems. Global biogeochemical cycles, 13(2), 623-645.

Gabet, E. J. (2000). Gopher bioturbation: field evidence for non-linear hillslope diffusion. Earth Surface Processes and Landforms, 25(13), 1419-1428.

Gabet, E. J., & Dunne, T. (2003). A stochastic sediment delivery model for a steep Mediterranean landscape. Water Resources Research, 39(9).

Garten Jr, C. T. (1992). Nitrogen isotope composition of ammonium and nitrate in bulk precipitation and forest throughfall. International Journal of Environmental Analytical Chemistry, 47(1), 33-45.

Hoering, T. (1957). The isotopic composition of the ammonia and the nitrate ion in rain. Geochimica et Cosmochimica Acta, 12(1-2), 97-102.

Heaton, T. H. (1986). Isotopic studies of nitrogen pollution in the hydrosphere and atmosphere: a review. Chemical Geology: Isotope Geoscience Section, 59, 87-102.

Heimsath, A. M., DiBiase, R. A., & Whipple, K. X. (2012). Soil production limits and the transition to bedrock-dominated landscapes. Nature Geoscience, 5(3), 210.

Jin, L., Ravella, R., Ketchum, B., Bierman, P. R., Heaney, P., White, T., & Brantley, S. L. (2010). Mineral weathering and elemental transport during hillslope evolution at the Susquehanna/Shale Hills Critical Zone Observatory. Geochimica et Cosmochimica Acta, 74(13), 3669-3691.

Jones, M. B., & Woodmansee, R. G. (1979). Biogeochemical cycling in annual grassland ecosystems. The Botanical Review, 45(2), 111-144.

Kurtz, A. C., Derry, L. A., Chadwick, O. A., & Alfano, M. J. (2000). Refractory element mobility in volcanic soils. Geology, 28(8), 683-686.

Morford, S. L., Houlton, B. Z., & Dahlgren, R. A. (2016). Geochemical and tectonic uplift controls on rock nitrogen inputs across terrestrial ecosystems. Global Biogeochemical Cycles, 30(2), 333-349.

Mudd, S. M., & Furbish, D. J. (2007). Responses of soil-mantled hillslopes to transient channel incision rates. Journal of Geophysical Research: Earth Surface, 112(F3).

National Atmospheric Deposition Program (NRSP-3). 2019. NADP Program Office, Wisconsin State Laboratory of Hygiene, 465 Henry Mall, Madison, WI 53706.

Reneau, S. L., Dietrich, W. E., Donahue, D. J., Jull, A. T., & Rubin, M. (1990). Late Quaternary history of colluvial deposition and erosion in hollows, central California Coast Ranges. GSA Bulletin, 102(7), 969-982.

Riebe, C. S., Kirchner, J. W., & Finkel, R. C. (2003). Long-term rates of chemical weathering and physical erosion from cosmogenic nuclides and geochemical mass balance. Geochimica et Cosmochimica Acta, 67(22), 4411-4427.

Sudom, M. D., & St. Arnaud, R. J. (1971). Use of quartz, zirconium and titanium as indices in pedological studies. Canadian Journal of Soil Science, 51(3), 385-396.

Thompson, A., Chadwick, O. A., Boman, S., & Chorover, J. (2006). Colloid mobilization during soil iron redox oscillations. Environmental science & technology, 40(18), 5743-5749.

Yoo, K., Amundson, R., Heimsath, A. M., & Dietrich, W. E. (2005). Process-based model linking pocket gopher (Thomomys bottae) activity to sediment transport and soil thickness. Geology, 33(11), 917-920.

Yoo, K., Mudd, S. M., Sanderman, J., Amundson, R., & Blum, A. (2009). Spatial patterns and controls of soil chemical weathering rates along a transient hillslope. *Earth and Planetary Science Letters*, *288*(1-2), 184-193.

Chapter 6. Conclusions and Next Steps

1. Conclusions

1.1 Chapter summary

This dissertation seeks to understand how and why landscapes within the Western Transverse Range respond over multiple timescales of perturbations, specifically looking for how internal and external factors control landscape evolution. The individual chapters of this dissertation contribute towards narrower fields of research within this framework:

In Chapter 3, I demonstrate widespread transience over long timescales for the inland and coastal portions of the Western Transverse Range, in which cosmogenic nuclide erosion rates are an order of magnitude lower than uplift rates. Holocene-age climate drying decreased stream power and increased valley aggradation which slows erosion rates for some catchments. Additionally, the presence of resistant lithologies at the channel outlets keep erosion rates low in high relief regions where streams are headed in erodible rock types. Lastly, small catchments positioned above large channel knickpoints are protected from increases in incision and tend to have very low erosion rates.

In Chapter 4, I investigate how lithology and vegetation influence the spatial heterogeneity of landscape response to recent, anthropogenic erosion. To produce these findings, I developed an innovative way to measure 1) erosion without time-series data, and 2) vegetation cover across an eroded landscape. I show that the amount of anthropogenic erosion is dictated by the underlying lithology. Furthermore, lithology corresponds to changes in vegetation type and presence on the landscape, which has different feedbacks to the amount of on-going erosion.

Finally, in Chapter 5 I return to a soil mantled landscape to determine how the relative chemical weathering within a pedon affects the flux of rock-derived nitrogen, to the soil. Here I show evidence for the presence of rock-derived N within the solum but find that the flux of rock-derived N is overshadowed by atmospheric contributions in this system because of low rates of chemical weathering.

1.2 Overarching conclusions

Across these three studies, two factors dominated the way the landscapes I studied adjust to both long- and short-timescale perturbations: 1) The current semi-arid climate limits how soil is produced and where it can go in a landscape, and 2) The erodibility of the underlying lithology sets how much soil can be produced and how erosion can be translated across catchments. I explore the interplay between the two factors in further detail below.

In each chapter, the warm and dry climate in the westernmost Transverse Range has direct effects on how soil is produced and stored within the region. Over geologic timescales, the warm and dry climate means reduced stream power. Sediment eroded from ridgecrests and steep slopes is stored over tens of thousands of years in low relief portions of the landscape. The timescale over which 10Be accumulation averages is sensitive to this sediment storage in valleys (Chapter 3). These findings are in agreement with work from river terraces in Ventura County that show significant valley aggradation in the early to middle Holocene (DeVecchio et al., 2014).

Regardless of climate, less resistive lithologies also translate changes in uplift more quickly, and this can mean that landscapes underlain by resistant lithologies at the channel mouths can maintain slower erosion rates over the last 100 kyr despite rapid uplift rates

(Chapter 3). These low rates may reflect a relic landscape that has not yet adjusted to a shift in uplift rates because of the resistivity of the underlying bedrock.

The climate and lithology also impact chemical weathering over long-timescales. Chemical weathering is low for ridgecrests or steep-sloped areas with short soil residence times set by the uplift rate (Chapter 5). We can suppose that chemical weathering may be higher if a soil's residence time is much longer than the current period of aridity (~11ky). Longer soil residence times may be found in relic landscape positions (small sub-catchments on SCI) or concave positions receiving sediment and water (shallow slopes and valleys in Sedgwick). The effects of climate limiting chemical weathering means that for a steep slope or ridgecrest to be soil mantled, there needs to be means of physical weathering to produce sufficient soil. At the ridgetop location of the Sedgewick soil pit discussed in Chapter 5, tremendous gopher bioturbation physically disturbs the in-place bedrock, creating a 1m deep solum that is relatively unweathered (50% in-place bedrock by 50cm). This bioturbation by gophers into the underlying bedrock is possible because the shale lithology is fractured, weak, and easily diggable. Therefore, more resistant lithologies are dependent on chemical weathering to produce soil. SCI, which does not currently have soil bioturbators, provides an interesting case study of this conclusion. It's plausible to assume that the presence and depth of non-anthropogenically disturbed soil on the slopes and ridgecrests may be controlled by the residence time of the soil (set by tectonics) and the chemical weatherability of the underlying lithology. This comparison does not account for the presence of mega-fauna bioturbators in the Pleistocene (Pygmy Mammoth) or how the effects of vegetation rooting depth may have influenced soil production on SCI.

On short timescales, the erodibility of the underlying lithology sets the bottom limit of incision and therefore the total volume of sediment that can be mobilized from one location (Chapter 4). Short-timescale perturbations of significantly increased erosion rates occur over too rapid a timescale for chemical weathering to keep pace. Lithologies that are physically cohesive may have soils derived predominantly from chemical weathering processes. Therefore, as a landscape sheds sediment, no new sediment is produced from landscapes underlain by these resistant lithologies, and the bedrock is the bottom limit for landscape response over rapid timescales. However, in areas with physically erodible lithology, the bedrock is not a boundary for erosion and the landscape will continue to incise. This is the case for Pozo Catchment on SCI; friable shale continues to erode once the soil mantle is removed. In contrast, the more resistant volcanic sandstone/tuff in Pozo, shows little erosion that can be attributed to the anthropogenic disturbance. Interestingly, the spatially varied presence of vegetation in Pozo Catchment likely reflects areas where the lithology permits continued erosion – vegetation is absent in areas of high incision underlain by erodible lithologies but present in areas of high incision underlain by resistant lithologies. The areas of high incision in the resistant lithologies are no longer active and instead provide concave regions to gather water and foster revegetation.

2. Next Steps

There are several ideas that present as logical follow-ons from this dissertation. First, I would like to expand the work in Chapter 5 to the whole hillslope in an attempt to capture the effects of valley in-filling on chemical weathering and the flux of rock-derived N. Next, I would like to probe how differences in soil residence time feedback into the amount and spatial patterning of anthropogenic erosion. I expand on these ideas below.

2.1 Rock-derived N flux across a catena

The spatial pattern of rock-derived N flux should be connected with the soil depth at Segdwick Reserve. The valley infilling within Sedgwick Reserve from reduced stream power means that soils are much thicker in toeslopes than on the ridgecrest. Downslope of the ridgecrest pit discussed in Chapter 5, solum depth increases to 4+ meters at the lower-backslope and toeslope positions (Lin et al., 2015). Soil production rate theory dictates that deeper soils have lower production rates than more shallow soils (Heimsath et al., 1997). This means that downslope solum should be more derived from upslope colluvial material than the bedrock and the deeper solum in the toeslope positions should have lower fluxes of rock-derived nitrogen. While it is more challenging to trace rock-derived N than traditional rock-derived nutrients, my work from Chapter 5 elucidates the connection between total $\delta^{15}N$ within the solum and the proportion of rock-derived N in the solum. When the solum is entirely derived from bedrock, the $\delta^{15}N$ signature is derived from both surficial and bedrock inputs of nitrogen. Previous work suggests that organic matter is further decomposed downslope (Lin et al., 2015), this reworking of the organic matter alters the $\delta^{15}N$ signature of the solum to a more biological signal (Hobbie and Ouimette, 2009) and away from the $\delta^{15}N$ signature at the ridgecrest. Therefore, I hypothesize that downslope, soils will become

less bedrock influenced and this will be reflected in a change in the depth pattern of total δ15N to a more biologically-processed signature.

I will test this idea by combining δ15N depth profiles for bulk nitrogen at different hillslope positions with a simple transport model based on soil-depth and curvature relationships to partition the sources of rock-derived nutrients across the catena. The model was introduced by Yoo et al. (2009) to understand the dynamics of rock derived nutrients across the hillslopes. The model calculates total chemical weathering flux across the catena and the contributions to this flux from colluvially transported material and rock-weathering derived material. I will use my estimates of total denudation and chemical weathering rates to provide initial conditions for the model. Downslope soil production rates can be predicted from the relationship between soil production, soil thickness, and hillslope curvature (Heimsath et al., 1997). The average grassland sediment transport rate by Gabet and Dunne (2003) provides a lower boundary check on these predicted rates. Chemical weathering indices can be calculated using similar mass balance techniques as outline in Chapter 5. Lastly, I will measure total δ15N from soils along a hillslope catena previously analyzed by Lin et al. (2015) for total C and N patterns. I expect these results to show differences in the relative importance of rock-derived N and colluvially-transported N soils across the hillslope – showing the proportion of rock-derived nitrogen within the soil dropping off as the soil depth increases downslope. These results will provide a catena-scale insight into rock-derived nitrogen research and also reinforce existing knowledge on rock-derived nutrient dynamics within Mediterranean grasslands.

2.2 Potential feedbacks between long-term catchment evolution and anthropogenic erosion

Anthropogenic erosion on Santa Cruz Island overprints onto the pre-existing balance between uplift and erosion set by long-term climate and tectonics. Despite similar experiencing similar intensities of anthropogenic disturbance, south-draining catchments underlain by schist have catchment average erosion rates an order of magnitude faster than north-draining catchments. The mismatch in erosion rates between the south-draining, steady-state catchments and the north-draining, slower eroding sub-catchments that share the ridgeline leads to an asymmetry in catchment shape (c.f. Chapter 3, Fig. 7). The slowly eroding central valley sub-catchments are losing area to the faster eroding, south-draining catchments that share the ridgeline (Dohrenwend, 1978). If relic soil depth is set by the residence time of the catchment (holding lithology constant) and if we assume that the schist is physically resistant such that the bedrock is the boundary layer for recent anthropogenic erosion, then the north-draining catchments should have deeper soils and consequently the maximum depth for anthropogenic soil erosion will be higher. However, I also predict that higher soil moisture and longer soil residence times increases vegetation density and pedogenesis (soil armoring) – which could dampen soil transport (Istanbulluoglu et al., 2008; Johnstone et al., 2017) and minimize the impacts of anthropogenic erosion. Therefore, I predict that soil erosion from the south-draining catchments will be shallow but more pervasive than erosion from the north-draining catchments.

To test this hypothesis, I will combine topographic metrics with erosion rate data and estimates of anthropogenic erosion to ascertain soil residence time, soil depth, and the depth of erosion. This dissertation provides the algorithm for producing the anthropogenic erosion maps (Chapter 4) necessary for determining differences in landscape response. I have also measured the cosmogenic nuclide derived erosion rates for the south- and north-draining

catchments, which show the landscape is either in steady-state (south-draining) or slowly aggrading (north-draining). To this I will add new topographic metrics, hilltop curvature and hillslope steepness, that are sensitive to shifts in long-term erosion and uplift rates, which will help spatially constrain soil residence time differences assumed from the catchment average erosion rate data. I will also add field measurements of ridgetop, relic soil depths to assess the variability of soil depth between north- and south-draining ridgecrests and slopes. This study will elucidate the effects of long-term erosion rate on the response of a landscape undergoing rapid, high magnitude erosion. With the increase in human-driven disturbances globally, I expect these results to be particularly useful for understanding landscape response into the next decades.

3. Last thoughts

This dissertation demonstrates that the interplay between lithology and climate is important for understanding the trajectories of landscape response to multiple timescales of disturbance. While these findings are not entirely novel, these relationships had not been studied fully in this region and the individual chapters contribute substantial new information to fields within the Earth Surface Processes. This work also sets the geomorphic stage for continuing research in the Western Transverse Range, as outlined in this chapter.

4. References

Binnie, S. A., Phillips, W. M., Summerfield, M. A., & Fifield, L. K. (2007). Tectonic uplift, threshold hillslopes, and denudation rates in a developing mountain range. *Geology*, 35(8), 743-746.

DiBiase, R. A., Whipple, K. X., Heimsath, A. M., & Ouimet, W. B. (2010). Landscape form and millennial erosion rates in the San Gabriel Mountains, CA. *Earth and Planetary Science Letters*, 289(1-2), 134-144.

Dohrenwend, J. C. (1978). Systematic valley asymmetry in the central California Coast Ranges. *GSA Bulletin*, 89(6), 891-900.

Gabet, E. J., & Dunne, T. (2003). A stochastic sediment delivery model for a steep Mediterranean landscape. *Water Resources Research*, 39(9).

Heimsath, A. M., Dietrich, W. E., Nishiizumi, K., & Finkel, R. C. (1997). The soil production function and landscape equilibrium. *Nature*, 388(6640), 358.

Hobbie, E. A., & Ouimette, A. P. (2009). Controls of nitrogen isotope patterns in soil profiles. *Biogeochemistry*, 95(2-3), 355-371.

Istanbulluoglu, E., Yetemen, O., Vivoni, E. R., Gutiérrez-Jurado, H. A., & Bras, R. L. (2008). Eco-geomorphic implications of hillslope aspect: Inferences from analysis of landscape morphology in central New Mexico. *Geophysical Research Letters*, 35(14).

Johnstone, S. A., Chadwick, K. D., Frias, M., Tagliaro, G., & Hilley, G. E. (2017). Soil development over mud-rich rocks produces landscape-scale erosional instabilities in the northern Gabilan Mesa, California. *GSA Bulletin*, 129(9-10), 1266-1279.

Lin, Y., Prentice III, S. E., Tran, T., Bingham, N. L., King, J. Y., & Chadwick, O. A. (2016). Modeling deep soil properties on California grassland hillslopes using LiDAR digital elevation models. *Geoderma regional*, 7(1), 67-75.

Yoo, K., Mudd, S. M., Sanderman, J., Amundson, R., & Blum, A. (2009). Spatial patterns and controls of soil chemical weathering rates along a transient hillslope. *Earth and Planetary Science Letters*, 288(1-2), 184-193.